

DIPA GHINDANI

Tailoring Light-Matter Interaction via Advanced Nanophotonic Structures

From Passive to Dynamically Tunable Systems

DIPA GHINDANI

Tailoring Light-Matter Interaction
via Advanced Nanophotonic Structures
From Passive to Dynamically Tunable Systems

ACADEMIC DISSERTATION

To be presented, with the permission of
the Faculty of Engineering and Natural Science
of Tampere University,
for public discussion in the auditorium TB103
of the Tietotalo building, Korkeakoulunkatu 3, 33720 Tampere,
on 31st of March 2023, at 12 o'clock.

ACADEMIC DISSERTATION

Tampere University, Faculty of Engineering and Natural Science
Finland

*Responsible
supervisor
and Custos*

Professor
Humeyra Caglayan
Tampere University
Finland

Pre-examiners

Assistant Professor
Nasim Mohammadi Estakhri
Chapman University
United States of America

Professor
Polina Kuzhir
University of Eastern Finland
Finland

Opponent

Professor
Olivier Martin
École polytechnique fédérale de
Lausanne (EPFL)
Switzerland

The originality of this thesis has been checked using the Turnitin OriginalityCheck service.

Copyright ©2023 Dipa Ghindani

Cover design: Roihu Inc.

ISBN 978-952-03-2809-2 (print)

ISBN 978-952-03-2810-8 (pdf)

ISSN 2489-9860 (print)

ISSN 2490-0028 (pdf)

<http://urn.fi/URN:ISBN:978-952-03-2810-8>



Carbon dioxide emissions from printing Tampere University dissertations have been compensated.

PunaMusta Oy – Yliopistopaino
Joensuu 2023

Dedicated to my Parents.

*Success can come to you by courageous devotion to the task lying in front of
you.*

C.V.Raman.

ACKNOWLEDGEMENTS

The support, encouragement, and opportunities that have been provided to me during my doctoral journey have all been invaluable to the completion of my thesis.

First and foremost, I would like to sincerely thank my supervisor, Professor Humeyra Caglayan, for providing me with an excellent opportunity to come to ‘Finland’ and join the Metaplasmonics team to pursue a doctorate in the field of nanophotonics. I am thankful for her profound belief in my abilities. I have learned a lot from Professor Humeyra, starting from the core research topic, progress tracking, managing data, to writing scientific papers. The hard work, enthusiasm, energy, and vision she put forth are contagious. I would like to express gratitude for her invaluable guidance and endless support throughout my doctoral research and dissertation.

Next, I would like to thank Professor Olivier Martin for taking over the Ph.D. exam, Professor Polina Kuzhir, and Professor Nasim Estakhri for being pre-examiners for my thesis. Also, thanks to Professor Esa Räsänen for the internal examination.

It has been a privilege to work in the Metaplasmonics research group and to be part of the fantastic photonics community. I greatly appreciate the support received from the whole Metaplasmonics team: Carlos, Rakesh, Jesse, Ipek, Arttu, and Alessandro. Rakesh and Carlos, thank you for great coffee break discussions about all different topics. I enjoyed working with the team together, and all the other events we had outside of the university.

I am thankful to Professor Arri Priimägi for his guidance and for introducing and providing me with wonderful smart materials that were essential for the success of my thesis. At this point, I would also like to acknowledge Kim, Markus, Alex, Chiara, Mari, Matias, and the whole SPM research team for the collaboration.

I would like to extend my gratitude to Tuomas Pihlava, Dr. Semyon Chervinskii, Dr. Antti Tukiainen, and Dr. Alireza Rahimi for helping me with the measurements. Also, I would like to acknowledge Mervi Koskinen, Dr. Jarno Reuna, Dr. Turkka Salminen, Dr. Suvi Lehtimäki, Dr. Hanna Hulkkonen, and Dr. Marika Janka for their technical help, ever-helping discussions, and for sharing their expertise. I wish to thank Marketta Myllymäki, Anne Viherkoski, and Anna Nykänen for their help with all my administrative questions.

This thesis is a culmination of an education that began long before my journey at Tampere University, and so I'm deeply grateful to innumerable people who have helped me along the way. Especially, my time at IITB, TIFR, and TUNI has contributed to my development as a researcher and a person, and I'm grateful to have had so many places to call home. I'm heartily thankful to Prof. Duttagupta (IIT-Bombay) and Prof. Prabhu (TIFR Mumbai) for believing in my potential and providing me with such an excellent photonics platform.

A big thanks to Vaibhav Sir, Sowmya di, Abhimanyu, Arnab, Aman, Abhishek, Piyush, and Shalom for being such amazing friends. And special thanks go to Abhishek; it's hard for me to articulate just how grateful I am for his unwavering support and steadfastness. Thank you for always being there for me, for motivation, for encouragement, for believing in me more than I believed in myself, and for all the wonderful discussions we had about philosophy, culture, faith, and science.

It has been a pleasure getting to know all my wonderful friends in Tampere, and I am grateful for our friendship as well as all the unforgettable events, trips, and celebrations (especially Deepawali celebrations in Tampere's coldest and darkest times).

Finally, I am thankful to my husband for his encouragement and support during the last phase of my thesis. It was a long journey to get here, and my parents supported me unquestioningly at every step of all my pursuits and always encouraged me to believe that I could achieve anything. I am also grateful to my late grandparents, Morbai and Prabhudas Ghindani, for instilling the importance of education and values.

I am blessed to have a brother like Rakesh Bha, I am forever indebted to my brother for his generosity, understanding, sacrifices, and continuous support and I'm so glad that we have each other.

I thank my whole family for all the support and love.

Thank you!

Tampere, 12.02.2023

Dipa Ghindani

ABSTRACT

Light-matter interaction is the fundamental principle of photonics that governs numerous disruptive applications. Dynamically tuning the light-matter interaction is key to designing advanced photonic devices with improved and enhanced functionalities. Specifically, having active control of the amplitude, wavelength, phase, and polarization of light is vital. It essentially addresses the key pillars of photonics, ranging from generating, guiding, manipulating, amplifying, and detecting light.

This thesis presents a framework and platform to model, tailor, and enhance the light-matter interactions in nanophotonic structures. Epsilon-near-zero (ENZ) materials, plasmonic nanostructures, and metal-insulator-metal (MIM) cavities were utilized as a light-matter interaction platform. First, the underlying mechanism of emission enhancement was unravelled by integrating fluorescent dye with the MIM cavity. This study suggests a pathway for engineering the emission properties of an emitter through both Purcell and excitation rate enhancement. Following this, dynamic emission tuning was achieved, whereby a fluorescent dye containing hydrogel integrated MIM cavity was utilized. The thickness of the insulator layer was tuned by changing the ambient humidity, which resulted in spectral tuning of cavity resonance, hence the active tuning of emission.

The coupling strength quantifies the light-matter interaction, so tuning the coupling strength is another way to tailor the light-matter interaction. By developing a novel electrical gating scheme, an active tuning of the coupling strength was demonstrated in a strongly coupled system comprised of ENZ materials that support ENZ mode and gold nanorods supporting the localized surface plasmon mode. Lastly, by harnessing the vanishing index of the ENZ material, less sensitivity of the spectral position of photonic resonance towards the geometrical perturbations was obtained through a polarization-independent plasmonic structure on an ENZ substrate.

Overall, this thesis shows broad opportunities for using nanophotonic systems to tailor light-matter interactions dynamically.

CONTENTS

1	Introduction	25
1.1	Light-matter interaction	25
1.2	Emergence of active nanophotonics	27
1.3	Application prospects of active nanophotonic structures	29
1.4	Research questions	31
1.5	Outline of the thesis	31
2	Light matter interactions at different nanophotonic structures	33
2.1	Plasmonic systems	33
2.1.1	Theory of localised surface plasmon resonance	34
2.1.2	Applications of localised surface plasmons	36
2.2	Metal-insulator-metal Fabry-Pérot resonance	36
2.3	Epsilon-near-zero materials and mode	38
2.3.1	Properties and applications of ENZ materials	39
2.3.2	ENZ mode	43
3	Enhanced and active tunable emission	45
3.1	Organic dye integrated in metal-insulator-metal structure	46
3.1.1	Emission enhancement in photonic environment	46
3.1.2	Structure optimization and fabrication	47
3.1.3	Optical characterization: reflection and emission	49
3.1.4	Mechanisms behind emission enhancement	53
3.2	Organic dye integrated in hydrogel-based metal-insulator-metal structure	53

3.2.1	Hydrogel synthesis and fabrication of metal-hydrogel+dye-metal structure	54
3.2.2	RhB dye characterization and optimization of MIM design	56
3.2.3	Passive emission tuning	57
3.2.4	Reversible and active emission tuning in air	60
3.2.5	Active emission tuning in water	63
3.3	Conclusion	66
4	Electrically tunable coupling of epsilon-near-zero and plasmonic modes	67
4.1	ENZ mode excited in the ITO layer	68
4.2	LSP mode of nanoantenna and its fabrication	69
4.3	Strong coupling of ENZ and LSP modes	71
4.4	Design of dynamically tunable system	73
4.4.1	Gating system	73
4.4.2	Hall measurement	75
4.5	Gate-tunable coupling of ENZ-LSP mode	76
4.5.1	Active tuning of strongly coupled ENZ-LSP modes	76
4.5.2	Reversible behavior of designed gated system	79
4.5.3	Effect of negative voltage	80
4.5.4	Simulation results: tunable ENZ-LSP coupling	82
4.6	Conclusion	83
5	Pinning effect on ITO-based polarization independent nanostructure	85
5.1	ENZ substrate characterization	86
5.2	Polarization-independent structure design	87
5.3	Demonstration of resonance pinning	89
5.4	Conclusion	94
6	Summary and future work	95
6.1	Future research directions	96
	References	99

Appendix A	Appendix	113
A.1	Electron beam evaporator	113
A.2	Scanning electron microscope	113
A.3	Electron beam lithography	114
Appendix B	Appendix	117
B.1	Other publication	117
Publication I		121
Publication II		129
Publication III		139
Publication IV		147

List of Figures

1.1	The SEM image of Au nanodiscs of radius 150 nm on the ITO substrate as an example of NS fabricated by the author.	26
1.2	Illustration of various schemes to realize dynamic tunability in the active nanophotonic systems.	28
1.3	Overview of prospective applications of tunable nanophotonic structures based on different advanced approaches. Applications due to spatial and spectral control; beam steering [25], holography [26], AR/VR component. Application due to temporal and emission control; tunable laser sources [27] and bio/chemical sensors [28]. By integrating active nanophotonics with existing technology, applications like super-resolution focusing lens [29], and active imaging devices [30] can be realized.	30
2.1	An artistic illustration of LSP mode in a metal nanoparticle.	35

2.2	Reflection from the metal-insulator-metal structure and its electric field profile.	37
2.3	Three-layer geometry with permittivity ε_1 , ε_2 and ε_3 respectively. [88]	43
2.4	Dispersion relation of the three-layered (air - 40 nm ITO - glass) system. [89]	44
3.1	An artistic illustration of MIM cavity comprise of Ag- (PMMA+LDS 798 dye) - Ag	48
3.2	a) The color plot of simulated reflection spectra for various thicknesses of PMMA. The white dashed lines highlight the resonance wavelengths corresponding to PMMA thicknesses 140 nm and 190 nm. b) Simulated reflection plot for MIM cavity with PMMA thickness 140 nm and 190 nm. The inset shows the artistic diagram of the MIM cavity.	49
3.3	Experimentally recorded reflection spectra indicated with solid blue lines (a) for MIM-I cavity and (b) MIM-II cavity. The absorption and emission of LDS-798 dye are marked by black and solid red lines, respectively. [97]	50
3.4	PL spectra of LDS 798 dye integrated with (a) MIM-I cavity and (b) MIM-II cavity. The emission spectra for bare LDS 798 dye spin-coated on glass substrate for reference is highlighted by dotted black line. [97]	50
3.5	Time resolved PL intensity results for LDS dye embedded in (a) MIM-I cavity and (b) MIM-II cavity. The fluorescent lifetime for reference dye-coated sample (on bare glass substrate) is shown by the dotted black line. [97]	51

3.6	The electric field contour simulated for (a) MIM-I cavity and (b) MIM-II cavity, and the inset shows the diagrammatic representation of both cavities. [97]	53
3.7	Schematic of the RhB-containing hydrogel incorporated into the MIM cavity.	55
3.8	Measured transmittance spectra of reference hydrogel coatings on a glass substrate to confirm photopolymerization time.	56
3.9	(a) Emission (solid red line) and absorption (dashed black line) spectra of fluorescent dye RhB (b) Contour plot of reflection spectra simulated for various thickness of hydrogel. [18]	57
3.10	Optical images of the MIM samples with different hydrogel thicknesses. The thicknesses of hydrogels were measured using a profilometer.	58
3.11	(a) Experimentally recorded reflection spectra for different thicknesses of the hydrogel. (b) The PL response of RhB incorporated in MIM cavity with different hydrogel thicknesses. [18]	59
3.12	(a) Experimentally recorded reflection spectra of MIM cavity at different humidity values. The thickness of hydrogel in the dry state is 110 nm. The solid curve represents the forward (i.e., increase in humidity from 3% to 80%), and the line depicts the reverse cycle (i.e., decrease in humidity from 80% to 3%). (b) Steady-state emission spectra of a cavity at different humidities. (c) Optical images of MIM samples at various humidities. The corresponding thicknesses of hydrogel are marked in the optical images which were extracted from the simulation. [18]	61
3.13	(a) Experimentally recorded reflection spectra of MIM cavity (with 110 nm hydrogel) at different humidities. (b) Steady-state PL of the dye at varying humidity values.	62

3.14	Steady-state PL spectra of RhB dye molecules bound with hydrogel at different humidities.	63
3.15	(a) Experimentally recorded reflection spectra of MIM cavity completely immersed in DI water for different time duration. The inset shows the corresponding hydrogel thickness calculated using simulation. (b) PL spectra of dye incorporated with MIM for dry case and when completely immersed in water for different duration. The inset shows the optical image of sample for dry case and after immersing into water for 20 minutes. [18]	64
3.16	Effective refractive index vs thickness of the hydrogel-water complex.	65
3.17	The simulated reflection spectra of the MIM cavity with varying insulator (hydrogel) thickness in two cases: (a) by keeping the hydrogel's refractive index constant at 1.503. (b) by considering the effective index of the hydrogel-water complex.	66
4.1	(a) Complex permittivity of a 40 nm thin ITO film measured using ellipsometry. (b) Dispersion relation of the ionic liquid - ENZ material - glass three-layered system.	69
4.2	(a) 40 nm thin ITO film's permittivity result, where real and imaginary parts are depicted by the solid blue line and dotted blue line. The ENZ region is highlighted with grey color. The simulated transmittance spectrum of the optimized nanorods placed on a glass substrate is shown by the solid red line. [69] (b) diagrammatic representation of unit cell consisting of a gold nanorod on a glass substrate. .	70

4.3	(a) Measured transmittance spectra of plasmonic antenna array on ITO substrate and the inset depicts SEM image of the Au nanorods. (b) Simulated electric field (E_x) plot of antenna array on ITO substrate at lower polariton (1260 nm) and upper polariton (1600 nm) [69]	71
4.4	Simulation result for strong coupling between nanorod and ENZ mode of ITO. The dimensions of the nanorod vary by a common factor ranging from 0.7 to 1.2. The observed anti-crossing behavior implies that the ITO + Nanorod system exhibits strong coupling. . .	72
4.5	Optimization of gating architecture: an artistic illustration of the three different cases to achieve the electrical gating in transmission mode.	74
4.6	(a) diagrammatic representation of Hall measurement compatible gating system. (b) Hall measurement result, the carrier density in ITO at varying voltage values.	76
4.7	(a) Experimentally recorded spectra at various bias voltages. (b) Zoomed portion of transmission spectra near lower polariton wavelength. . .	77
4.8	Measured transmission spectra at different gating voltages (individual spectra near lower polariton at different voltages are vertically offset). . .	78
4.9	(a) Simulated transmission spectra of nanorods with various dimensions named as NR1, NR2, NR3. (b), (c) and (d) Experimentally recorded electrical tuning of transmission spectra of nanorod-ITO integrated systems corresponding to NR1, NR2, and NR3, respectively.	79
4.10	(a) The schematic of ITO gated system. (b) I-V characteristics of the device.	80
4.11	Transmission spectra recorded at different days, which exhibits nearly identical behavior which proves the reversibility of the system. . . .	81

4.12	Experimentally recorded electrical tuning of transmission spectra of nanorod-ITO integrated systems (a) under positive bias, (b) under negative bias.	81
4.13	Simulated transmission spectra by varying the carrier concentration of ITO (to emulate the response at different biasing voltages).	83
5.1	Experimentally recorded complex permittivity of 100 nm thick ITO film, blue and red solid line depicts real and imaginary part of ITO's permittivity respectively and a grey area indicated ENZ wavelength region.	86
5.2	(a) Schematic of polarization-independent Au nanoantenna array of thickness 40 nm on a 100 nm-thick ITO layer on a glass substrate. (b) Simulated transmittance spectra of the plasmonic nanoantennas on the ITO substrate; the insets depict the electric field profile at the corresponding wavelength. [121]	88
5.3	(a) SEM image shows the top view of Au nanoantenna array (scaling factor = 1, i.e., $l_s = 130$ nm and $l_l = 420$ nm), dashed yellow box indicates the supercell with supercell periodicity 1150 nm in x and y directions. The inset shows the SEM image taken at 30° tilt. [121]	89
5.4	(a) SEM images of the fabricated set of samples with varying scaling factors from 0.8 to 1.2 and a constant periodicity of 1150 nm in both x and y.	90
5.5	(a),(b) Simulated transmittance spectra of the supercell array of nanorods on glass and an ITO substrate at different scaling factors; the inset shows a schematic of the Au antenna array on glass and ITO, respectively. (c),(d) Experimentally recorded transmission spectra of the supercell array of nanorods on a glass and ITO substrate. [121]	91

5.6	Simulated and experimental transmittance spectra of 100 nm ITO film on a glass substrate.	92
5.7	(a), (b) Simulated and experimental wavelength shift ($\Delta\lambda$) as a function of scaling factor respectively, at resonance 1 (λ_1) at a shorter wavelength. (c), (d) Simulated and experimentally recorded wavelength shifts corresponding to resonance 2 (λ_2) at a longer wavelength. [121]	93
5.8	Resonant wavelength (λ) as a function of antenna length (l_l) for the Glass (orange) and ITO (Green) substrates. The solid lines are calculated analytically, and square and circular markers result from FDTD numerical calculations. [121]	94

ABBREVIATIONS

Ag	Silver
AIBN	azobis(isobutyronitrile)
AR	Augmented reality
Au	Gold
AZO	Aluminum-doped zinc oxide
BP	Benzophenone acrylamide
CMT	Coupled mode theory
DI	Deionized
e.g.	for example, from Latin <i>exempli gratia</i>
EBL	Electron-beam lithography
EM	Electromagnetic
ENZ	Epsilon-near-zero
et al.	and others, from Latin <i>et alii</i>
FDTD	Finite-Difference Time-Domain
FP	Fabry-Pérot
GSP	Gap surface plasmon
IPA	Isopropyl alcohol
ITO	Indium Tin oxide
LASER	Light amplification by stimulated emission of radiation
LSP	Localized surface plasmon
LSPR	Localized surface plasmon Resonance

MIBK	Methyl isobutyl ketone
MIM	Metal-Insulator-Metal
MM	Metamaterial
NIPAm	N-Isopropylacrylamide
NIR	Near-infrared
NR	Nanorod
NS	Nanophotonic structure
PbS	Lead sulfide
PL	Photoluminescence
PML	Perfectly-matched layers
PMMA	Poly(methyl methacrylate)
PSP	Propagating surface plasmon
Q	Quality factor
R.I.	Refractive Index
RH	Relative humidity
RhB	Rhodamine B
RIE	Reactive ion etching
RPM	Rotations per minute
SEM	Scanning electron microscope
SPP	Surface plasmon polariton
SRR	Split ring resonator
TCO	Transparent conducting oxide
Ti	Titanium
TMM	Transfer matrix method
UV	Ultraviolet
VR	Virtual reality

ORIGINAL PUBLICATIONS

- Publication I D. Ghindani, A. R. Rashed and H. Caglayan. Unveiling spontaneous emission enhancement mechanisms in metal-insulator-metal nanocavities. *Photonics Research* 9.2 (2021), 237–242. DOI: 10.1364/PRJ.411456.
- Publication II D. Ghindani, I. Issah, S. Chervinskii, M. Lahikainen, K. Kuntze, A. Priimagi and H. Caglayan. Humidity-Controlled Tunable Emission in a Dye-Incorporated Metal-Hydrogel-Metal Cavity. *ACS Photonics* 9.7 (2022), 2287–2294. DOI: 10.1021/acsp Photonics.2c00202.
- Publication III D. Ghindani, A. R. Rashed, M. Habib and H. Caglayan. Gate Tunable Coupling of Epsilon-Near-Zero and Plasmonic Modes. *Advanced Optical Materials* 9.22 (2021), 2100800. DOI: <https://doi.org/10.1002/adom.202100800>.
- Publication IV D. Ghindani, T. Pihlava and H. Caglayan. Suppressing the spectral shift of a polarization-independent nanostructure with multiple resonances. *Opt. Lett.* 47.21 (2022), 5553–5556. DOI: 10.1364/OL.472360.

Author's contribution

- Publication I The author worked with A. R. Rashed and Humeyra Caglayan for idea formulation. The author performed the simulations, designed the structure, and fabricated the structure. The author analyzed the data and wrote the manuscript under the guidance of Humeyra Caglayan. A. R. Rashed did the measurements.

- Publication II The author, together with Semyon Chervinskii and Humeysra Caglayan, formulated the idea. The author performed numerical simulations for the optimization of structures. The author designed and fabricated the structure. The author, together with Semyon Chervinskii and Ibrahim Issah, created and planned the experiments. The author carried out the data analysis and wrote the manuscript. The work was accomplished in collaboration with Arri Priimagi's Smart Photonic Materials (SPM) research team, and Kim Kuntze synthesized the Hydrogel+dye. Also, Markus Lahikainen and Kim Kuntze gave the theory of hydrogel's properties. Ibrahim Issah did the measurements. Humeysra Caglayan and Arri Priimagi guided the whole work.
- Publication III The author and Humeysra Caglayan structured the idea. The author carried out simulations and designed the structure. The author optimized nanostructure dimensions and selected materials to be used and nanofabrication. The author developed a novel gating system. The author, together with A. R. Rashed, planned the experiments. The author wrote the manuscript under the guidance of Humeysra Caglayan. Bilge Can Yildiz and Mohsin Habib contributed to the initial discussion of the project. A. R. Rashed performed the transmission measurements. Humeysra Caglayan guided all of the work.
- Publication IV The author designed the structure and carried out simulations under the supervision of Humeysra Caglayan. The author did structure optimization and fabrication. The author, together with Tuomas Pihlava, planned the experiment. The author analyzed the data and wrote the manuscript. Tuomas Pihlava did the measurements and contributed to the data plotting.

1 INTRODUCTION

1.1 Light-matter interaction

The role of light is significant in our daily lives, and it won't be an exaggeration to say that it has enhanced the quality of modern lifestyles. Almost, all sectors, including medicine, communication, defense, information technology, and advanced manufacturing, are benefiting from cutting-edge technologies which involve light. The umbrella which includes the sciences and technologies related to light is called 'photonics'. The word photonics is derived from the word 'photon', which represents the smallest entity of light analogous to an electron in electricity. So essentially, photonics involves the proper use of light as a tool for the benefit of society. Historically, the term photonics was first introduced to designate the field of research areas like telecommunication and information processing. Studies in the field of photonics were fuelled by the discovery of lasers in nearly the 1960s [1]. Further, the development of optical fiber laid the foundation for the industrial revolution in the telecommunications sector during the late 20th century. However, from the current perspective, the research arenas for photonics are not only limited to the telecommunication and information processing sectors. Nowadays, it encompasses a multidisciplinary character, for instance, bio-photonics.

Light-matter interaction is the heart of current research activities in photonics which helps in driving innovative technologies and unraveling new physics. Light-matter interactions are essential for the efficient conversion of light into various forms, such as current in photovoltaic devices [2, 3] and chemical energy in biological light-harvesting systems [4]. Notably, in recent years a new paradigm based on controlling light-matter interactions has emerged, which provides a way to manipulate and synthesize novel quantum materials [5, 6]. A prime example to illustrate this fact is the demonstration of light-induced superconductivity [7]. Therefore, it is imperative to study and control light-matter interactions. In the quest to control

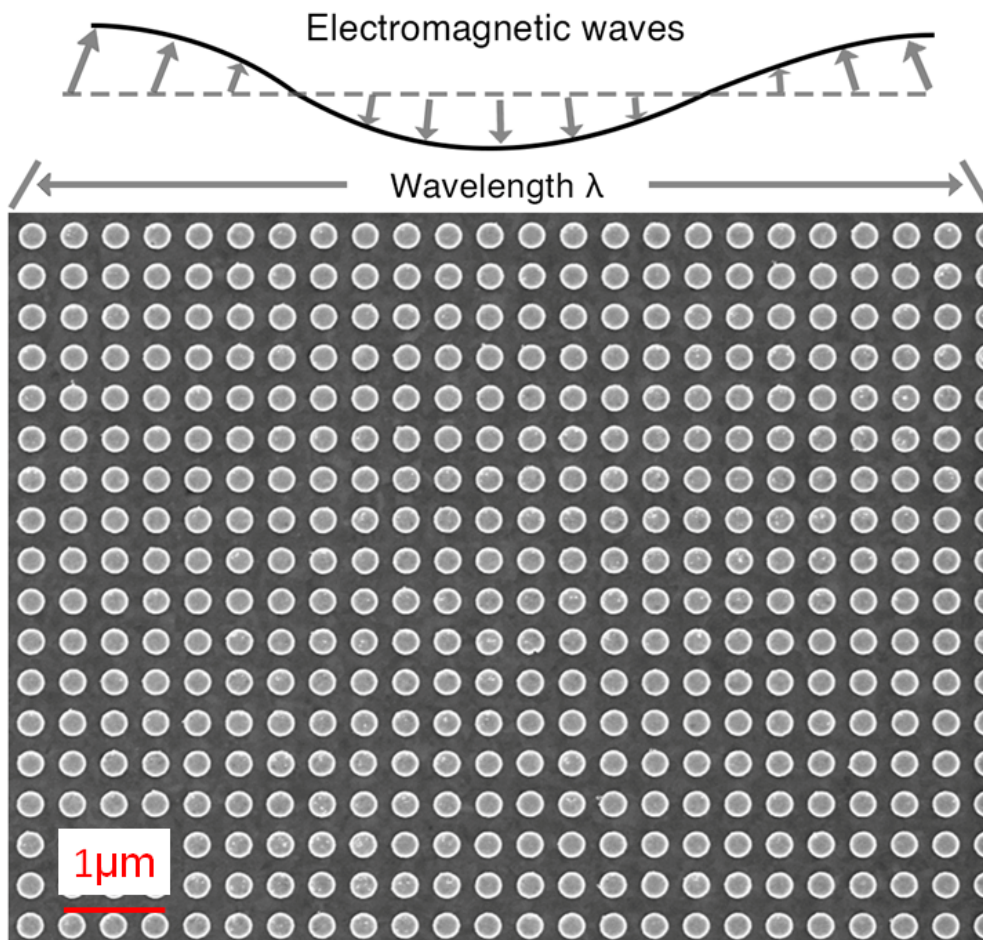


Figure 1.1 The SEM image of Au nanodiscs of radius 150 nm on the ITO substrate as an example of NS fabricated by the author.

light-matter interaction, the discovery of nanophotonic structures (NSs) has opened a new research arena. An example of a fabricated NS consisting of an array of Au nanodiscs is shown in Fig. 1.1. The NSs enable on-demand tailoring of light-matter interaction, either by enhancing light confinement at the nanoscale or by controlling emission from the atoms or molecules. The nanophotonic system has offered remarkable new approaches to manipulating light and allowed unprecedented control over the amplitude, phase, and polarization of light waves. However, despite the impressive progress, the majority of NSs observed today are static in nature, meaning their optical properties are fixed after their fabrication. To uplift the application do-

mains and achieve technological advancement, real-time active control of the optical properties of these NSs is vital. This requirement has led to the development of ‘active nanophotonics’. The active tunability of properties of nanostructures expands the importance of photonic devices for practical applications. Intriguing photonic devices have evolved after introducing the concept of active nanophotonics. So far, the nanophotonics platform has been used to demonstrate several optical properties like phase control, amplitude modulation, and frequency tuning. However, their utilization for achieving real-time control of light-matter interactions is largely untapped.

1.2 Emergence of active nanophotonics

As discussed earlier, the NSs provide a new scale invariant design paradigm to create functional devices in photonics with remarkable properties, which is difficult to achieve from the library of conventional or natural materials. From a broader perspective, these structures can be categorized into two sections - a) Passive and b) Active NSs. Passive structures are those whose optical properties are fixed once they are fabricated. The flexibility to engineer the optical properties of nanophotonic structures provided a novel platform to demonstrate unique functionalities. Although the passive NSs have given the flexibility to engineer the optical response at will but lack post-fabrication tunability.

However, for various potential applications, it is desirable to control the amplitude, phase, and polarization of transmitted or reflected lights through electrical, optical, thermal, or mechanical means. This requirement has led to the development of active nanophotonics. In the quest to develop active nanophotonics, many demonstrations have been done in the scientific community e.g., in 2011, Zheludev *et al.* [8] achieved tunable spectral response via thermal control, in 2014, Capasso, Belkin and Halas groups [9, 10, 11] demonstrated electrical control. Additionally, the research activities to develop different modules of active nanophotonics have grown and expanded. To date, researchers have achieved several ways to achieve dynamic tunability. These include optical excitation [12, 13, 14], temperature control [15, 16], electrical control [17], chemical approach [18, 19] and mechanical control [20].

Fig. 1.2 shows the conceptual representation of active nanophotonics, where resonant elements are controlled by external stimuli e.g., optical, electrical, thermal,

chemical, or mechanical.

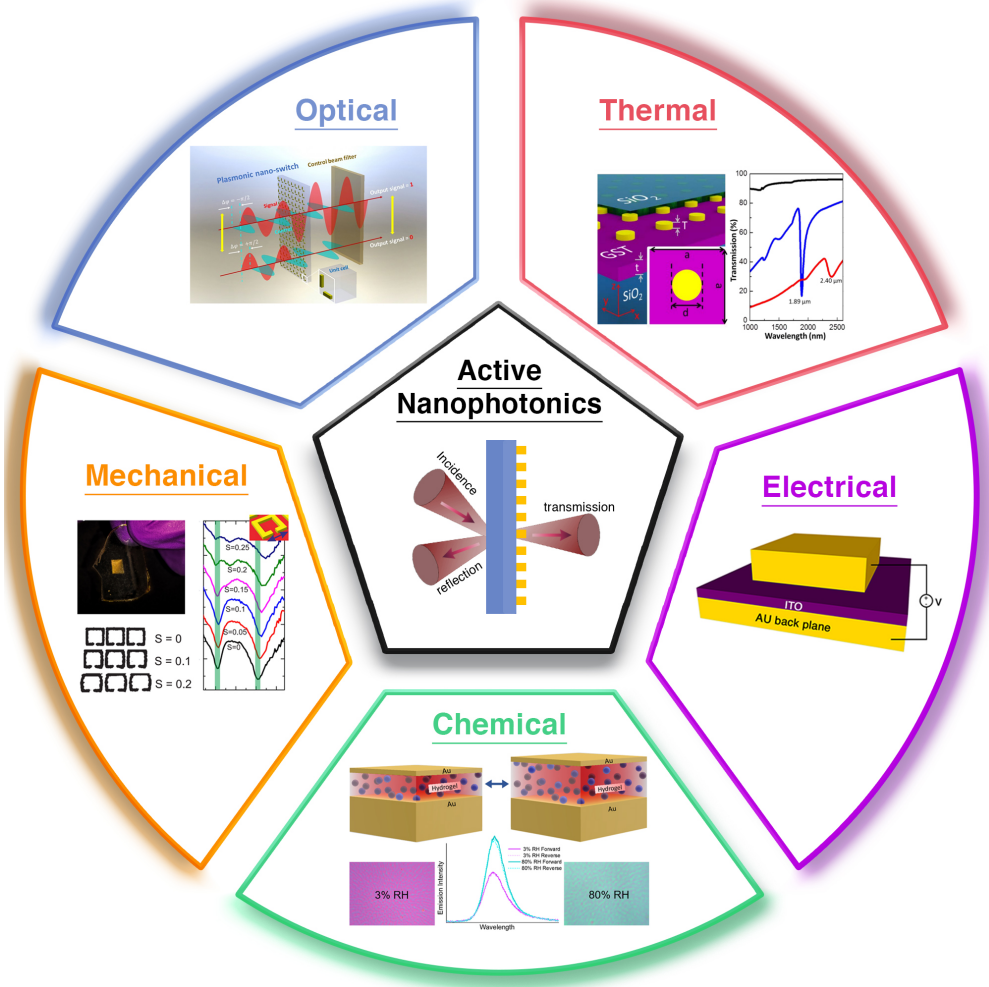


Figure 1.2 Illustration of various schemes to realize dynamic tunability in the active nanophotonic systems.

The underlying principle to accomplish active control on the optical properties of nanostructures is either i) by changing the local dielectric environment or ii) by modifying the geometrical shape of the constituent elements. Researchers have explored both routes. The change in the local dielectric environment of the subwavelength constituents of nanostructure design allows for dynamic control of their reflection and transmission. For instance, optical excitation of nanoresonators reduces the capacitive strength, thus reducing the resonance strength [21]. In addition to ampli-

tude modulation, the same strategy can be utilized to achieve phase modulation that could be useful for beam steering and spatial light modulator applications. In the context of practical applications, electrical control is preferable, as it can be used for designing novel chip-scale photonic devices. In this regard, several active nanophotonic designs were devised and demonstrated electrical tuning of phase, and amplitude [22, 23].

1.3 Application prospects of active nanophotonic structures

The advancement to achieve on-demand control of amplitude, phase, and polarization of light by using active nanophotonics has opened a new avenue for disruptive applications. Fig. 1.3 highlights the broad range of applications ranging from imaging, display sensing, communication, energy, and space technologies that could potentially be realized by active nanophotonics [24].

Some initial proof of concept applications based on active NSs has shown promising outlooks. The prospective application dimensions can be classified into three major categories: (1) applications due to spatial and spectral control of active nanophotonics, (2) applications due to temporal and emission control of nanophotonics, and (3) applications due to integrating active NSs with the existing technologies. The key applications corresponding to each category are listed below:

1. Applications with spatial and spectral control of active nanophotonics [31, 32, 33, 34, 35]
 - Beam steering for LIDAR and wireless communication
 - Dynamic holography
 - Active polarization control
 - Devices for AR/VR applications
2. Applications with temporal and emission control of active nanophotonics [36, 37, 38]
 - Active bio/chemical sensors
 - Tunable laser sources
 - Thermal emission devices
 - Nonreciprocal devices

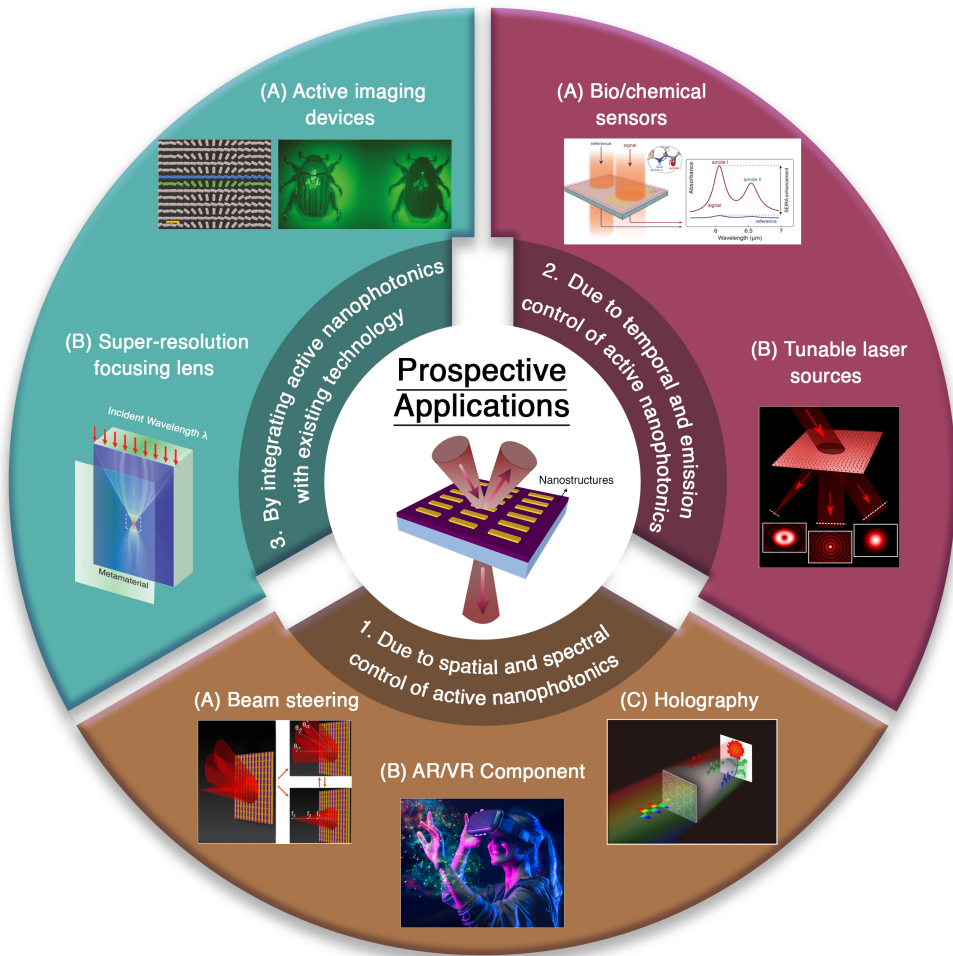


Figure 1.3 Overview of prospective applications of tunable nanophotonic structures based on different advanced approaches. Applications due to spatial and spectral control; beam steering [25], holography [26], AR/VR component. Application due to temporal and emission control; tunable laser sources [27] and bio/chemical sensors [28]. By integrating active nanophotonics with existing technology, applications like super-resolution focusing lens [29], and active imaging devices [30] can be realized.

3. Applications by integrating active NS with existing technologies [39, 40, 41]

- Spatial light modulators
- Ultrafast modulator
- Active imaging devices
- Super-resolution focusing lens

Here, it is essential to highlight that most of the reports of 'active nanophotonics' are proof of concept demonstrations without significant integration into an actual device application. However, significant application-based progress is expected in the coming years.

1.4 Research questions

The aim of this research work is to model, tailor, and enhance the light-matter interactions in nanophotonic structures. The dynamic tailoring of light-matter interactions offers valuable guidelines for practical applications in nanophotonics. The key research questions are:

- What are the mechanisms behind emission enhancement from emitter when placed under strong electric field confinement?
- How active and reversible emission tuning can be achieved using nanophotonics structures?
- How can the strong coupling strength be tuned dynamically via electrical bias in transmission mode?
- What are the key properties for a photonic system to loosen up the sensitivity of plasmonic resonance from its geometrical dependency?

1.5 Outline of the thesis

This thesis presents a framework and platform to model, tailor, and enhance the light-matter interactions in nanophotonic structures. In this thesis, nanophotonic platforms are utilized to control the light-matter interactions actively. The metal-insulator-metal (MIM) structures and epsilon-near-zero (ENZ) materials have been harnessed to achieve these.

The thesis is an anthology of 4 published research work done during my doctoral studies. It includes six chapters. Chapter 1 introduces the topic, Chapter 2 presents the theoretical background, and Chapters 3, 4, and 5 have been structured from publications (I, II, III, IV). A brief discussion on the content of each chapter is as below:

Chapter 1 presents a broad overview of the scope of the thesis for a wide range of audiences. It highlights the importance of photonics and its advancement achieved

by light-matter interactions. Finally, the emergence of active nanophotonics is outlined, and its broad application perspective is showcased.

Chapter 2 briefly presents the theoretical background of plasmonics, MIM-based cavities, and ENZ materials. This chapter lays the theoretical foundation for all the subsequent chapters.

Chapter 3 presents the dynamic control of the emission property of an emitter enabled by tailoring the light-matter interaction. It starts with the motivation behind tuning the emission characteristic of any optical emitter. As proof of concept, the Rhodamine B dye is utilized as an optical emitter. Most importantly, this chapter unravels the underlying mechanism behind emission enhancement, which is well supported by intense experimental results. The emission property of the emitter was tuned using a hydrogel-integrated MIM platform. By changing the ambient humidity, the thickness of hydrogel can be tuned in a controlled manner. This allows tuning of the resonance wavelength of the MIM cavity and hence the dynamic tuning of emission. (Publication I and II)

Chapter 4 addresses one of the critical problems in photonics, active tuning of coupling strength of the photonic systems. The breakthrough is achieved by designing a novel gating scheme that can potentially operate in both the transmission and reflection modes. The chapter starts with a brief motivation followed by the experimental and results section. The results demonstrate the tuning of coupling strength of plasmonic nanostructures and ENZ modes using the devised gating scheme. Furthermore, the detailed fabrication procedures involved in devising the devices are discussed. (Publication III)

In Chapter 5, to increase the flexibility of the plasmonic structure design, the polarization-independent plasmonic nanoantenna was optimized and fabricated on an ENZ substrate, which exhibited two distinct resonances, out of which one lies in the ENZ region. The ENZ substrate's vanishing index of refraction property in its ENZ region was utilized to loosen the sensitivity of resonance toward geometrical perturbations of the structure. (Publication IV)

Chapter 6 summarizes the whole work and discusses the future scope.

2 LIGHT MATTER INTERACTIONS AT DIFFERENT NANOPHOTONIC STRUCTURES

The control and manipulation of light ranging from nano to micro scale is the primary aim of photonics. Indeed, it is of fundamental scientific interest and plays a crucial role in various applications. Yet, in the natural form, the interactions of light with matter are usually weak; they often need to be assisted by well-designed macroscopic media. These engineered macroscopic media are popularly called resonating systems. Several resonating platforms offer unprecedented light confinement, even at extremely subwavelength volumes. In this chapter, the overview of three different resonating platforms, viz. MIM, ENZ media, and plasmonic systems are broadly presented in different sections. Each section provides the theoretical framework to understand the underlying physics of the corresponding resonator platform. Followed by this, a detailed literature review is given where some of the key and seminal works that have utilized these resonating platforms for novel application are discussed.

2.1 Plasmonic systems

Plasmonics is a subset of nanophotonics that concerns the investigation of the oscillation of conduction electrons in metal (plasmons) NSs under the irradiation of light. The plasmons allow the coupling between NSs and the incident light and support the electric field confinement at the nanoscale. Field confinement and enhancement are the heart of novel nanophotonics applications. Therefore, since the emergence of plasmonics, it has been extensively studied and is still a focus of interest for the scientific community. The plasmon modes are categorized into two categories a)

propagating surface plasmons (PSPs), sometimes also called surface plasmon polariton (SPP) b) localized surface plasmons (LSPs). The PSP is the surface electromagnetic wave that may be supported by the metal-dielectric interface. It comprises an electromagnetic wave coherently bounded by the collective motion of free charges at the surface of the metal [42]. Another type of plasmonic mode i.e., LSPs, involve the combined oscillation of the free carrier in a metallic nanoparticle and the associated oscillation of the electromagnetic field. In this dissertation, mainly the LSP mode is utilized.

2.1.1 Theory of localised surface plasmon resonance

The LSPs involve the combined oscillation of the conduction electrons in a metallic NS and associated oscillations of the electromagnetic (EM) field (Fig. 2.1). The resonance wavelength depends on the size, shape, composition, and local optical environment of the nanoparticle [43]. For metallic NSs made of noble metals like gold and silver, the resonance generally occurs in the visible to the near-infrared regime of the spectrum (as in Chapters 4 and 5). LSPs have emerged as an attractive alternative to SPP because of the simplicity of excitation i.e., does not require momentum matching. Furthermore, the ease of NS fabrication due to the advancement of nanofabrication techniques has fueled the applications of LSP. Along with the above-mentioned functionalities, the light confinement at the nanoscale makes localized surface plasmon resonances (LSPRs) more attractive for advanced applications.

The spectral width and the resonance position of LSPR depend on the size, shape and local optical environment of the nanoparticle [43]. For instance, in the case of a single metallic nanosphere placed in a medium with permittivity ε_m , the applied EM field induces a dipole moment p in the sphere whose magnitude is proportional to $|E_0|$, the strength of the applied electric field. The polarizability is an important parameter as it helps to find out the resonance condition of the nanostructure. The polarizability, α , is then defined through $p = \alpha E_0$ and can be derived in the quasi-static approach, where the particles are assumed to be smaller than the wavelength of the light involved, as [44]

$$\alpha = 4\pi d^3 \frac{\varepsilon(\omega) - \varepsilon_m}{\varepsilon(\omega) + 2\varepsilon_m}, \quad (2.1)$$

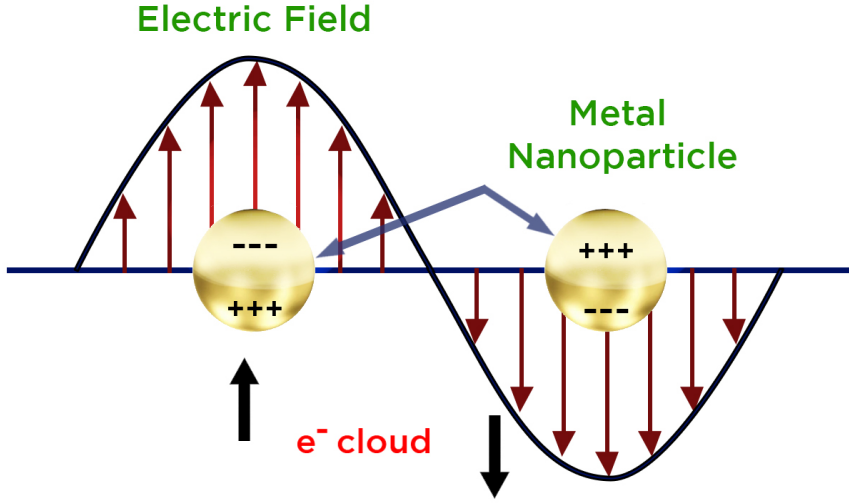


Figure 2.1 An artistic illustration of LSP mode in a metal nanoparticle.

where $\varepsilon(\omega)$ is the relative permittivity of the nanosphere and d is the particle radius.

The spectral position of LSPR can be found by using the condition $\varepsilon + 2\varepsilon_m = 0$. The quality (Q) factor of the LSPR resonance depends on the $\text{Im}(\varepsilon(\omega))$. For metal, the dielectric constant is complex; therefore, it always contains the non-zero value of $\text{Im}(\varepsilon(\omega))$. For most of the applications, strong field confinement (enhanced Q factor) and strong signal strength are required, which is not possible to accomplish using a single NS as its resonance is broad due to radiative damping and dynamic depolarization.

The limitations of the low Q-factor of LSPR in a single nanoparticle case can be overcome by arranging the NSs in an array. The electromagnetic field associated with a nanoparticle's LSP mode may affect the response of its neighboring nanoparticles. Either near-field coupling or far-field coupling can occur with this electromagnetic coupling. The involvement of far-field coupling of LSPs, i.e., their scattered radiation fields, significantly improves the quality and strength of LSPR. When the nanoparticles are arranged randomly, the scattered fields impinge random phase, therefore, do not improve the quality of the scattering field. While on the other hand, when

the nanoparticles are arranged in a periodic way, keeping the periodicity comparable to the wavelength of the incident light, then under appropriate conditions, the scattered fields impinging on a given particle can arrive in phase with the incident light. Physically, in the plane of the array, the scattered fields correspond to the diffraction of the incident light. The light scattered by each nanoparticle into the plane of the array can be coordinated with the plasmon resonance induced by the incident light in the neighboring particle by choosing the appropriate nanoparticle size and shape, along with a suitable array period, to strengthen the resonance in the neighboring particle. In this thesis, especially in Chapter 4 and 5, the array of nanostructures have been used.

2.1.2 Applications of localised surface plasmons

The arrays of sub-wavelength holes on metallic films act as tunable filters where the wavelength selectivity can be tuned by changing the period. Another interesting application for which plasmonic NS has shown extraordinary performance is biosensing. The plasmonic resonance is extremely sensitive to the change in the refractive index of the surrounding medium. Taking advantage of this property, miscellaneous structures have been shown [45, 46, 47, 48] for biosensing applications. Furthermore, integrating plasmonics with novel materials like graphene or index zero material has opened a whole new avenue for exploring new physics and applications. Recently, the plasmonic effects have been shown solely in a thin film of graphene [49, 50]. In short, plasmonics offers inevitable novel opportunities to advance both fields and stimulate new cross-disciplinary approaches to address grand challenges in photonics.

2.2 Metal-insulator-metal Fabry-Pérot resonance

MIM is a planar photonic structure that is structurally simple and has attracted significant attention in the photonic community, and people have shown a diverse range of applications, including polarization control [51, 52], perfect absorption [53, 54], focusing [55, 56], and hologram [57]. MIM consists of a subwavelength thin dielectric spacer sandwiched between an optically thick metal film and a thin metallic layer on top, as shown in Fig. 2.2. The geometrical parameters, such as the thickness of the

dielectric spacer and the thickness of the top metallic layer, play crucial roles in determining the spectral position of the resonances. In this thesis, a finite difference time domain (FDTD) numerical solver (Ansys Lumerical FDTD Solutions) was used to optimize the thickness of an insulator layer of the MIM resonator. In the case of the MIM cavity, the existence of the Fabry-Pérot (FP) mode is the underlying reason for resonance wavelength in the reflection spectra. The FP resonance is resultant of the interference of multiple reflected waves. Analytically, the resonance wavelength can be derived [58] using the transfer matrix method (TMM). The resonance condition is given by the following relation

$$\frac{4\pi}{\lambda_r} nd + \phi_b + \phi_t = 2m\pi, \quad (2.2)$$

where λ_r is the resonance wavelength, n and d are the refractive index and thickness of the dielectric spacer, and m is the integer representing the order of resonance in the MIM cavity. ϕ_b and ϕ_t are the acquired phase shifts upon reflection at the bottom and top metal-dielectric interface, respectively. From Eq.(2.2), it is evident that as the optical thickness (nd) of the dielectric layer increases, λ_r increases i.e. resonance wavelength redshifts.

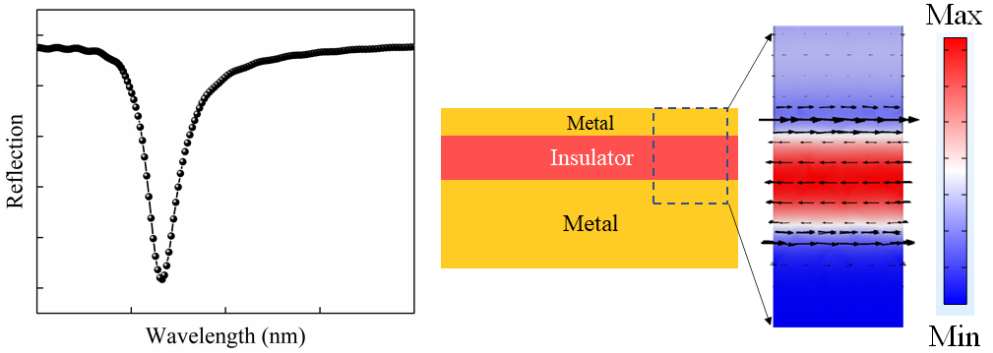


Figure 2.2 Reflection from the metal-insulator-metal structure and its electric field profile.

Furthermore, owing to the structural simplicity and ease of fabrication yet, the properties to fully control the reflected/transmitted light allowed MIM to be used for various range of applications. In laser design, FP resonance determines the lasing wavelength, a cavity in which only light at the resonance wavelength can be emitted. Additionally, enhancing the absorption of light in a controllable manner is extremely important for numerous applications like photovoltaics, photo-detector,

and thermal emitter. In this direction, MIM provided a simple and efficient platform to realize ultra-thin absorbers. The realization of a perfect absorber requires the prohibition of all transmission and reflection channels. For this, the geometrical configuration of MIM structures is ideal. For instance, an optically thick continuous film of metal at the bottom back blocks all the transmission, making the MIM structure a single-port reflective system. Further, a rational design of the topmost metallic layer and carefully choosing spacer thickness eliminate the reflection by destructive interfering gap plasmon and reflected waves. Leveraging this concept, several works were reported as narrow and broadband perfect absorbers [54, 59, 60, 61, 62]. Another application aspect where MIM structures have further advanced the performance metric is color filtering. Due to the unprecedented control over the reflected light with surface engineering, MIM structures are expected to play a pivotal role in both fundamental research and real-world applications.

2.3 Epsilon-near-zero materials and mode

In the natural materials library, there exist few materials that exhibit near zero permittivity. The commonly known materials are those that contain electron gas. The dispersion relation of such materials is given by the Drude model as

$$\varepsilon(\omega) = 1 - \frac{\omega_p^2}{(\omega^2 + i\gamma\omega)}, \quad (2.3)$$

where γ represents the damping rates, and ω_p is the plasma frequency. The real and imaginary components of this complex dielectric function $\varepsilon(\omega) = \text{Re}(\varepsilon(\omega)) + i(\text{Im}(\varepsilon(\omega)))$. Using Eq. (2.3), the real part of permittivity can be written as

$$\text{Re}(\varepsilon(\omega)) = 1 - \frac{\omega_p^2 \tau^2}{1 + \omega^2 \tau^2}, \quad (2.4)$$

where $\gamma = 1/\tau$ have been used. For the frequencies $\omega < \omega_p$, where metals retain their metallic character. However, for the large frequencies close to ω_p , the product $\omega\tau \gg 1$, leads to negligible damping. Therefore, Eq. (2.4) gives

$$\text{Re}(\varepsilon(\omega)) = 1 - \frac{\omega_p^2}{\omega^2}. \quad (2.5)$$

The Eq. (2.5) suggests that the real permittivity goes to zero at $\omega = \omega_p$, indicating the existence of the ENZ wavelength. Since the plasma frequency varies with carrier densities, this type of ENZ behavior can be found over a wide range of frequencies ranging from optical to mid-IR. For example, potassium [63], and silicon carbide [64, 65] exhibit ENZ wavelength at THz and mid-IR frequencies, respectively.

Another class of commonly used materials that exhibits ENZ behaviour are transparent conduction oxides (TCOs) [66, 67, 68]. For example, aluminum-doped zinc oxide (AZO) and indium tin oxide (ITO) show near zero permittivity at near-infrared frequencies (telecom wavelengths). The salient features of TCOs are CMOS compatibility, and active tunability of the ENZ wavelengths, which allows their usage for a diverse range of applications like beam steering [17], strong coupling[69] and designing time-varying metasurfaces [70]. In this dissertation, an ITO is utilized as an ENZ material to investigate and tune the light-matter interactions, which will be discussed in detail in Chapter 4.

In addition to existing natural materials, another approach to realize the ENZ properties is by using artificial materials, which allow independent control and tuning of the permittivity (ϵ) and permeability (μ) at the desired range of frequency. One simple way to achieve the ENZ point is by stacking different thicknesses and permittivity of materials. For example, stacking two materials with dielectric constant ϵ_1 and ϵ_2 and thickness t_1 and t_2 yields the effective permittivity as

$$\epsilon_{eff} = \frac{\epsilon_1 \cdot t_1 + \epsilon_2 \cdot t_2}{t_1 + t_2}. \quad (2.6)$$

By choosing the opposite sign of permittivity, either $\epsilon_1 > 0$ or $\epsilon_2 < 0$ and appropriate thickness of materials, one can readily realize $\epsilon_{eff} \approx 0$.

2.3.1 Properties and applications of ENZ materials

Since, the early investigations of ENZ material, it has attracted significant interest in the scientific community due to its interesting underlying physics. Starting from the simple picture of Snell's law, which formulates the relation between the angle of the incident (θ_1) and emergent (θ_2) from the media with refractive index n_1 and n_2 , respectively as

$$n_1 \sin(\theta_1) = n_2 \sin(\theta_2). \quad (2.7)$$

For ENZ media, $n = \sqrt{\mu\varepsilon} \approx 0$, Snell's law predicts that when a ray is transmitted through ENZ media, the output ray will always be normal to the exit facet as $\theta_{\text{out}} = 0^\circ$. This property of ENZ offered a potential solution for developing a highly directive emitter.

Further, to gain more insight into the dynamics of the electromagnetic waves in ENZ media, Maxwell's equations are the starting point. The time-harmonic source-free Maxwell curl equations can be written as

$$\nabla \times E = i\omega\mu H, \quad (2.8)$$

$$\nabla \times H = -i\omega\varepsilon E, \quad (2.9)$$

where E is the electric field, H is the magnetic field, and μ and ε are permeability and permittivity, respectively. By simple inspection, for index near zero media ($\varepsilon \approx 0$ or $\mu \approx 0$), the Maxwell curls equations yield the decoupling of electricity and magnetism, as $\nabla \times E = 0$ or $\nabla \times H = 0$. Vanishing the curl of electric or magnetic fields physically means nearly constant phase distribution of electric or magnetic fields in a medium with near zero permittivity or permeability. Intuitively, the decoupling behavior can also be seen as the “stretching” of the wavelength. Since the wavelength (λ) of the electromagnetic field inside a media can be written as

$$\lambda = \frac{\lambda_0}{\sqrt{\mu\varepsilon}}, \quad (2.10)$$

where λ_0 is the finite wavelength in free space. Clearly from Eq. (2.10), at ENZ wavelength, λ becomes infinite; consequently, propagation constant ($k = 2\pi/\lambda$) becomes zero, implying that waves do not accumulate phase as it propagates to ENZ media. The stretching of wavelength further indicates the weakening connection between frequency (temporal) and wavelength (spatial) domains, which is an interesting and important aspect of ENZ media. Furthermore, this property provides unprecedented control of both domains (spatial and temporal) of electromagnetic waves, which is the basis of numerous photonic applications.

Looking more closely at Maxwell's curl equations (Eq. (2.8) and Eq. (2.9)), for a medium with a vanishing permittivity ($\varepsilon = 0$), the magnetic field becomes curl-free ($\nabla \times H = 0$) which further yields the Helmholtz's wave equation as $\nabla^2 E = 0$. This indicated that the electric field distributions inside the ENZ media are “static-like”.

The static behavior can also be explained by the phase velocity ($v_p = c / \sqrt{\mu\varepsilon}$), which diverges at ENZ wavelength, which physically means the excitation of static-like field distributions for monochromatic steady state time-varying fields.

Most importantly, ENZ materials are known for enhanced electromagnetic field confinement which boosts the nonlinear effects. In fact, ENZ materials empower two of the main requirements for nonlinear effects, viz., phase matching and high field intensities. Among these two, the phase-matching condition was explained in the above discussion. The lack of phase progression inside the ENZ media allows for the fields to build up coherently. For high field intensities, typically plasmonic structures are employed to confine the light into a small region of space. In stark contrast, the ENZ media can provide strong field confinement over a large area, while ensuring the phase-matching condition. Mathematically, it can be explained by using the boundary conditions. To satisfy the continuity for the longitudinal component of the displacement electric field ($D_l = \varepsilon_l E_l$), the electric field inside the ENZ media increases significantly. To illustrate this, consider an interface of two media, one with permittivity ε_1 and the other with permittivity ε_{ENZ} . From the continuity of the longitudinal component of the displacement field, the strength of the electric field (E_1) inside the ENZ media can be derived as

$$E_{ENZ} = \frac{\varepsilon_1 E_1}{\varepsilon_{ENZ}}. \quad (2.11)$$

From Eq. (2.11), it is evident that E_{ENZ} is large at ENZ point due to vanishing permittivity ($\varepsilon \approx 0$).

It was Ziolkowski's seminal work [71], which stimulated the discussion of ENZ media. This work provided an in-depth analysis of the field dynamics in the ENZ structure and showed that the field's distributions in the region with near-zero parameters exhibit static. This remarkable feature of ENZ media stimulated the discussion of tunneling electromagnetic waves through a narrow medium. The theoretical prediction came in 2006 [72] followed by the experimental demonstration in microwave frequencies [73, 74]. In addition to electromagnetic tunneling, developing highly directive emitters was also a big motivation for ENZ media. Also, Enoch's work [75] showed that the phase and amplitude uniformity associated with the ENZ media directly leads to highly directive beams.

In addition to enhancing the radiation/emission directivity, the phase and amplitude uniformity of ENZ media can empower the beam-steering and beam-forming

applications. Furthermore, similar principles can be adapted to arbitrarily shape the scattering pattern's phase and amplitude profile, which could also be utilized for lensing purposes. Indeed, harnessing these properties of ENZ media, several works [76, 77, 78, 79] on beamforming and lensing were reported. Interestingly, the uniformity of phase and high field confinement in ENZ media was also exploited to enhance the spontaneous emission from the fluorescence molecules [80].

The electric flux densities vanish in the ENZ media as $D = \varepsilon E$, which induces a strong discontinuity of the normal component of the electric field at the interface that leads to strong field confinement at the interface [81]. Also, leveraging this unique boundary effect, unprecedented control in guiding the displacement current can be achieved, which is vital for photonic integrated circuits. For instance, if an air groove is carved in an ENZ medium, the displacement current will be zero everywhere except in the air groove region. Thus, by patterning arbitrarily shaped air grooves, displacement currents can be guided similarly in which conducting wires guide the flow of electrons in an electronic circuit. This unique feature of ENZ medium has stimulated the field of photonic integrated circuits, and various works reported [82, 83, 84, 85] to realize the photonic integrated circuits using ENZ media.

Furthermore, owing to vanishing characteristics of electric and magnetic fields at the ENZ media boundaries, geometrical-invariant resonant cavities [86] were shown whose resonance frequency is independent of the geometry, including shape, size, and topology. Due to the ENZ layer's vanishing index property, it was used as a substrate in chapter 5, and it has been demonstrated that the resonance wavelength shift became nearly independent of antenna length near the ENZ wavelength. Recently, ENZ thin film has received significant interest due to its ability to support ENZ modes, an ENZ layer (40nm) that supports ENZ mode was used in chapter 4. These ENZ modes enhance the interaction between nanostructure and semiconducting structures, phonon excitation, and thermal emission. Thus, ENZ thin film has proven to be a simple and useful candidate for studying light-matter interaction. Due to its simplicity, numerous works have been reported [17, 66, 87] by integrating ENZ thin film either with plasmonic nanostructures or emitter to several potential applications.

2.3.2 ENZ mode

Recently, it has been observed that an ultra-thin ENZ material supports a unique surface mode known as ENZ mode [88]. The salient features of ENZ mode are the following: (1) It lies below the light line, which means it is nonradiative in nature. Therefore, it is confined within the thin film. (2) ENZ modes are long-range surface plasmon polaritons that exhibit nearly flat dispersion at the ENZ wavelength as the thickness of ENZ material goes to zero. (3) ENZ mode allows strong field confinement, therefore, facilitating enhanced light-matter interactions.

The underlying physics of ENZ modes can be understood by considering a simple three-layer structure, as shown in Fig. 2.3

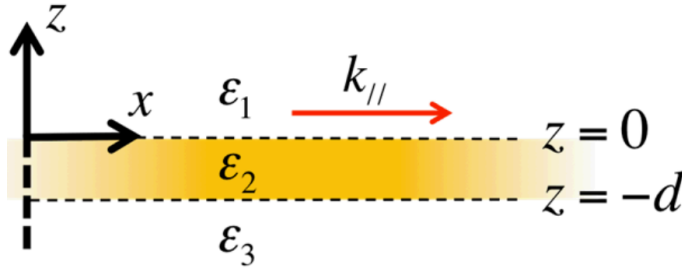


Figure 2.3 Three-layer geometry with permittivity ϵ_1 , ϵ_2 and ϵ_3 respectively. [88]

A thin film of material with relative permittivity ϵ_2 and thickness d is surrounded by two semi-infinite regions of dielectric constants ϵ_1 and ϵ_3 . For ease of calculation, the dispersion of sandwiched material is modeled using a simple Drude model as shown in Eq. (2.3). It is evident from Eq. (2.5) that at $\omega = \omega_p$, permittivity vanishes, i.e., $\epsilon = 0$, which leads to the existence of ENZ mode. Furthermore, this mode satisfies the following dispersion equation

$$1 + \frac{\epsilon_1 K_{z3}}{\epsilon_3 K_{z1}} = i \tan(K_{z2} d) \left(\frac{\epsilon_2 K_{z3}}{\epsilon_3 K_{z2}} + \frac{\epsilon_1 K_{z2}}{\epsilon_2 K_{z1}} \right), \quad (2.12)$$

here, $K_{zi} = (\epsilon_i \omega^2)/c^2 - k_{||}$ is the longitudinal component of mode in respective medium $i = 1, 2, 3$ and $k_{||}$ is the transverse component of wave vector. The Eq. (2.12) can be solved for real $k_{||}$ and complex ω to capture the transient radiative decay nature of ENZ mode. Fig. 2.4 depicts the solution of Eq. (2.12), i.e., dispersion curves for both the short- and long-range surface plasmon modes of thin ENZ material.

From Fig. 2.4 it is clear the long-range polariton mode is ENZ mode as the dispersion becomes nearly flat for a large range of transverse wave vectors ($k_{||}$) at ENZ frequency or plasma frequency.

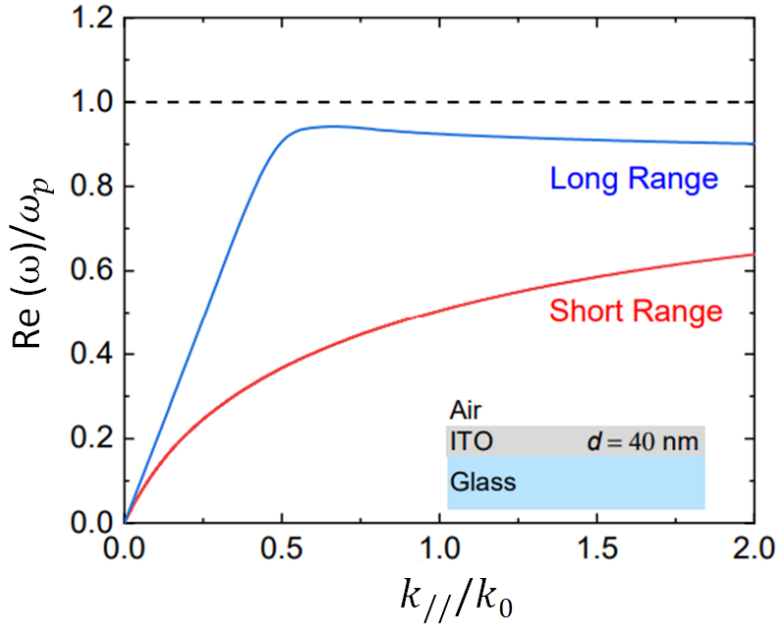


Figure 2.4 Dispersion relation of the three-layered (air - 40 nm ITO - glass) system. [89]

3 ENHANCED AND ACTIVE TUNABLE EMISSION

This chapter is based on Publication I and II, and here metal–insulator–metal (MIM) structures are harnessed to unveil the underlying emission mechanism of photoluminescence dye and to achieve tunable emission.

The MIM nanocavity has provided an opportunity to improve the performance of photonic devices. However, the basic physics and mechanisms involved in the emission enhancement obtained from such cavities are not very clear and are under debate. In the study from, Prayakarao *et al.*, the effect of the dielectric thickness of the MIM cavities on the spontaneous emission (SE) rate enhancement [90] has been shown. Also, Nyman *et al.* reported far-field fluorescence enhancement in a dye-integrated MIM structure [91]. They displayed that an enhanced emission is attributed to both the Purcell and excitation rate enhancement. Nevertheless, in the above-mentioned studies, the dyes used were with low Stokes shift. In such experimental conditions, the participation of each phenomenon in the emission enhancement was not well separable, and exact mechanisms for the enhanced SE were not revealed.

In this chapter, the mechanisms behind emission enhancement have been revealed by designing and investigating the fluorescent dye integrated with various MIM cavities. Furthermore, the dynamically controllable emission is of great importance for the applications like bio-sensing, imaging, and optoelectronics. Traditionally, methods to achieve dynamically controllable emission [92, 93, 94] are limited due to complex fabrication processes or irreversible tuning. Also, Serpe *et al.* have extensively worked on tunable etalons where an insulator layer comprises a hydrogel, which responds to different stimuli and displays color tuning [95, 96]. However, all aforementioned studies do not converse emission tuning. To demonstrate the dynamic and reversible emission tuning, a photo-luminescent hydrogel, obtained via covalent

functionalization with a fluorescent dye, has been integrated into a MIM cavity as a tunable platform. The proposed approach is reversible, scalable, and easily integrable and has the potential to develop tunable photonic devices. The advantages of incorporating MIM structures in these studies are as follows:

1. The inclusion of MIM structure with dye molecules provides large area interaction of the dye with the confined electromagnetic field that yields high-intensity emission. Compared to plasmonic nanostructures such as nanoantenna or discs, which require careful alignment of dye molecules with the nano-sized electromagnetic field hot-spot, MIM simplifies the experimental complexity.
2. Ease of spectral tunability of resonance wavelength - Compared to standard plasmonic devices, which require periodicity modification or intense geometrical parameter altering, the spectral position of resonance in MIM can be easily tuned by changing the thickness of the dielectric layer. In addition, this also allows an extensive spectral range and fine-tuning of resonance wavelength.
3. Simplicity of achieving active control - In comparison to a traditional plasmonic structure which requires a complex fabrication process to achieve dynamic tuning on spectral resonance, the realization of active spectral control in MIM structures is easy. For instance, using hydrogel as a dielectric spacer allows an extensive spectral range and reversible tuning of resonance wavelength.

3.1 Organic dye integrated in metal-insulator-metal structure

3.1.1 Emission enhancement in photonic environment

Spontaneous emission is pivotal for determining the performance of any optoelectronic devices, including smart displays, light sources, lasers, and solar cells. For a long time, it was thought that spontaneous emission was an inherent and unchangeable property of an emitter. However, several studies have shown that by changing the electromagnetic environment of an emitter, spontaneous emission can be

modified. This has opened a whole new avenue in photonics, further fuelled by the advancement of nano-photonics and the development of advanced fabrication techniques. The underlying physics to explain the emission enhancement can be explained by the Purcell factor, defined as the ratio between the modified and free space emission rates of an emitter. The Purcell factor can be written as

$$F_p = \frac{3Q\lambda^3}{4\pi^2 V_0}, \quad (3.1)$$

where, Q is the quality factor of cavity or resonator, λ is the emission wavelength and V_0 is the mode volume of resonance mode. From the Purcell formula, it is clear that to achieve a large Purcell factor, low mode volume or large quality factor of cavity is required. The applicability of resonant systems often constrains operational bandwidth and fabrication complexity. In addition, one of the important points is that, so far, most of the studies have focused on improving spontaneous emission by increasing the emission rate of the emitter.

In this thesis, increasing the absorption rate is integral to improving emission efficiency has been demonstrated and utilizing the MIM structure was advantageous due to the ease of tuning the cavity resonance to match either the absorption or emission wavelength of the emitter, along with fabrication simplicity. Further sections provide a detailed discussion on unveiling the underlying physical mechanism for enhancing the emission of an emitter.

3.1.2 Structure optimization and fabrication

The diagrammatic representation of the fabricated MIM cavity is shown in Fig. 3.1, where the thicknesses of the top and bottom metallic layers were fixed as 35 nm and 150 nm, respectively. Silver (Ag) has been used for the metal layers because of its unique optical properties, such as excellent plasmonic properties and lower plasmonic losses. Both the Ag layers were deposited using an e-beam metal evaporator, and the thickness of each layer was confirmed by a profilometer. The LDS 798 dye was dissolved in Poly(methyl methacrylate) (PMMA) to make the homogeneous solution, and for proper mixing, an ultrasonicator was used. Then, the PMMA solution was spin-coated as a dielectric layer on top of the 150 nm Ag layer. To tune the MIM cavity resonance, the thickness of the dielectric layer was varied, and the

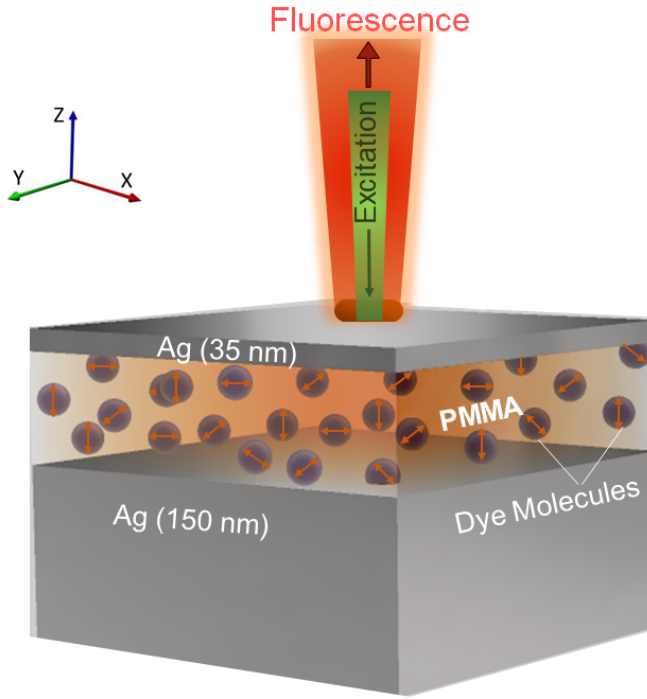


Figure 3.1 An artistic illustration of MIM cavity comprise of Ag - (PMMA+LDS 798 dye) - Ag

dielectric layer's thickness was optimized using FDTD numerical simulation.

To emulate the experimental scenario, in simulation, periodic boundary conditions both in the x and y directions were implemented, followed by a perfectly matched layer (PML) in the z-direction. The propagation direction of the incident plane wave was z-direction, to excite the MIM Fabry Perot resonance modes. The reflection profile was further recorded using the power monitor. The simulated reflection spectra for different thicknesses of the dielectric (PMMA) layer are as depicted in Fig. 3.2a. Based on these simulation results, the thickness of the PMMA layer was chosen as 140 nm and 190 nm, which yields cavity resonance at 567 nm (MIM-I) and 710 nm (MIM-II), respectively, as indicated by white dashed lines in Fig. 3.2a. The corresponding simulated reflection spectra for both of these cavities are as shown in Fig. 3.2b. These specific thicknesses of PMMA were chosen to match MIM cavity resonance with the absorption and emission spectra of LDS 798 dye molecules.

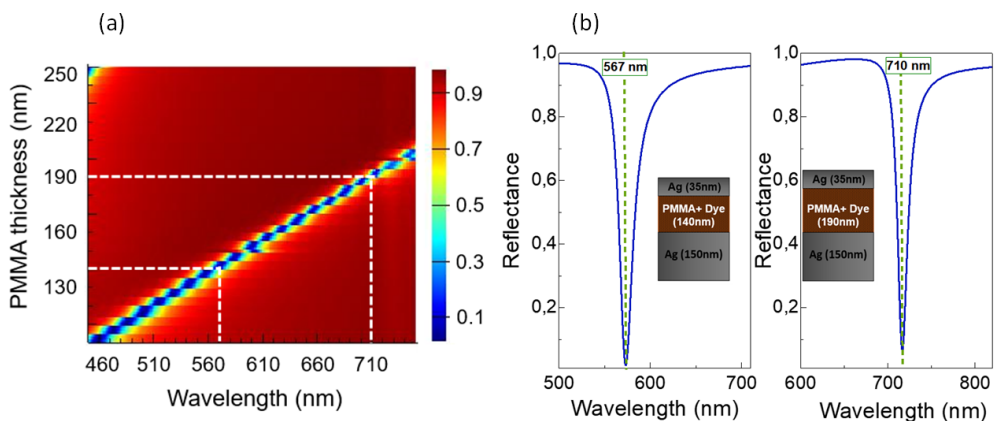


Figure 3.2 a) The color plot of simulated reflection spectra for various thicknesses of PMMA. The white dashed lines highlight the resonance wavelengths corresponding to PMMA thicknesses 140 nm and 190 nm. b) Simulated reflection plot for MIM cavity with PMMA thickness 140 nm and 190 nm. The inset shows the artistic diagram of the MIM cavity.

3.1.3 Optical characterization: reflection and emission

The MIM cavities with the optimized parameters were fabricated and experimentally characterized by measuring their reflectance. In addition, the fluorescent dye (LDS 798) was characterized by measuring its absorption and emission spectra. Figs. 3.3a and b show the experimentally recorded absorption (solid black line) and emission spectra (solid red line) of the LDS 798 dye molecules, which confirms the absorption and emission peaks at 567 nm and 670 nm, respectively. The experimentally recorded reflection spectra for MIM-I and MIM-II are shown by solid blue lines in Fig. 3.3, which showed a good agreement with simulated reflectance results (Fig. 3.2b). Notably, the resonance of the MIM-I cavity has a strong overlap with the absorption spectrum of an emitter, as shown in Fig. 3.3a, whereas the MIM-II cavity's resonance overlaps with the emission spectrum and barely overlaps with the absorption spectrum as shown in Fig. 3.3b.

The MIM cavity confines the light into the dielectric layer at resonance wavelength. To study the effect of strong field confinement over the emission properties of LDS 798 dye, intensity counts were experimentally recorded using the PL measurement. In PL measurement, LDS 798 dye was excited with 532 nm and Figs. 3.4a and b show measured emission intensity for MIM-I and MIM-II, respectively. The remarkable emission enhancement in dye molecules integrated MIM-I cavity is

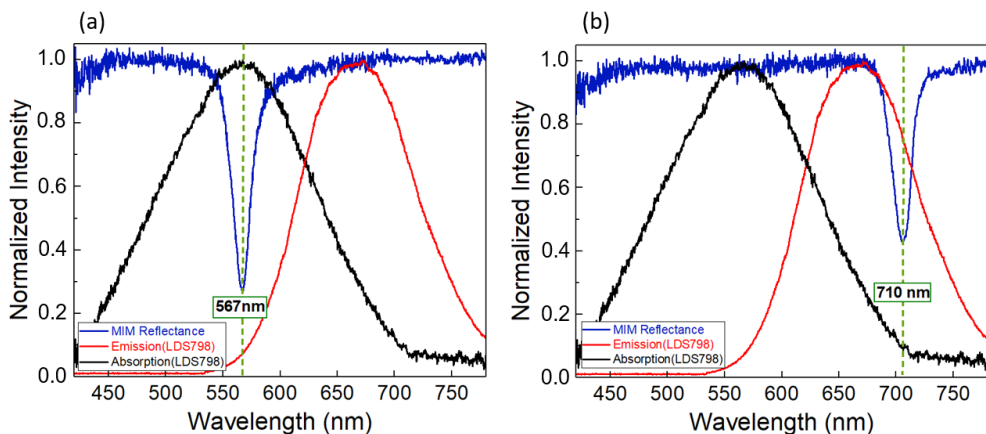


Figure 3.3 Experimentally recorded reflection spectra indicated with solid blue lines (a) for MIM-I cavity and (b) MIM-II cavity. The absorption and emission of LDS-798 dye are marked by black and solid red lines, respectively. [97]

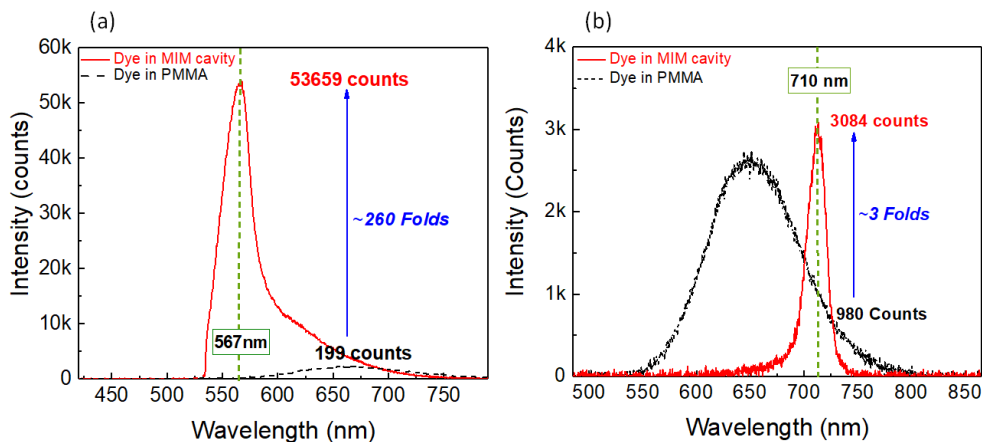


Figure 3.4 PL spectra of LDS 798 dye integrated with (a) MIM-I cavity and (b) MIM-II cavity. The emission spectra for bare LDS 798 dye spin-coated on glass substrate for reference is highlighted by dotted black line. [97]

shown in Fig. 3.4a. Nearly 260-fold PL enhancement was recorded from the dye molecules integrated with MIM-I, whereas dye integrated with MIM-II cavity yields only 3-fold emission enhancement. The resonance band of MIM-I strongly overlaps with the absorption spectrum of dye and partly with the emission spectrum. Therefore, the higher enhancement in the case of the MIM-I cavity can be attributed to an unequal contribution of both the Purcell factor enhancement and absorption rate enhancement. on the contrary, the resonance of MIM-II poorly overlaps with emis-

sion and barely with the absorption band. Thus, MIM-II contributes to the emission enhancement via Purcell factor enhancement.

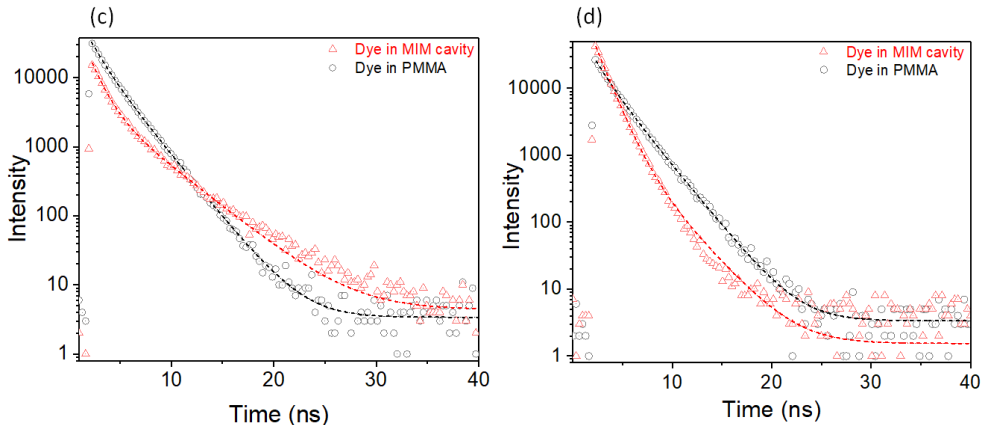


Figure 3.5 Time resolved PL intensity results for LDS dye embedded in (a) MIM-I cavity and (b) MIM-II cavity. The fluorescent lifetime for reference dye-coated sample (on bare glass substrate) is shown by the dotted black line. [97]

Furthermore, to unveil the effect of the MIM cavity on the emission property of dye, the transient PL dynamics were recorded using time-resolved fluorescence spectroscopy. Figs. 3.5a and b depict the transient decay dynamics. For comparison, the decay dynamics of LDS 798 dye were recorded for all the cases, viz. LDS 798 integrated with MIM I and MIM II cavities and reference sample (LDS 798 dye embedded in only PMMA). The bi-exponential function was used to fit the transient kinetics of the reference and MIM integrated dye sample and obtained τ_1 and τ_2 values corresponding to different processes involved in the decay dynamics. The rigid matrix of PMMA hinders the large amplitude motion and inter-molecule beatings of the excited state molecules of LDS 798 dye, and the dense environment of PMMA increases the probability of the aggregation of the dye for monomers. The combination of the above-mentioned reasons results in two fluorescent lifetimes components rather than a single component, which mostly occurs for LDS dye molecules in less viscous solvents. The bi-exponential fit to the time-resolved PL of the dye molecules in the case of the reference sample denoted with black circles yields $\tau_1 \approx 1.144$ ns and $\tau_2 \approx 2.408$ ns, where the first component accounts for fast decay while the second component represents the slow decay process. The integration of dye molecules with the MIM-I cavity imparts a reduction in the fast decay component ($\tau_1 \approx 1.074$ ns); however, the slow component gets elongated ($\tau_2 \approx 3.691$ ns) as shown in Fig.

3.5a (red triangles). The reduction in the fast component can be ascribed to the enhanced emission rate due to the Purcell effect. In contrast, enhancement in the slow component occurs due to the leakage radiation from the MIM-I cavity. This slow leakage field comes from the fact that the MIM-I cavity's resonance (567 nm) is far from the emission peak of the dye (670 nm, Fig. 3.5a, solid red line) that does not couple with the MIM-I cavity. Furthermore, the lower thickness (35 nm) of the top metallic layer is unable to effectively confine the emission of non-resonant dye molecules and further supports the slow leakage.

On the other hand, the characteristic lifetime components for LDS 798 integrated with MIM-II cavity are $\tau_1 \approx 0.99$ ns and $\tau_2 \approx 2.404$ ns. Here, the reduction in the first component (τ_1) attributes to the emission rate enhancement due to the Purcell factor, while the τ_2 decay component remains unchanged (similar to the reference sample). Comparing the fast components of the excited dye molecules in both cavities reveals a similar coupling strength. Notably, a similar coupling strength was observed even though the spectral overlap between the emission spectra of dye molecules and resonance of MIM cavities were not similar. It further confirms that the Purcell enhancement gateway leads to similar intensified emissions in both the MIM cavities. Importantly, from Fig. 3.3a, it is evident that only a small portion of emission from dye molecules coupled with the MIM-I cavity, and the majority of the fluorescence emission leaks through the cavity, which confirms that the multi-fold (260 folds) emission enhancement occurs in MIM-I cavity comes from the excitation rate enhancement and the contribution of Purcell enhancement was very subtle. Therefore, excitation rate enhancement was a preeminent channel that contributed towards multi-fold emission enhancement in the MIM-I cavity.

Moreover, to explore the underlying physics for multi-fold enhancement, numerical simulations were performed, and the electric field confined inside nanocavities was calculated. Figs. 3.6a and b show the electric field contour plot of both the MIM cavities at 567 nm and 710 nm resonance wavelengths, respectively. The strong electric field confinement into the dielectric layer suggests that the incorporation of dye molecules with the designed MIM cavities may lead to fluorescence enhancement.

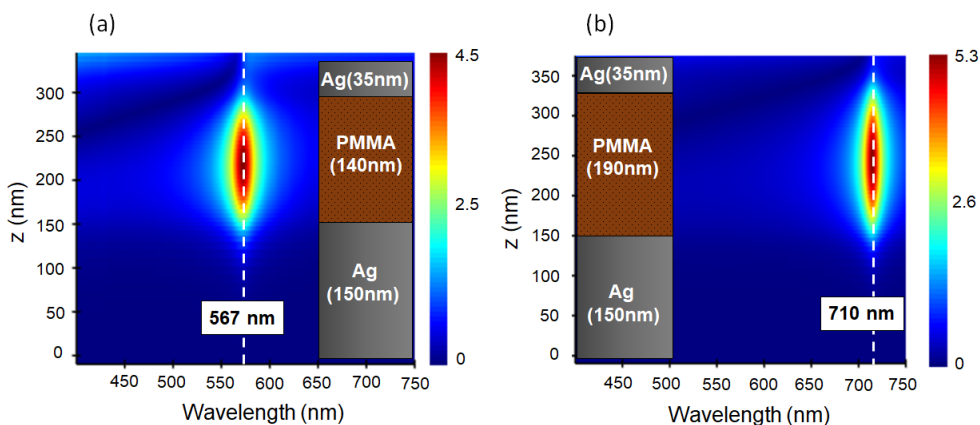


Figure 3.6 The electric field contour simulated for (a) MIM-I cavity and (b) MIM-II cavity, and the inset shows the diagrammatic representation of both cavities. [97]

3.1.4 Mechanisms behind emission enhancement

The enhanced emission in the dye-integrated compound system is primarily due to two mechanisms, (1) the confinement of the EM field between two metallic films enhances the Purcell effect, and (2) the intense cavity mode enhances the excitation rate. As the overall enhancement is the product of Purcell and excitation rate enhancement, therefore mechanisms mentioned earlier results in emission enhancement of the system. The simultaneously overlapping absorption and emission spectra of an emitter with the MIM cavity resonance stimulate the opportunity to exploit both mechanisms to maximize the emission efficiency of the system. Conclusively, an emission property can be engineered and enhanced not only through enhancing the Purcell factor but, more importantly, by enhancing the excitation rate of an emitter.

3.2 Organic dye integrated in hydrogel-based metal-insulator-metal structure

Manipulating the optical properties of an emitter is of paramount importance for developing efficient light sources for advanced nanophotonic devices, fluorescence microscopy, and various optoelectronic applications. Actively controllable photoluminescence (PL) is potent for multiple applications, from bio-sensing to imaging.

Previous studies have shown either the passive control of emission or actively tunable emission with limitations such as lack of reversibility, complex fabrication processes, or exhibiting small spectral tunability. In addition, complicated and tedious fabrication procedures hamper the translation of tunable emissions to real-world applications. A photo-luminescent hydrogel was integrated with a MIM cavity as a tunable platform to circumvent this and demonstrate active emission tuning. The fluorescent hydrogel was obtained via covalent functionalization with rhodamine B (RhB) as an emitter (further details are in the following sections). This work reflects a timely and essential study that would immensely enrich a wide range of photonics community that requires on-demand optoelectronic tunability ranging from flat optics to integrated circuits. Thus, our findings will create a new direction toward dynamically mutable reversible photonic devices and contactless optical sensors.

3.2.1 Hydrogel synthesis and fabrication of metal-hydrogel+dye-metal structure

The schematic of desired Metal-Hydrogel+Dye-Metal (MIM) structure with thicknesses of the top and bottom metallic layers were 30 and 100 nm, respectively, as depicted in Fig. 3.7. The bottom 100 nm Gold (Au) layer works as a reflector, and the top 30 nm layer is partially transparent, which allows the collection of reflected light. The fabrication process of MIM begins with cleaning 1 cm \times 1 cm fused silica substrates by sonicating them in acetone, and isopropanol for 10 minutes, followed by a blow-dry and oxygen plasma treatment. Next, using e-beam evaporation, an adhesive layer of 1 nm Ti was deposited, followed by an Au layer of 100 nm. The next step was the synthesis and deposition of an insulator (PNIPAm-BP) layer, this material was selected as an insulating layer owing to its excellent swelling [98] and film forming [99] properties. The thin hydrogel layer and its swelling/deswelling allow the modulation of hydrogel layer thickness, hence the cavity resonance and emission tuning. For forming the insulator layer, the primary steps were 1) PNIPAm-BP-RhB Co-polymer Synthesis and then 2) Solution preparation. PNIPAm-BP-RhB Copolymer was synthesized using commercially available N-Isopropylacrylamide (NIPAm) and azobis(isobutyronitrile) (AIBN). The AIBN was recrystallized from methanol before use. The RhB acrylate was synthesized from commercial RhB. Benzophenone acrylamide (BP), and the copolymer were prepared by using the similar

process explained in [19] yielding the copolymer with composition 98.5:2.0:0.5 (NI-PAm/BP/RhB).

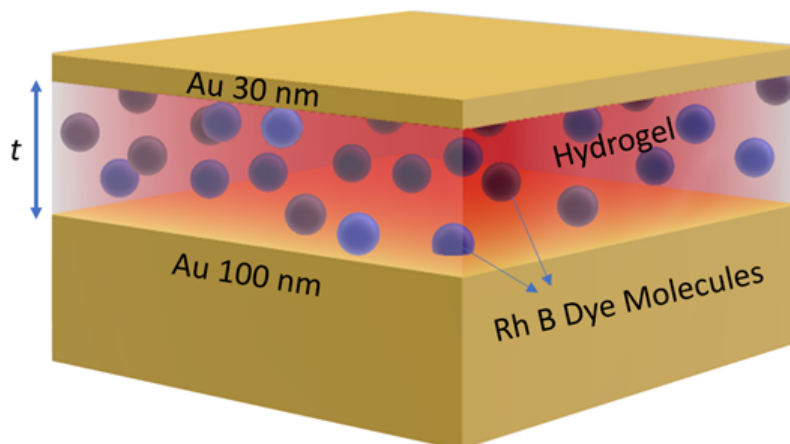


Figure 3.7 Schematic of the RhB-containing hydrogel incorporated into the MIM cavity.

Two different concentrations of 20 and 30 mg/ml were prepared by dissolving PNIPAm-BP-RhB copolymer in filtered (filtered using 0.2 μm pore sized PTFE Teflon filter) 94% ethanol. For better and homogeneous dissolution of the copolymer in ethanol, 10 min of sonication and magnetic stirring for 1 hour at 1400 rpm, 50°C was done. The solutions were filtered through a 0.45 μm pore-sized PTFE filter; then, the solution was spin-coated on a glass substrate to optimize the desired layer thickness of the dye-incorporated hydrogel. Later, to have a uniform and well-distributed spin-coated hydrogel layer on the final samples, the Au-coated samples were treated with oxygen plasma (20 min, 30 W RF power, 1000 mTorr O_2) to activate the surface. Subsequently, hydrogel layers of different thicknesses were coated by using different spin-coating parameters. Dynamic 2-step spin-coating was used as (1) 10 seconds at 150 rpm, 100 acceleration for dispense and pre-distribution of solution on the sample, and (2) 30 seconds at 2000rpm/3000rpm/4500rpm, 1000 acceleration to form the coatings. To obtain 90 and 110 nm hydrogel thicknesses, the 20 mg/ml solution was used, and for higher thicknesses (135 to 160 nm), 30 mg/ml solution was utilized. The samples were baked at 50°C in a vacuum for 45 minutes. Thenceforth, the spin-coated samples were photopolymerization under UV light (365 nm from CoolLED pE-4000), and the time required for complete crosslinking of PNIPAm-BP-RhB copolymer was 40 minutes. The polymerization time was optimized and confirmed by the disappearance of the 301 nm peak in the optical transmittance spec-

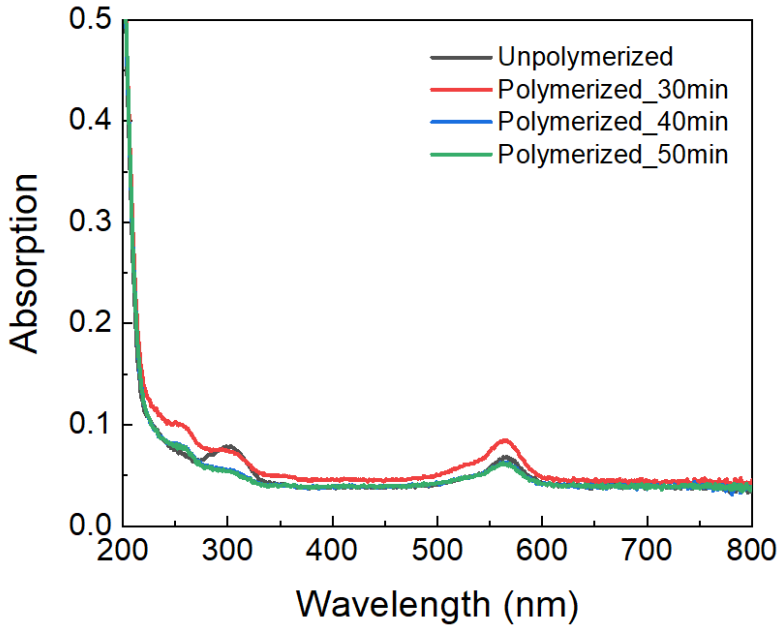


Figure 3.8 Measured transmittance spectra of reference hydrogel coatings on a glass substrate to confirm photopolymerization time.

tra of the reference hydrogel coatings on the glass as shown in Fig. 3.8. The MIM structure's top Au layer (25-30 nm) was deposited on top of the hydrogel layer by a thermal metal evaporator.

3.2.2 RhB dye characterization and optimization of MIM design

As discussed in section 3.1, the simultaneous overlap between cavity resonance and dye's emission and absorption is imperative for achieving enhanced emission. This enhanced emission is the product of Purcell enhancement and excitation rate enhancement (also discussed in Publication I). This knowledge helps in the MIM design, particularly the thickness of an insulator layer. The dye characteristics i.e. absorption and emission were measured from the reference sample (dye coated on glass substrate), and as shown in Fig. 3.9a RhB exhibit a small Stokes shift of ≈ 30 nm. The black dotted curve presents the absorption spectra (peak at 563 nm), and the solid red line represents the emission (peak at 592 nm) of RhB.

Fig. 3.9a propose that if the cavity resonance falls in the wavelength range of 540

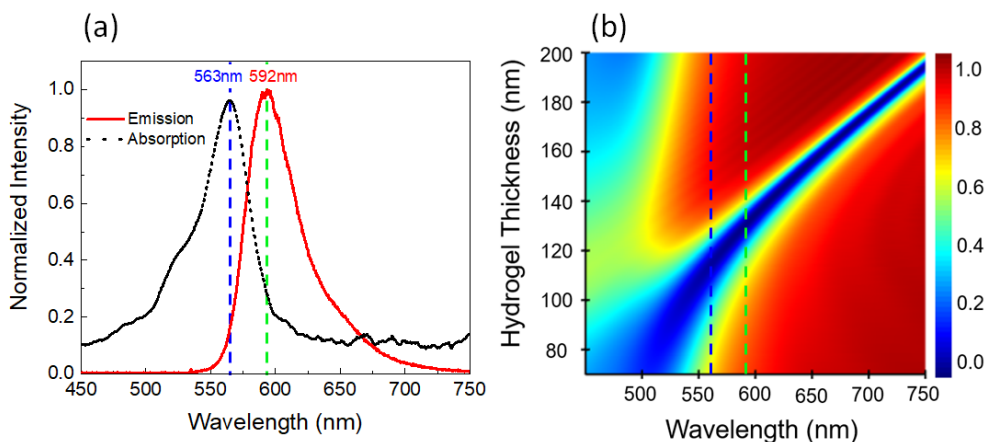


Figure 3.9 (a) Emission (solid red line) and absorption (dashed black line) spectra of fluorescent dye RhB (b) Contour plot of reflection spectra simulated for various thickness of hydrogel. [18]

to 650 nm, then it is optimal for its simultaneous overlap with the emission and absorption of RhB. The major factor which decides the wavelength of cavity resonance is the thickness of the insulator layer in a MIM cavity. So the next obvious step was numerical simulations to identify the suitable thickness range of the hydrogel layer. In the simulation, to minimize the simulation time, symmetric and antisymmetric boundary conditions were applied in the x and y directions. Moreover, to remove the unwanted reflections, PML was used along the z direction. The resonance cavity mode was excited by launching a plane wave. The insulator layer (hydrogel) was modeled with a refractive index of 1.503 [100] and to define the material for the top and bottom layer i.e. Au, Johnson and Christy data set [101] was utilized from the in-built material library of FDTD. The simulation result, reflection from the MIM cavity at varying hydrogel thicknesses, is as depicted in Fig. 3.9b, and crest positions of absorption and emission of RhB are also indicated by blue and green dashed lines, respectively. Therefrom, the dielectric thickness range of ≈ 90 to ≈ 150 nm was optimized using both the dye characteristics (Fig. 3.9a) and the MIM cavity resonance (Fig. 3.9b).

3.2.3 Passive emission tuning

Before the demonstration of real-time emission tuning, passive emission tuning is demonstrated. To demonstrate emission tuning without real-time control, the first

step was to inspect the effect of overlap extent between dye characteristics and a cavity resonance on the emission intensity. For this investigation, a range of MIM cavities with dry hydrogel thicknesses (i.e. thickness at room humidity) between ≈ 90 to ≈ 160 nm were fabricated. The captured optical images of MIM cavities with different cavity resonances exhibit different bright colors as per their reflection as depicted in Fig. 3.10.

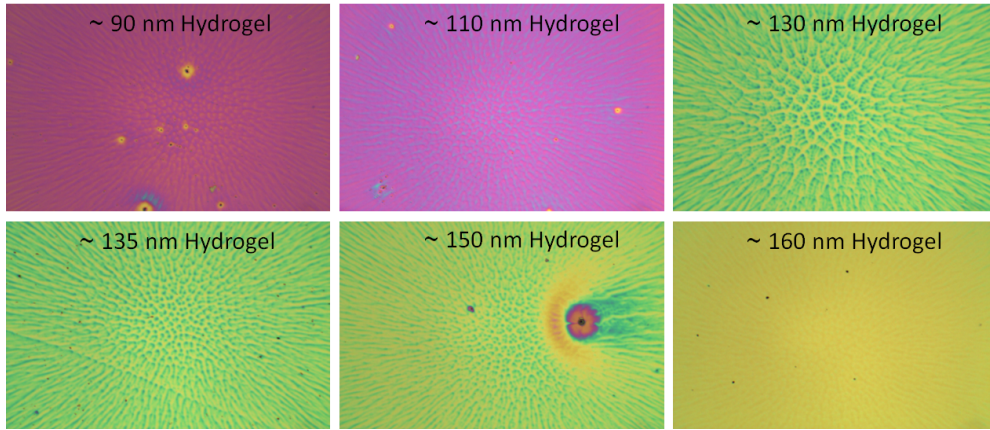


Figure 3.10 Optical images of the MIM samples with different hydrogel thicknesses. The thicknesses of hydrogels were measured using a profilometer.

For the reflectance measurement of all the fabricated MIM cavities at room conditions (23 °C, 28% room RH), a multifunctional WITec alpha300C confocal microscope was utilized. The samples with different hydrogel thicknesses were irradiated with a broadband light source through a 20X objective. Thenceforth, to see the response from samples, the light reflected from the sample's bottom reflector was collected through the same 20X objective and coupled to spectrometers via an optical fiber. The Ocean Optics Flame UV-vis spectrometer was used to detect a response in the spectral range of 400 nm to 900 nm. The reflectance spectra measured from different MIM cavities as depicted in Fig. 3.11a. From the acquired reflectance results, the redshift in MIM cavity resonance with an increase in the hydrogel thickness was observed.

Subsequently, the PL measurement was performed to observe the change in emission of the emitters coupled with different MIM cavities with passively varying hydrogel thicknesses. For this, a 532 nm laser was used to excite the samples to attain the emission peak intensity of the RhB dye incorporated within various MIM cavi-

ties. The response from the samples was coupled to an optical fiber connected to an Ocean Optics Flame UV-vis spectrometer, and the steady-state PL spectra of RhB in the different MIM cavities are shown in Fig. 3.11b. As shown in Fig. 3.11a the MIM cavity with a dry hydrogel thickness of 90 nm exhibits cavity resonance at 540 nm, which strongly overlaps with the absorption spectrum and barely with the emission spectrum of RhB dye. Because of bare overlap with emission, a very low PL was observed from this sample, shown by the solid magenta line in Fig. 3.11b.

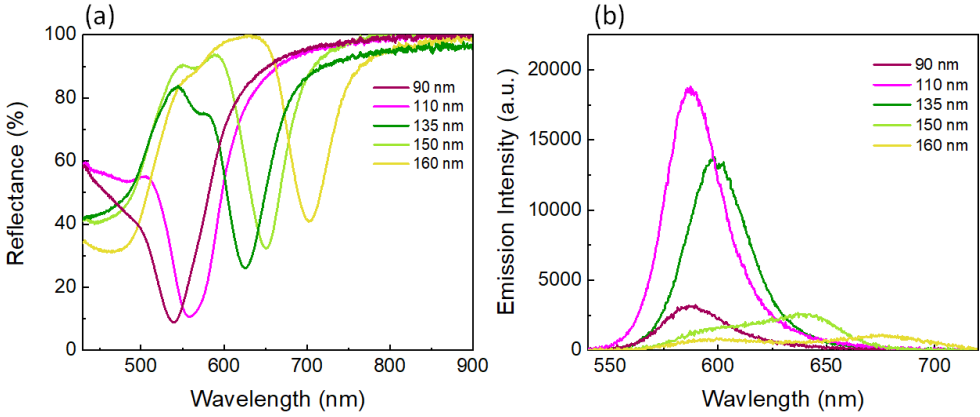


Figure 3.11 (a) Experimentally recorded reflection spectra for different thicknesses of the hydrogel. (b) The PL response of RhB incorporated in MIM cavity with different hydrogel thicknesses. [18]

Upon increasing the hydrogel thickness to 110 nm, the cavity resonance redshifts to 558 nm, displaying a significant overlap of cavity resonance with both the absorption and the emission spectra of an emitter. This simultaneous overlap opens the door to utilizing the contribution from the Purcell enhancement and the excitation rate enhancement to enhance the overall emission. The highest emission intensity was observed in the case of the MIM cavity with 110 nm hydrogel, as indicated by the solid pink line in Fig. 3.11b. Moreover, in the case of the MIM cavity with a dry hydrogel thickness of 135 nm, the cavity mode overlaps mainly with the emission, and there is a slight overlap with the tail of the absorption, which results in a decrease in emission intensity and further redshift. After additional increments in dry hydrogel's thickness to 150 nm and 160 nm, the cavity resonance shifted away from the absorption and emission spectra of RhB. It occupied lesser overlap with the tail of the dye's emission. As a result, more and more reduction in PL was observed with a small shoulder at about 650 nm. These observations conclude that the basic principle involved in the emission intensity change, in the case of a cavity that overlaps

only the emission of an emitter, is the Purcell enhancement. On the other hand, for the cavity resonance, which overlaps with both absorption and emission, the factors involved in emission intensity change are the Purcell enhancement and the excitation rate enhancement. As the Stokes shift for RhB is small (30 nm), it is difficult to completely isolate the contributions arising from the Purcell enhancement and the excitation rate enhancement. Therefore, the wavelength corresponding to the emission peak slightly offsets the cavity resonance wavelength.

3.2.4 Reversible and active emission tuning in air

In the last section, the passive tuning of emission was demonstrated. The next is real-time emission tuning via hydrogel-based MIM in response to ambient humidity. The humidity-based tuning allows active control of the overlapping region between cavity resonance and the emission and the absorption of RhB, which manifests as tunable emission. Fig. 3.11 brought to light that the MIM sample with 110 nm hydrogel thickness has the best overlap and is optimal for enhancing the emission intensity. Therefore, the MIM with a dry hydrogel thickness of 110 nm was selected to demonstrate the active tuning. Additionally, to perform relative humidity (RH) controlled reflectance and PL measurements, a customized experimental setup with Linkam Scientific LTS420-H stage and RH95 humidity controller, was utilized. Here also, the WITec microscope was used to measure reflectance spectra. The samples were illuminated with a broadband light source. In this measurement, a 2.5X air objective with a relatively long working distance was utilized to focus on the samples, which were embedded within the Linkam Scientific LTS420-H stage in the customized setup. The PL measurements were also performed in the humidity chamber, and a 532 nm laser source was used to excite the samples. The measurements were performed in a controlled environment at 3%, 30%, 60%, and 80% RH at a constant temperature. Furthermore, measurements were also conducted reversibly, i.e., from 80% back to 3% RH value, to obtain the reversibility of the PL response. Both forward and reverse cycles of reflectance, and PL measurement are depicted in Fig. 3.12a and b, respectively. The optical images captured at 3%, 30%, 60%, and 80% RH shows an evident change in color as shown in Fig. 3.12c. These distinct colors signify that with a change in humidity, hydrogel swells, and deswells, resulting in a modification in hydrogel thickness which changes the wavelength of a cavity resonance. The labeled

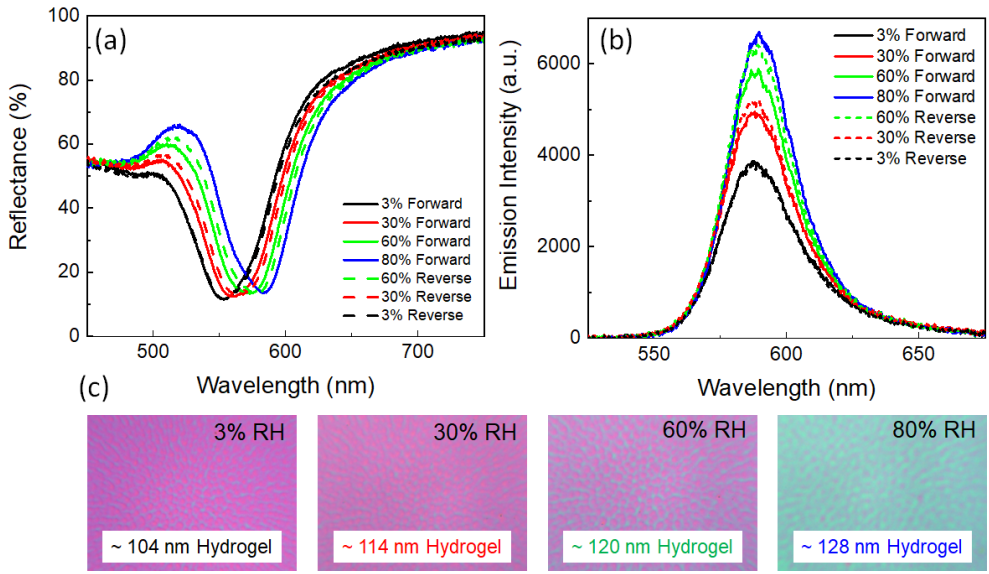


Figure 3.12 (a) Experimentally recorded reflection spectra of MIM cavity at different humidity values. The thickness of hydrogel in the dry state is 110 nm. The solid curve represents the forward (i.e., increase in humidity from 3% to 80%), and the line depicts the reverse cycle (i.e., decrease in humidity from 80% to 3%). (b) Steady-state emission spectra of a cavity at different humidities. (c) Optical images of MIM samples at various humidities. The corresponding thicknesses of hydrogel are marked in the optical images which were extracted from the simulation. [18]

hydrogel thicknesses at different humidity values were extracted from the simulation results. The change in hydrogel thickness was from 104 to 128 nm with an increase in humidity from 3 to 80%. As a result, the cavity resonance redshifted by 30 nm, from 548 to 588 nm, as shown in Fig. 3.12a. During this process, the cavity resonance overlaps better with the emitter's absorption and emission spectra. Hence, an almost 2-fold increase in the emission intensity was observed with a change in humidity from 3% to 80%, as shown in Fig. 3.12b. To verify the reversible nature of the humidity-induced emission tuning, RH was decreased from 80% to 3%. It is interesting to note that the forward cycle (3 hours) was a bit faster than the reverse cycle (3.5 hours) reason being the rates at which the hydrogel expels and absorbs water are different. It was observed that in the reverse cycle, the humidified sample (80% RH) started expelling the absorbed water gradually with a decrease in RH value, and the cavity resonance retains its original position, as shown in Fig. 3.12a (black, red, and green dashed line). The decrease in the hydrogel thickness during the reverse cycle

also allowed retrieval of the PL intensity, as shown by black, red, and green dashed lines in Fig. 3.12b. As a result of the swelling and deswelling properties of the hydrogel, it was possible to reversibly tune the optical response of the MIM cavity and, therefore, the PL intensity based on humidity changes. Subsequently, to check the

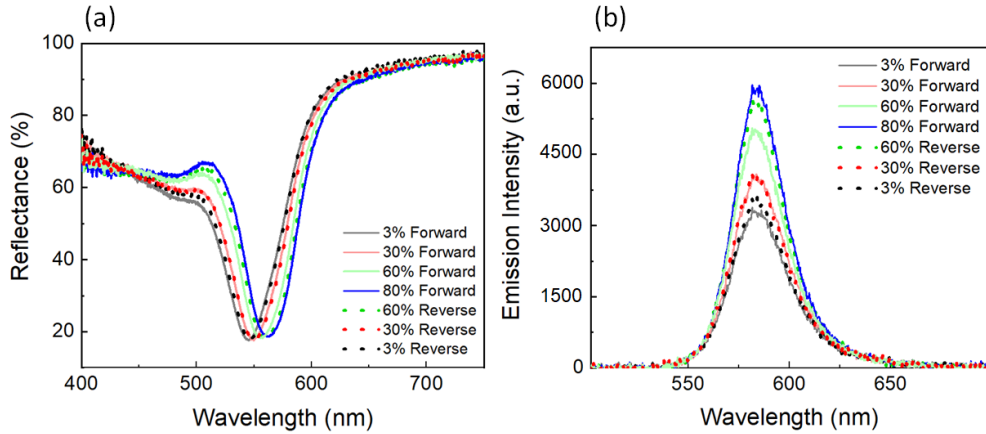


Figure 3.13 (a) Experimentally recorded reflection spectra of MIM cavity (with 110 nm hydrogel) at different humidities. (b) Steady-state PL of the dye at varying humidity values.

performance of our device after several humidity-controlled swelling/deswelling cycles, the same reflectance and PL measurements with the second swelling-deswelling cycle after 24 hours were performed on the same sample as that of Fig. 3.12. In the repeat measurement cycle, it was observed that both reflectance and PL results are almost reproducible (as shown in Fig. 3.13) and do not get worse after two cycles. Based on the results, it is inferred that even after several humidity-controlled forward/reverse (swelling/deswelling) cycles, emission intensity was preserved, and the device performance did not deteriorate.

From Fig. 3.12 and Fig. 3.13, it is observed that the dynamic tuning of PL occurs because of the change in the overlapping part of cavity resonance and dye's emission and absorption with varying RH values. To confirm that the increase in humidity does not directly affect the intrinsic properties of the dye in the hydrogel matrix, a 100 nm Hydrogel+dye (PNIPAm-BP-RhB copolymer) was coated on the glass substrate. The PL spectra of the fabricated sample were measured at different humidities as shown in Fig. 3.14 and observed that for the amount of dye (dye concentration) that was used, the PL does not change with humidity. Therefore, the intrinsic emission property of dye molecules was not changed in a humid environment, and a dy-

namic tuning in emission (as shown in Fig. 3.12b and Fig. 3.13b) is purely due to the significant overlap of the cavity resonance with the dye's absorption and emission.

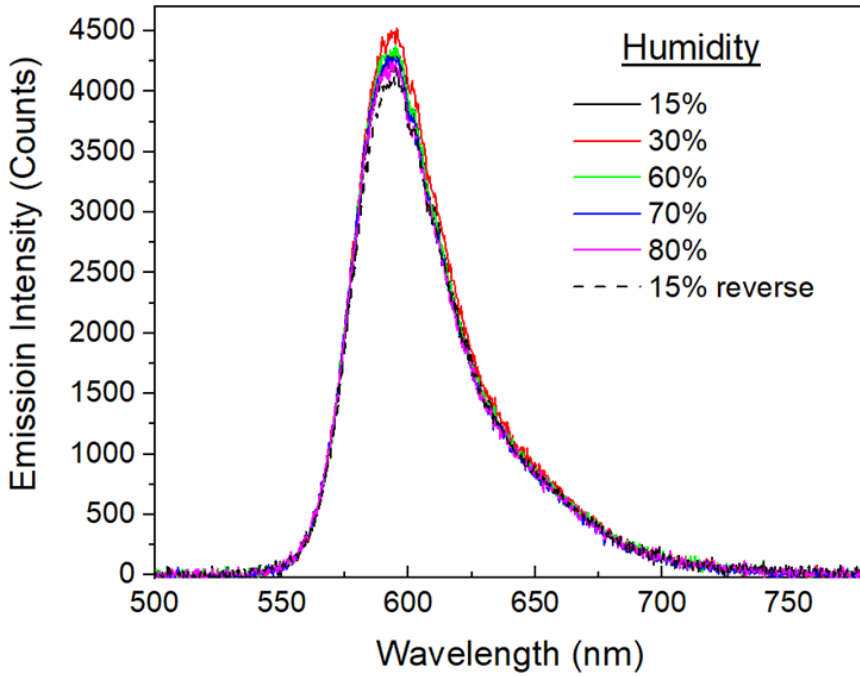


Figure 3.14 Steady-state PL spectra of RhB dye molecules bound with hydrogel at different humidities.

3.2.5 Active emission tuning in water

In the previous actively tunable system, the hydrogel thickness was controlled by a change in humidity. However, humidity-controlled thickness tuning does not allow large variations in the thickness. Therefore, to find the limits of hydrogel integrated MIM system, the sample was immersed in the deionized (DI) water for different time periods as 5, 10, and 20 minutes (wet state). The variation in hydrogel thickness achieved in the submerged case was much more significant than in the air humidity-controlled case. As a result, large spectral shifts in MIM cavity resonance were observed as compared to the humidity-based control. The sample (MIM cavity with a dry hydrogel thickness of 110 nm) was submerged for 5, 10, and 20 min in DI water, and the change in the cavity resonance, as well as the changes in the PL response, was observed.

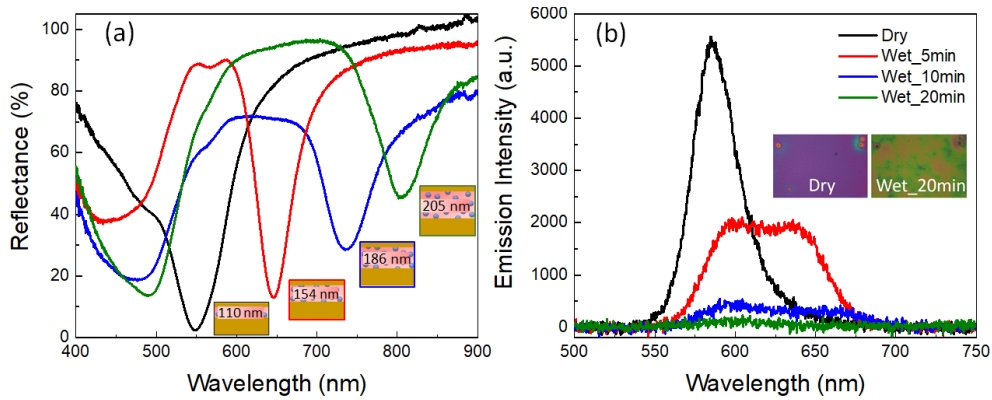


Figure 3.15 (a) Experimentally recorded reflection spectra of MIM cavity completely immersed in DI water for different time duration. The inset shows the corresponding hydrogel thickness calculated using simulation. (b) PL spectra of dye incorporated with MIM for dry case and when completely immersed in water for different duration. The inset shows the optical image of sample for dry case and after immersing into water for 20 minutes. [18]

Figs. 3.15a and b show the measured reflectance spectra and PL in three submerged cases, respectively. The inset of Fig. 3.15b shows the optical images of the sample in the dry case (with a thinner hydrogel layer) and the wet case (after hydrogel swelling). The dry case was compared with the wet case to evaluate the tuning range. The dry hydrogel (at ambient conditions) thickness was 110 nm, and after the sample was immersed in DI water for 20 min, the spectral shift of 255 nm, which is from 550 to 805 nm (from black to solid green line), was observed. Since the cavity resonance shifted to a higher wavelength, its overlap with the absorption and emission spectra of dye was reduced. As a consequence, a decrease in the emission intensity was observed as depicted in Fig. 3.15b. Subsequently, for 20 minutes immersion case, i.e., for the cavity with swollen hydrogel thickness of 205 nm, the MIM cavity resonance does not overlap with the emission of dye at all, which resulted in negligible emission. As the increase in hydrogel thickness illustrates the absorption of water in the hydrogel, therefore, the subsequent investigation is to find the influence of the refractive index (R.I.) of water on the effective index of the hydrogel-water system. since water has a smaller refractive index (1.33) as compared to hydrogel (1.503), one would expect that the effective refractive index of the hydrogel would decrease with the increasing humidity or water content, particularly for the case when the sample was immersed in DI water. Additional calculations were performed by using the below formula.

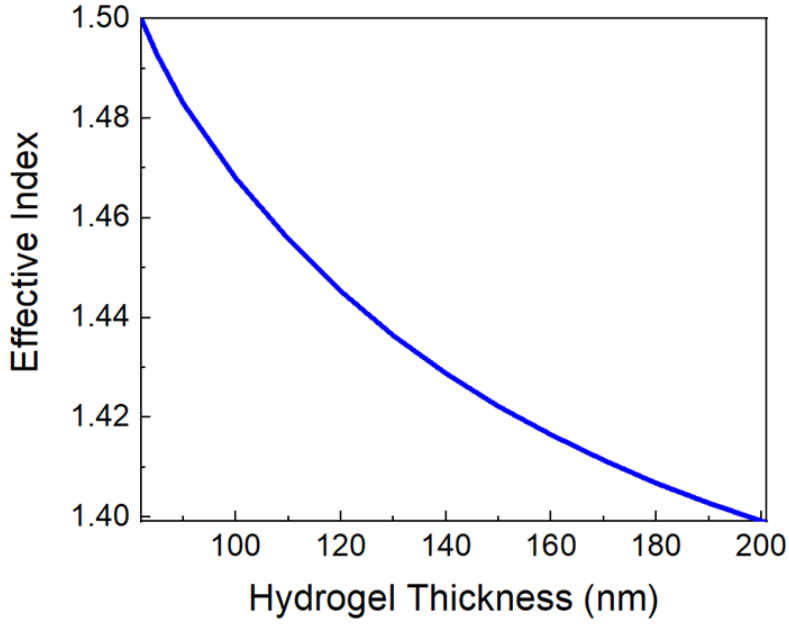


Figure 3.16 Effective refractive index vs thickness of the hydrogel-water complex.

$$n_{eff} = \frac{n_{hydrogel}H_{hydrogel} + n_{water}H_{water}}{H_{hydrogel} + H_{water}}, \quad (3.2)$$

where,

n_{eff} - effective R.I.,

$n_{hydrogel}$ - R.I. of hydrogel,

n_{water} - R.I. of water,

$H_{hydrogel}$ - the hydrogel's thickness in the dry state and

H_{water} - an increase in thickness due to water content.

Fig. 3.16 shows a slight change of the effective index to approximately 1.4 at 205 nm thickness. Fig. 3.17a shows the simulated reflection spectra by varying hydrogel thickness and keeping the refractive index of the hydrogel at 1.503. On the other hand, in Fig. 3.17b, both the thickness and the effective refractive index of hydrogel were varied, and the indices at each thickness were derived from Fig. 3.16. The simulation results of Figs. 3.17a and b clearly illustrate a slight change in reflection spectra upon comparing them. Conclusively, the difference in effective refractive index is relatively small, and its effect on the resonance shift is reasonably minimal.

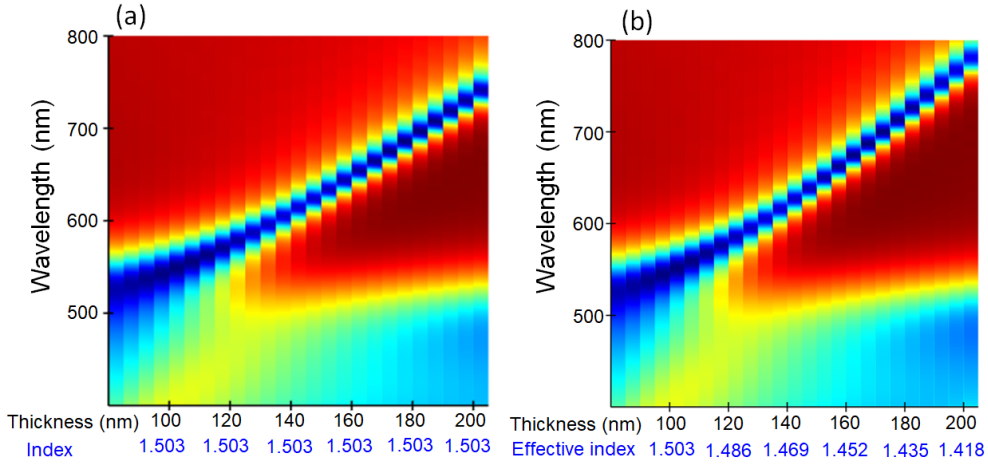


Figure 3.17 The simulated reflection spectra of the MIM cavity with varying insulator (hydrogel) thickness in two cases: (a) by keeping the hydrogel's refractive index constant at 1.503. (b) by considering the effective index of the hydrogel-water complex.

3.3 Conclusion

This work is the first demonstration of reversible active tuning of emission intensity by utilizing a controlled-humidity chamber. The only limitation of this work is swelling and deswelling times of hydrogel are more than three hours which might affect the potential application. On the other hand, the water-immersed case is faster and has considerable resonance spectral tunability (up to 250 nm) using the hydrogel. It mitigated the complex fabrication challenges of designing on-demand tunability as the MIM cavity was utilized as a photonic platform that offers electric field confinement to a large area, thus highly suitable for enhancing the PL emission. Additionally, an active tunability of cavity resonance aid an additional degree of freedom to control the PL emission.

4 ELECTRICALLY TUNABLE COUPLING OF EPSILON-NEAR-ZERO AND PLASMONIC MODES

Light matter interactions are often characterized by the coupling strength between the resonances. Depending on the coupling strength, the coupling regime can be categorized into weak, strong, and ultra-strong coupling regimes. The achievement of weak and strong coupling has led to increased control of the optical properties of resonators or emitters, which in turn enabled several optoelectronic applications. Interestingly, the fundamental properties of matter, such as emission rate, can also be altered by making it strongly coupled to light. Furthermore, from an application point of view, the strong coupling is viable as it reduces the loss channels of the photonic system by periodically exchanging the energy between the coupled systems. Therefore, it is imperative to achieve on-demand control of the coupling process in photonics.

In photonic systems, metallic resonators are widely employed to realize strong coupling. It is because metallic resonators provide strong confinement of light into subwavelength volume. The presence of strong coupling manifests as spectral splitting in the transmission/reflection spectra, where the separation between the split modes is called Rabi frequency. It quantifies the periodicity of the energy exchange between the modes. Particularly, in the strong coupling, Rabi frequencies are large enough that the energy exchanges among the hybrid modes before its loss. However, one of the major limitations associated with metallic structures is their low quality (Q) factor. Q-factor quantifies the quality of the resonance strength, thus, in turn, important for realizing strong coupling. To circumvent this limitation, the ENZ material that offers deep subwavelength field confinement due to the excitation of ENZ modes was utilized. The ENZ mode appears at wavelength or frequency where

the film's real dielectric permittivity vanishes. Leveraging the strong field confinement at ENZ mode, numerous studies have been demonstrated of nonlinear optical process [102, 103], frequency conversion [104], and electro-optical effects [17, 22]. Interestingly, integrating a metallic resonator with ENZ materials has shown a strong coupling effect [105]. The underlying principle to achieve strong coupling in such a system is to design the metallic resonators with resonance frequency within the ENZ region of ENZ materials. Therefore, it is obvious to tune the coupling strength in such systems by changing the geometrical parameters of the metallic resonators. Although, the passive tuning of the coupling strength has some merits but puts a constraint on practical applications. In this regard, achieving an active way to tune the coupling strength is exciting and offers a viable route for disruptive application as well as fundamental studies.

In this dissertation, a novel gating scheme based on ionic liquid was developed to enable active tunability. Our tunable, strongly coupled system comprises a thin ENZ material (Indium Tin Oxide (ITO)) and gold nanorods as plasmonic resonators. By changing the bias voltage, a significant tuning of the coupled resonance was observed. Various applications can benefit from this tuning mechanism that allows for advanced control and tunability of strongly coupled systems.

4.1 ENZ mode excited in the ITO layer

In this dissertation, ITO thin film was employed as ENZ material, which supports ENZ modes [106, 107] because of its remarkable properties like lower optical losses, large electrical conductivity, and tunable permittivity [108, 109, 110]. The ENZ modes in ITO are long-range surface plasmon polaritons whose dispersion becomes flat at the ENZ point for ultra-thin ENZ film. Interestingly, these ENZ modes exhibit a large density of states and can homogeneously confine the EM radiation within the ENZ thin film. As the ENZ mode lies within the light line (i.e. right of the light line), due to this, the excitation of ENZ mode directly from the incident light propagating in the air is difficult. While adding plasmonic structures such as nanoantenna on the top of ITO thin film provides the necessary momentum to excite the ENZ modes.

The complex permittivity of 40 nm thin ITO film was extracted using ellipsometry measurement as shown in Fig. 4.1a. The dispersion relation for ITO film em-

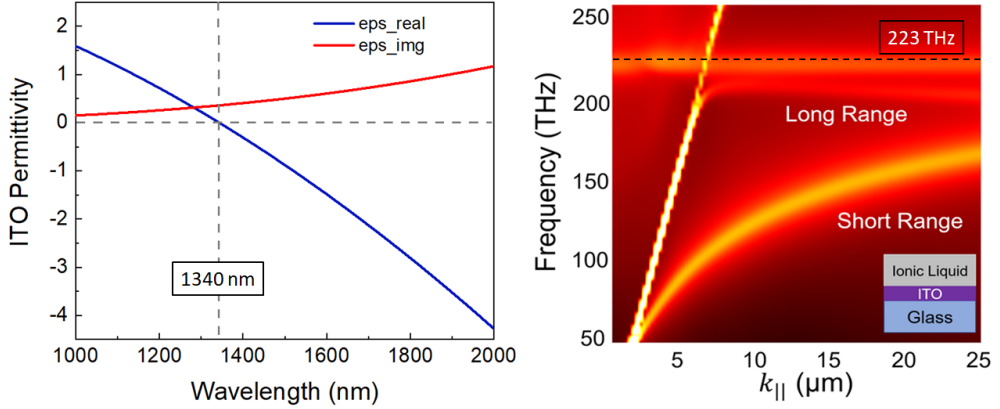


Figure 4.1 (a) Complex permittivity of a 40 nm thin ITO film measured using ellipsometry. (b) Dispersion relation of the ionic liquid - ENZ material - glass three-layered system.

bedded in ionic liquid (inset Fig. 4.1b) was calculated using the FDTD simulation. In the simulation, the Bloch boundary conditions were used. The dipoles with different phases and orientations were placed in the simulation region. The dispersion relation plot (Fig. 4.1b) was obtained by sweeping different transverse wave vector $k_{||}$ values, and by calculating the corresponding eigenfrequencies. To constrict the modes which were not supported by the designed structure, the simulation time was adequately long. The long-range and short-range surface plasmon modes of ITO thin film in the ionic liquid background are indicated in Fig. 4.1b. The long-range mode's dispersion was closely flat for a large range of $k_{||}$ near 225 THz frequency which is persistent with the ellipsometry result (Fig. 4.1a), which indicates 1340 nm as ENZ wavelength ($\approx 223 THz$). Hence, the long-range surface plasmon is called the ENZ mode [110] as introduced in Chapter 2. To enable high EM fields in the ENZ thin film and to generate the LSP mode, the gold nanorods were utilized in this work.

4.2 LSP mode of nanoantenna and its fabrication

The zero permittivity ($\epsilon \approx 0$) region of ITO from 1200 to 1500 nm is highlighted with a gray color in Fig. 4.2a. The plasmonic nanostructures can confine the incident electromagnetic field at a deep subwavelength scale due to the excitation of LSP, which leads to a remarkable enhancement of the local field. Therefore, Au nanorods were utilized to confine the EM field inside the ENZ film and generate the LSP mode.

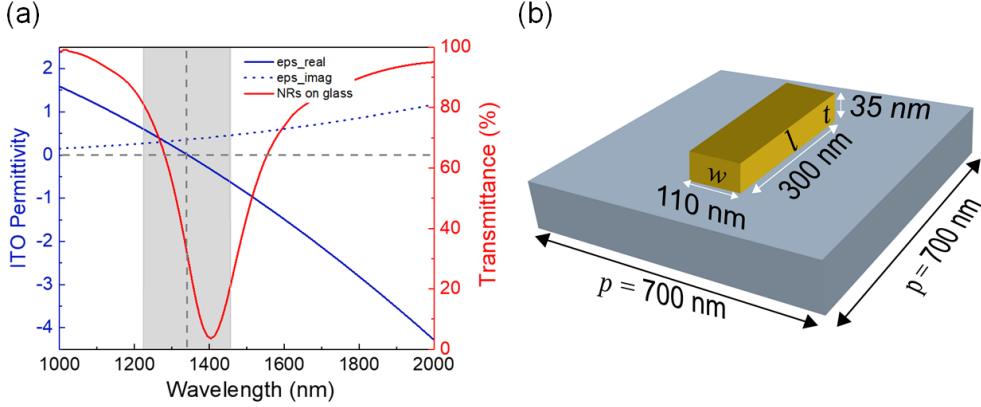


Figure 4.2 (a) 40 nm thin ITO film's permittivity result, where real and imaginary parts are depicted by the solid blue line and dotted blue line. The ENZ region is highlighted with grey color. The simulated transmittance spectrum of the optimized nanorods placed on a glass substrate is shown by the solid red line. [69] (b) diagrammatic representation of unit cell consisting of a gold nanorod on a glass substrate.

To optimize the Au nanorod's dimension such that their plasmonic resonance falls in the ENZ region of the ITO film, the numerical simulations were performed using FDTD. The linearly polarized plane wave source of wavelengths 1000–2000 nm was utilized to excite the nanorod with polarization along the nanorod's long edge. The gold (Au) was modeled by using Johnson and Christy material data [111] from the in-build material library of Lumerical. In the optimization process, the background refractive index value used was 1.41 to emulate ionic liquid ambience. As will be shown, the ionic liquid is needed for tunability. The simulated transmission plot for the optimized nanorod on a glass substrate is shown in Fig. 4.2a (solid red line). The dimensions of the optimized nanorod antenna were, length (l) = 300 nm, width (w) = 110 nm, and thickness (t) = 35 nm as marked in the schematic shown in Fig. 4.2b. The periodicity (p) was kept at 700 nm to maximize the density of the nanorod while avoiding the cross-talks between them.

The studied structure is based on a $100 \times 100 \mu m^2$ pattern of Au nanorods fabricated on top of a bare glass substrate and on 40 nm thin ITO coated on a 1.1 mm thick glass substrate. The 40 nm thin ITO layer on of glass substrate was purchased from 'Prazisions Glas und Optik'. A layer of resist poly(methyl methacrylate) (PMMA) 950K A2 was spin-coated on top of the substrate and then evaporated anisole, baked

at 180°C for 90 Sec. The array of Au nanorods was patterned onto the resist using an EBL technique, and the area dose used was $300\mu C/cm^2$. The sample exposed with an electron beam was developed for 60 Sec in metylisobutylketon:Isopropyl alcohol (MIBK:IPA) solution (1:3), and IPA was used as a stopper. A 1/35 nm layer of Ti/Au was deposited on developed samples using an electron beam metal evaporator. After lift-off in S1165 remover at 80°C, the sample was then cleaned using deionized water.

4.3 Strong coupling of ENZ and LSP modes

Once the ENZ and LSP modes were identified, the strong coupling of these modes was investigated by bringing them to the same platform. The ENZ-integrated plasmonic hybrid system's transmission spectra with (solid red line) and without ionic liquid (solid black line) were experimentally recorded, as shown in Fig. 4.3a. The presence of the ionic liquid redshifts the overall spectra due to an increase in background refractive index ($n_{air} = 1$ to $n_{ionicliquid} \approx 1.41$). In the optimization process of the plasmonic antenna, the background refractive index was included as 1.41.

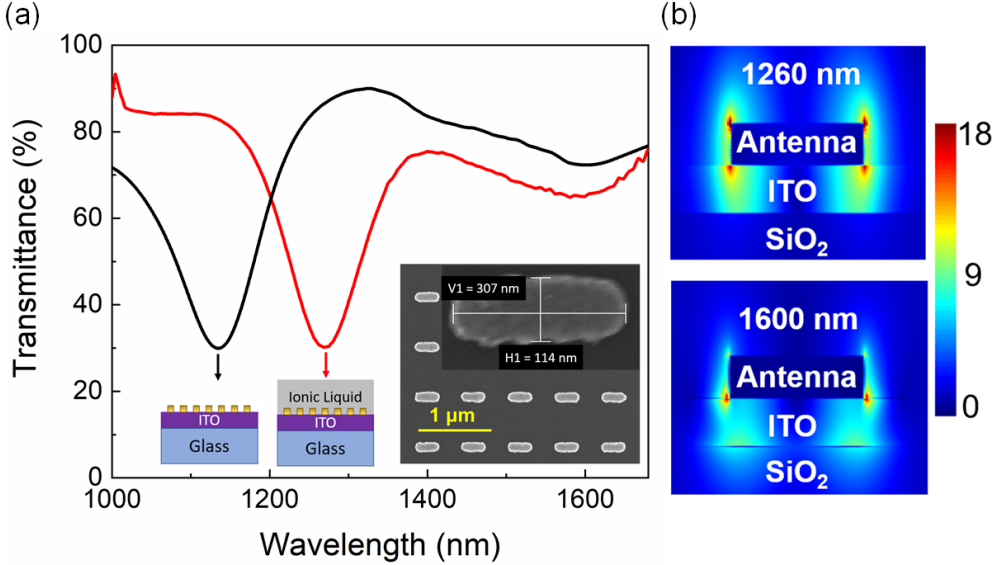


Figure 4.3 (a) Measured transmittance spectra of plasmonic antenna array on ITO substrate and the inset depicts SEM image of the Au nanorods. (b) Simulated electric field (E_x) plot of antenna array on ITO substrate at lower polariton (1260 nm) and upper polariton (1600 nm) [69]

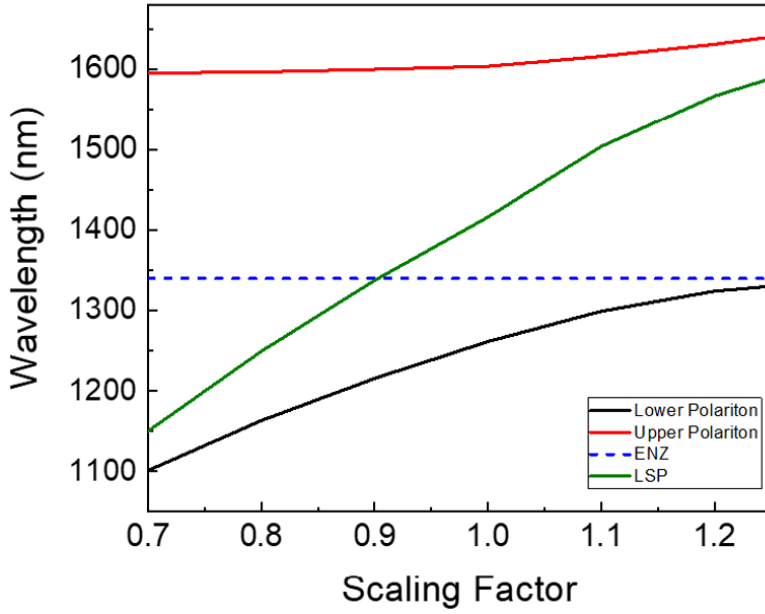


Figure 4.4 Simulation result for strong coupling between nanorod and ENZ mode of ITO. The dimensions of the nanorod vary by a common factor ranging from 0.7 to 1.2. The observed anti-crossing behavior implies that the ITO + Nanorod system exhibits strong coupling.

As a result, its resonance position was red-shifted to the ENZ region. Therefore, in Fig. 4.3a both upper and lower polaritons are clearly visible, which shows that in the presence of ionic liquid, the system exhibits strong coupling that manifests as apparent spectral splitting (solid red line). In contrast, the system without ionic liquid was weakly coupled. The inset of Fig. 4.3a represents the scanning electron microscope (SEM) image of the plasmonic structures (top view), showing the geometry of the gold antennas (square lattice Au nanorods). Note that fabricated nanoantennas were slightly different from the simulated ones due to the fabrication imperfections, which resulted in antenna edges being rounded off. The electric field confinement in the plasmonic structure and ENZ layer of the strongly coupled system shows the hybrid characteristics' features. The antennas placed on the ITO film allow the electric field to be concentrated inside the ITO layer resulting in the enhancement of the field intensity at polaritonic wavelengths. Fig. 4.3b shows the electric field distribution of the ENZ-integrated system, calculated at lower polariton (1260 nm) and upper polariton (1600 nm) that display a mixture of localized plasmons and ENZ mode confinement.

One important parameter that defines the strong coupling is anti-crossing behavior. Therefore, an additional simulation was performed to strengthen the claim of strong coupling and presented the results in Fig. 4.4. In the simulation, the dimension of the nanorod was varied by a common scaling factor ($l = 300 \text{ nm} \times \text{scaling factor}$, $w = 110 \text{ nm} \times \text{scaling factor}$) that varied between 0.7 to 1.2. In Fig. 4.4, the anti-crossing behavior was clearly observed, which is a signature of strong coupling. It is important to note that a similar strong coupling behavior was also reported by Campione *et al.* [112], where the authors utilized a dog-bone-shaped nano-resonator and ITO as ENZ material.

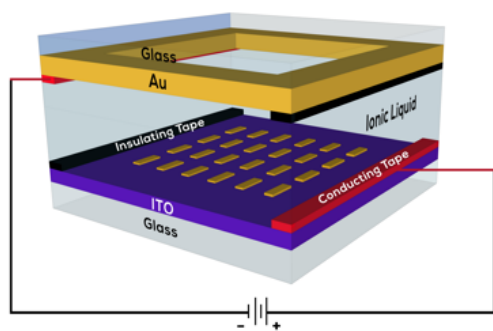
4.4 Design of dynamically tunable system

4.4.1 Gating system

To achieve an active tunability of ENZ-LSP coupling, the most important task was to design a gating system. In this thesis, firstly, three different cases have been analysed as explained below, and then designed the most efficient gating system and used for experiments to show the dynamic tuning of ENZ-LSP coupled mode. The schematic of the 3 different architectures to achieve the electrical gating in transmission mode is shown in Fig. 4.5.

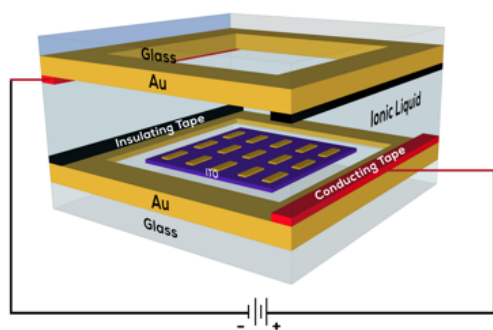
Case 1: In this assembly, the copper wire which was used for biasing was directly connected to the ITO layer. Due to the ITO layer's resistance, the contact resistance was high, and in such case, voltage loss occurred. Therefore, it was necessary to apply a high voltage to operate such a gating configuration effectively. Additionally, there was a potential drop upon moving along the ITO layer i.e., moving away from a voltage application point in ITO makes the potential gradient drop, thereby weakening the electric field.

Case 2: In this assembly, the ITO was etched using RIE (Reactive ion etching) from the periphery and only remains in the center, as shown in case 2. As there was no contact between the Au electrode and ITO, therefore the charge accumulation on the ITO surface was totally dependent upon carriers induced in ionic liquid through gating because the charge transfer medium in this case was only ionic liquid. It was necessary to connect ITO to an electrode to allow electrons or holes to flow in either direction upon polarizing the ITO surface using an ionic liquid; this was because



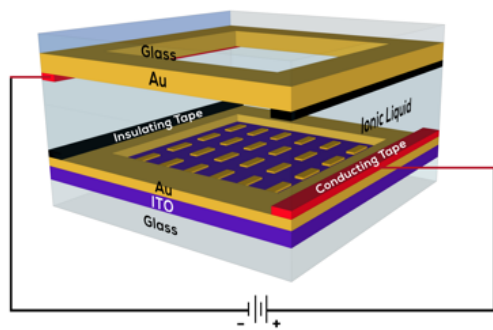
Case 1

- Directly biased ITO
- High contact resistance
- High voltage needed



Case 2

- No contact between Au electrode and ITO
- Floating Potential



Case 3

- Au electrode connected to ITO surface
- Uniform Biasing

Figure 4.5 Optimization of gating architecture: an artistic illustration of the three different cases to achieve the electrical gating in transmission mode.

additional charge carriers needed to flow from the source depending on the change in potential along the ITO surface. However, if there is no connection between the

ITO layer and the electrode, then the potential will remain floating potential which will not contribute significantly to charge density change on ITO surface. Hence, this case was not suitable for electrically tunable strongly coupled ENZ-LSP gated system.

Case 3: Here, the Au electrode was on top of the ITO; therefore, the biasing was uniform along the gold electrode, every point on the surface was at the same potential, and there was a very less potential loss. The electrodes were designed in such a way that, except for the small centre window in the upper plate, the rest of the part was gold in order to have uniform potential distribution after biasing.

As case 3 was the most efficient way to have uniform biasing, a gating scheme was designed using the approach shown in case 3. To achieve the dynamic tunability of ENZ-LSP coupling, a novel electrical gating scheme that allows transmission measurements was built to provide an extra dimension of performance. The designed gating is versatile in nature and is compatible with operating in both the transmission and reflection modes. The schematic of the designed architecture to achieve the electrical gating in transmission mode is shown in case 3 of Fig. 4.5. The gating assembly consists of two plates: the bottom plate includes the substrate with 40 nm ITO thin film followed by a square array of gold nanorods as shown in the inset of Fig. 4.3a, and the top plate was a bare glass. On both ITO and glass substrates, a gold periphery window was created to connect copper wires with good ohmic contact. To avoid a short circuit, these two substrates were separated from each other by insulating tapes. The ionic liquid was sandwiched between these two plates, which serve as media to accumulate ions at ITO and ionic liquid interface upon electrical biasing.

4.4.2 Hall measurement

The Hall measurement was performed on the nanorod-ITO gated system with developed biasing architecture. Fig. 4.6a shows the artistic illustration of our design with Hall measurements compatible biasing scheme. The assembly consists of top and bottom plates to facilitate the biasing and 4 metal contact pads for Hall measurement. Fig. 4.6b shows the measured carrier concentration for various voltages using the Hall measurement system. It is evident that by increasing the voltage, the carrier concentration changes due to the polarized ionic liquid. With changes in voltage, the

density of charge carriers does not change in bulk ITO, but only at the interface between ionic liquid and ITO surface. This enhanced carrier density at ITO surface changes the ITO permittivity, allowing us to tune the strong coupling between plasmonic nanorods and the ENZ layer. Thus, changing the bias voltage offers electrical tunability of ENZ-LSP hybrid modes' coupling strength.

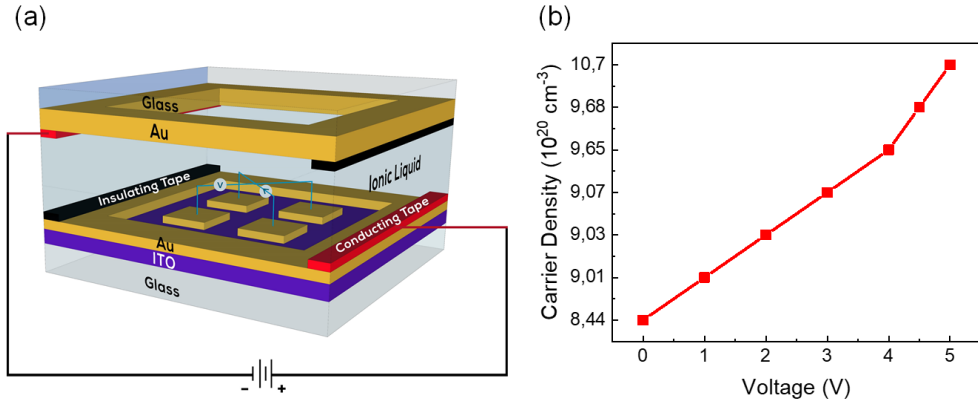


Figure 4.6 (a) diagrammatic representation of Hall measurement compatible gating system. (b) Hall measurement result, the carrier density in ITO at varying voltage values.

4.5 Gate-tunable coupling of ENZ-LSP mode

4.5.1 Active tuning of strongly coupled ENZ-LSP modes

The active tuning of strongly coupled ENZ-LSP modes was achieved by electrical biasing. In previous studies, to achieve tunability, the gating schemes require the metallic plate to be present at the backside of devices which severely limits the mode of operation to be only in reflection [22, 113, 114]. In contrast, our designed gating is highly versatile.

The change in the bias voltage offers electrical tunability of ENZ-LSP hybrid modes' coupling strength that manifests as a change in the spectral splitting. The experimentally acquired transmission spectra (Fig. 4.7a) for various bias voltages evidently show the splitting, and the zoomed spectra near the lower polariton wavelength are shown in Fig. 4.7b. Further, to emulate the experimental spectra (particularly the no-bias condition as shown in the solid black line in Fig. 4.7), the FDTD

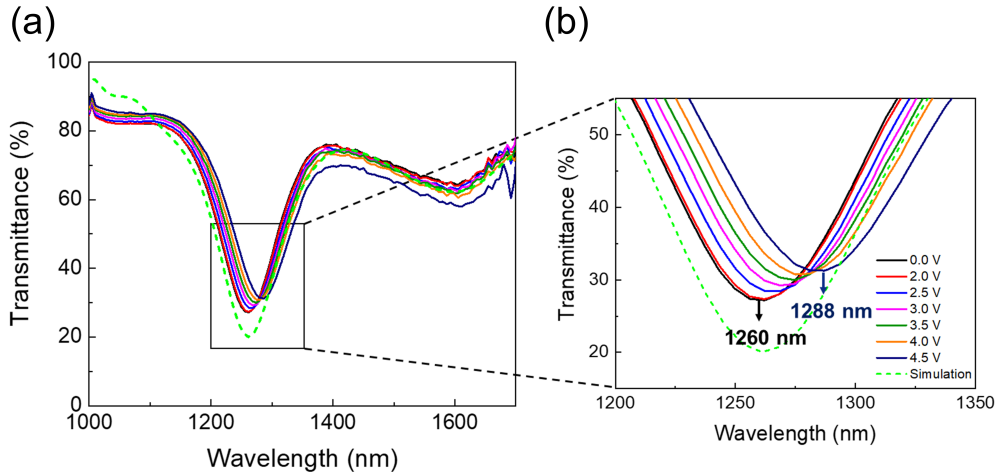


Figure 4.7 (a) Experimentally recorded spectra at various bias voltages. (b) Zoomed portion of transmission spectra near lower polariton wavelength.

numerical simulation was performed. The experimentally recorded permittivity of ITO was fed into the simulation, while the optical property of gold was used from the in-built material library of Lumerical. The green dashed line in Fig. 4.7 shows the simulated transmission spectra in no bias case of nanorod/ITO integrated hybrid system, keeping the background refractive as 1.41 to emulate the ionic liquid background. The simulated result (green dashed line) shows a good agreement with experimentally recorded spectra in no bias (0 V) case (solid black line).

For clarity, only the lower polariton is shown in Fig. 4.8, and the individual spectrum for different voltages are offset vertically. By increasing the bias voltage from 0 to 4.5 V, the lower polariton shifts from 1260 to 1288 nm, while there is a subtle change in the upper polariton as shown in Fig. 4.7. As the electric field confinement at the lower polariton (as shown in Fig. 4.3b) is more intense than the upper polariton, the lower polariton shows better tuning with respect to the upper polariton. Additionally, the change in the permittivity with different external bias voltages was more effective closer to the ENZ wavelength, where the lower polariton was observed. Since the splitting between the upper and lower polariton is proportional to the coupling strength, [115] change in the lower polariton's wavelength represents the change in the coupling strength of the strongly coupled system. Further, this coupling's tunability was verified using different nanorod dimensions, as shown in Fig. 4.9. The nanorods' size was considered so that the plasmon resonance still

resides inside the ENZ region (gray shaded region of Fig. 4.2a), which ensures the system remains in the strong coupling regime. The achieved tunability lies under the occurred modification in the permittivity of the ITO film as a response to the applied DC voltage. Under the presence of the electrical bias, the ions in an ionic liquid get polarized and accumulate at both the top and bottom interfaces. The increase in the voltage results in an increment of charge concentration at the interface of ITO and ionic liquid. These assembled ions at the interface induce charge increment that, in turn, changes the permittivity of the ITO. By increasing the bias voltage, the density of the ions increases and saturates after a threshold voltage which was 4.5 V in our case.

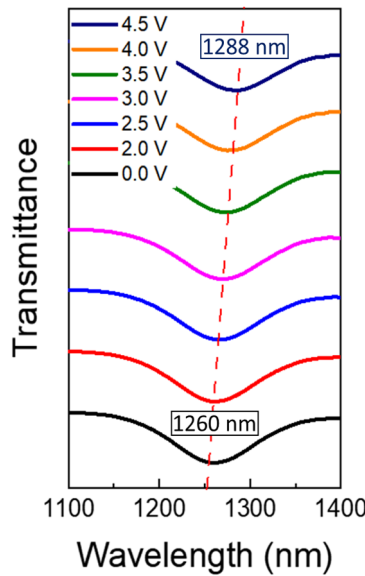


Figure 4.8 Measured transmission spectra at different gating voltages (individual spectra near lower polariton at different voltages are vertically offset).

To illustrate the consistency of this trend, the same experiment was repeated with different dimensions of the nanorod. Fig. 4.9a shows simulation results of resonance of different sized nanorods on a glass substrate, where the dimensions ($w \times l$) of nanorod 1, 2, and 3 were in nanometers 100×290 , 110×290 and 110×305 respectively, while the periodicity was kept identical as 700 nm for all three and the background index was 1.41 (ionic liquid). The dimensions of nanorods were selected in such a manner that their resonance still resides inside the ENZ region to make sure that the system is still in the strong coupling regime. The transmission

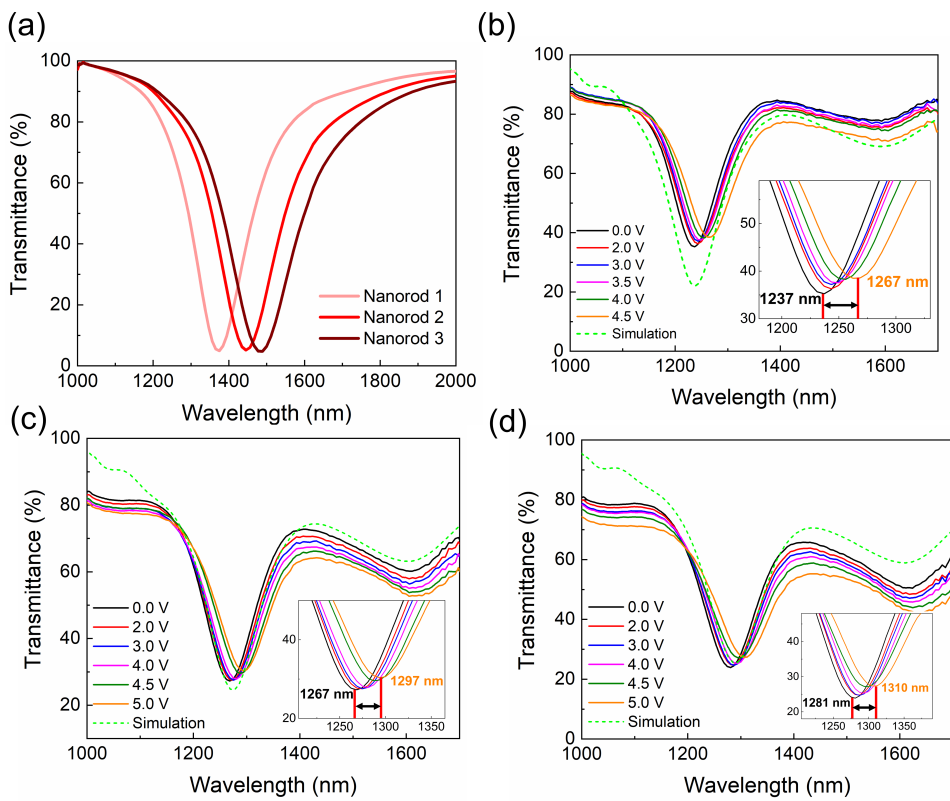


Figure 4.9 (a) Simulated transmission spectra of nanorods with various dimensions named as NR1, NR2, NR3. (b), (c) and (d) Experimentally recorded electrical tuning of transmission spectra of nanorod-ITO integrated systems corresponding to NR1, NR2, and NR3, respectively.

spectra corresponding to nanorod 1, 2, and 3 and ITO integrated systems are shown in Fig. 4.9b, c, and d, respectively. The spectral splitting in the transmission spectra for all three nanorods ensures strong coupling, and by applying the electrical bias, the tunability of the lower polaritons was consistently observed. Analogous to the main sample, ≈ 30 nm spectral shift in the lower polariton was observed for these nanorods, as well.

4.5.2 Reversible behavior of designed gated system

The I-V characteristics were recorded, where the voltage was applied to ITO as shown in the gated device (Fig. 4.10a). As a result, in some time intervals, ions in an ionic

liquid, get polarized and stabilized, then the corresponding current was measured, and the hysteresis behavior was observed as shown in Fig. 4.10b. Notably, this hysteresis behavior arose due to the difference in time taken by the ions of ionic liquid to return to the initial stage after removal of bias voltage i.e., within 10 min the ions did not return to their initial stage after removal of the bias voltage. This is a reversible process, but the time taken by the ions to get polarized and to relax back is different.

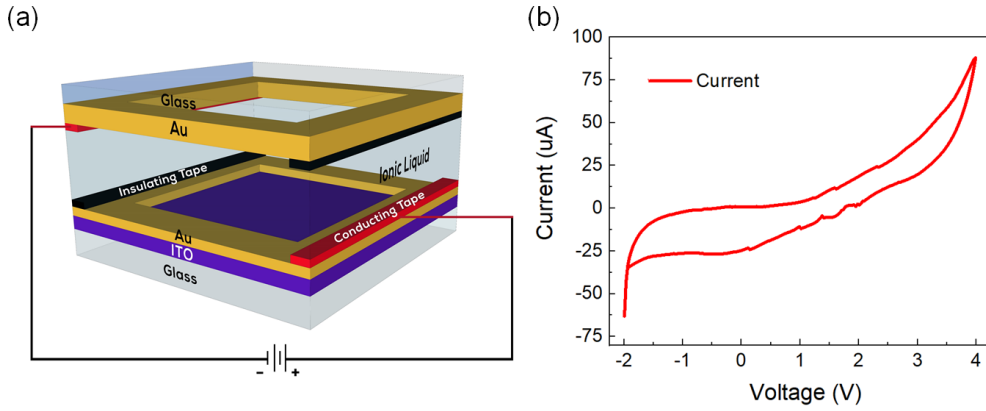


Figure 4.10 (a) The schematic of ITO gated system. (b) I-V characteristics of the device.

While recording transmittance by varying voltage, the transmittance peak changes over a certain gating time, and it was observed that for the designed gating configuration, in approximately 8 to 10 min, transmittance peak redshifts to a particular wavelength and stabilizes there until the gating voltage was changed to the next higher value. (This indicates that 10 min was the time taken by the gated system for most of the ions in an ionic liquid to get polarized for that specific external bias voltage). Also, the transmission spectra were recorded on two different days, as shown in Fig. 4.11. On day 1, the assembly (ITO + Nanorod + Ionic liquid) was biased by changing the voltage up to 4.5 V and kept the system as it was, and again recorded the spectra on day 2, the Fig. 4.11 shows that nearly identical spectra were retrieved, which confirms the repeatable and reversible nature of the system.

4.5.3 Effect of negative voltage

The magnitude of ω_p is determined by the carrier density as

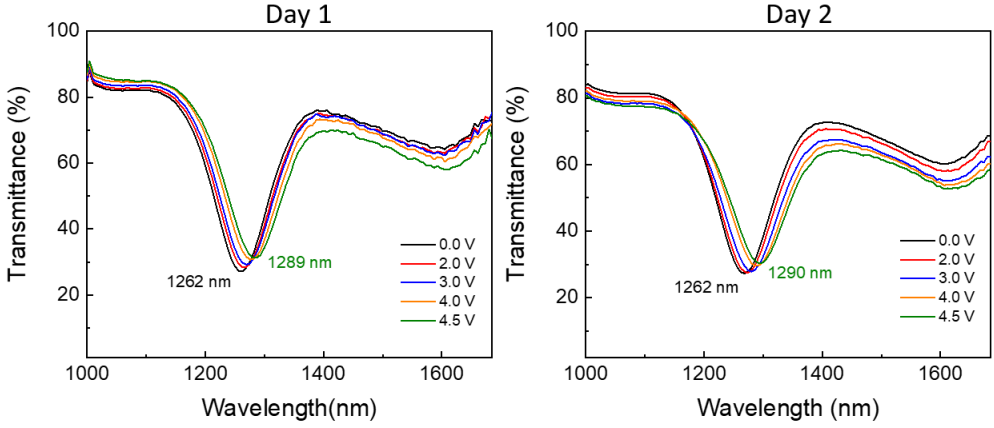


Figure 4.11 Transmission spectra recorded at different days, which exhibits nearly identical behavior which proves the reversibility of the system.

$$\omega_p^2 = \frac{ne^2}{m_e^* \varepsilon_0}, \quad (4.1)$$

where ω_p is plasma frequency, n is the electron density, e the electron charge (elementary charge = $1.60217662 \times 10^{-19}$ coulombs), ε_0 the free-space permittivity (8.85×10^{-12} F/m), m_e^* denotes the effective mass of the electrons. In the ITO, $m_e^* \approx 0.45 m_e$, where m_e is the electron mass in free space ($9.10938356 \times 10^{-31}$ kilograms).

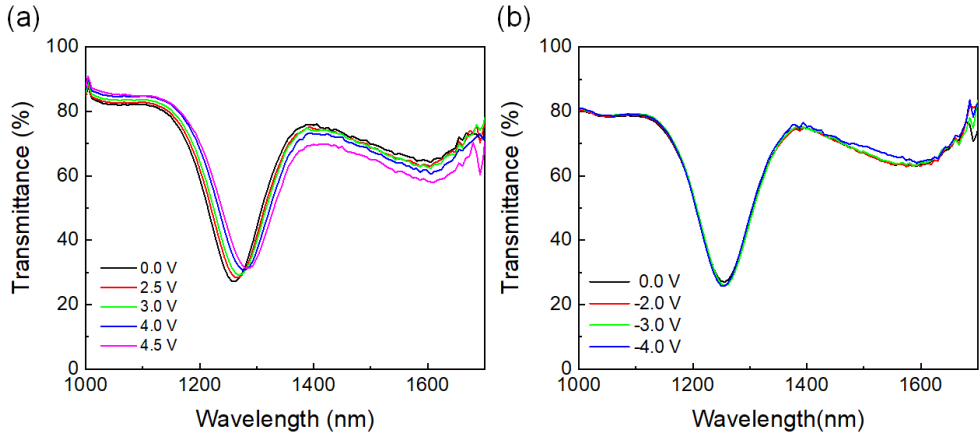


Figure 4.12 Experimentally recorded electrical tuning of transmission spectra of nanorod-ITO integrated systems (a) under positive bias, (b) under negative bias.

An applied positive voltage to the ITO layer attracts free electrons from the ionic

liquid and positive charges in ITO to the ITO surface. Consequently, ITO lacks free carriers, resulting in depletion. In depletion mode, there were fewer free charge carriers (n); thus, ω_p was smaller (Eq. (4.1)), and therefore ENZ wavelength shifted to a higher wavelength. Thus, as positive voltage increases, the red-shifting is observed in the coupled spectrum as shown in Fig. 4.12a. A negative bias toward ITO, on the other hand, causes the accumulation of free carriers in the ITO. In the accumulation mode of the material, there were more free carriers. When the ITO was in accumulation mode, n was more, so ω_p was greater. Therefore, ENZ wavelength shifts to a lower wavelength in the negative bias case, which results in a blue shift in spectra. However, in the negated gated assembly case, when the voltage was changed from 0 to -4V, all the ions accumulated, and a slight blueshift was observed, as shown in Fig. 4.12b. Although the shift can be more remarkable upon increasing the voltage, it was not possible to apply a higher voltage to the designed gated assembly to ensure its safe functioning.

4.5.4 Simulation results: tunable ENZ-LSP coupling

To emulate the effect of biasing, the numerical simulation was performed by varying the carrier concentration of ITO because changing the carrier density of ITO was nothing but changing the bias voltage in the experiment.

In the simulation, the ITO was modeled using the Drude model:

$$\varepsilon(\omega) = \varepsilon_{\infty} - \frac{\omega_p^2}{(\omega^2 + i\gamma\omega)}, \quad (4.2)$$

where ω_p and γ are the plasma and collision frequencies, respectively. Increasing the bias voltage across the ITO changes the carrier density, which in turn changes the plasma frequency (ω_p). The change in the carrier concentration was implemented through the ω_p value, which was fed into the simulation. The simulated result is shown in Fig. 4.13, where nearly identical trends were observed as that of the experimental results. The only difference is the shift in upper polariton for experimental results (see Fig. 4.7a) is subtle, whereas it is more significant in simulation. At longer wavelengths, the imaginary part of ITO's permittivity is higher [113, 116] as shown in Fig. 4.1a. As a result, ITO might get lossy in the experiment compared to the simulation; this factor may also affect the tuning performance of the upper polari-

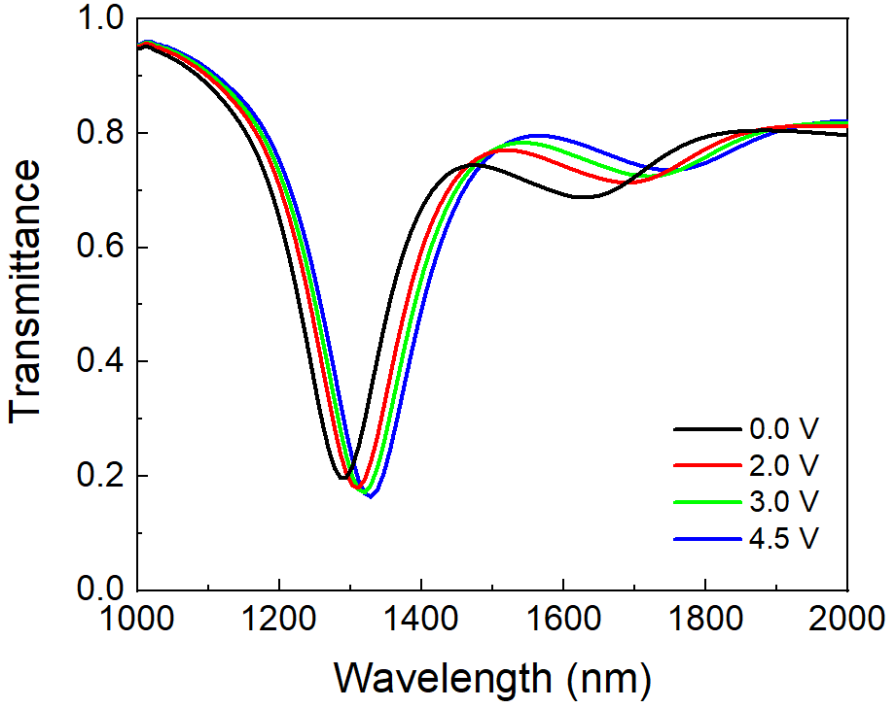


Figure 4.13 Simulated transmission spectra by varying the carrier concentration of ITO (to emulate the response at different biasing voltages).

ton [117].

4.6 Conclusion

An electrically tunable, strongly coupled ENZ-LSP system based on a novel gating scheme was developed. The strong coupling between optimally designed plasmonic nanorods and thin ITO film manifests as splitting in the transmission spectra of the structure. The developed ionic liquid-based gating system allows tuning the permittivity of the ITO film. Subsequently, the coupling strength between ENZ and LSP mode gets changed by changing the applied DC voltage. A 30 nm spectral shift was observed at lower polariton. Since the lower and upper polaritons' frequency difference quantifies the coupling strength, the spectral shift of the lower polariton via applied voltage signifies tuning the coupling strength. Dynamically tunable, strongly coupled systems are essential for exploring fundamental physics and developing ap-

plications. Therefore, our study opens a new avenue to explore many new phenomena and enhance integrated nanodevice performance by offering advanced control and tunability on strongly coupled systems. Additionally, the system exhibits reversible behavior, and the designed gating scheme is versatile, thus broadening the application horizon of photonic devices toward the tunable flat lens and transmissive spatial light modulators, which is vital for LIDAR and wireless communication.

5 PINNING EFFECT ON ITO-BASED POLARIZATION INDEPENDENT NANOSTRUCTURE

In many engineering and physics fields, resonances are key to photonic applications. The resonance wavelength of a plasmonic structure is significantly dependent on its structure (shape, dimensions, environment). If the plasmon resonance is nearly independent of the plasmonic structure's dimensions, then it relaxes the requirement of precise subwavelength features and can compensate for the fabrication errors, and also reduces the need for advanced demanding fabrications. Therefore, protecting the photonic resonance from geometrical perturbations enables the realization of photonic devices with superior properties.

In recent years, the investigation of the effects of ENZ substrate on plasmonic systems has been of great interest because ENZ materials exhibit unique optical properties, such as subwavelength confinement, wavefront control, and enhanced light-matter interaction. One particular approach is using ENZ materials as a substrate, where the reduced sensitivity of the plasmonic resonance to geometrical perturbations is achieved by minimizing the index of the substrate.

In this chapter, the nanoantennas on a glass (non-dispersive) substrate and on an ENZ (dispersive) material are experimentally explored and characterized. Largely dispersive media such as ENZ material is used as a substrate, and it is observed that the resonance shift of plasmonic antennas of different dimensions slows down near the ENZ wavelength and is less sensitive to dimension change, which diminishes the effect of antenna dimension on the spectral position of plasmon resonance. In contrast, for the non-dispersive and non-zero effective mode index (glass substrate), it is observed that the spectral shift of plasmonic antennas of different dimensions is proportional to the plasmonic antenna length. Thus, the plasmonic resonance in the

ENZ substrate case is less sensitive to the characteristics of the plasmonic antenna and is controlled mostly by the substrate. The vanishing index of refraction induces a “slowing down” of the rate of spectral shift for the antenna resonance near the ENZ wavelength. As the resonance is being pinned in a narrow spectral range, it is called “resonance pinning”. This pinning effect has already been demonstrated with an ENZ substrate such as Al-doped ZnO (AZO), indium tin oxide (ITO), and SiC [64, 118, 119] and by utilizing a hyperbolic metamaterial [120]. However, so far, the pinning effect has been shown using nanostructures that exhibit single resonance.

In this work, the universality of the pinning effect by showing the slowing down of resonance near the ENZ wavelength in a multi-resonance plasmonic system has been demonstrated. The structure design and its investigation to achieve the above-mentioned functionality are described in the following sections.

5.1 ENZ substrate characterization

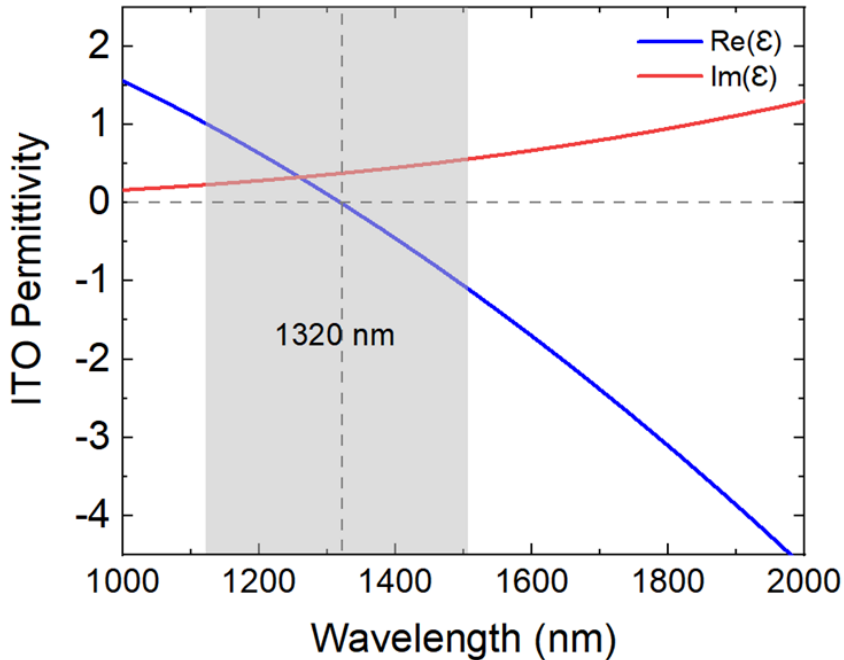


Figure 5.1 Experimentally recorded complex permittivity of 100 nm thick ITO film, blue and red solid line depicts real and imaginary part of ITO’s permittivity respectively and a grey area indicated ENZ wavelength region.

A commercially available transparent conducting oxide (TCO), 100 nm-thick ITO film on the glass slab was utilized as ENZ substrate due to its remarkable properties like near zero permittivity in the near-infrared (NIR) regime, lower optical losses in combination with enhanced light-matter interaction.

The spectroscopic ellipsometry measurement was performed to characterize the dispersion of 100 nm thick ITO film, and the complex permittivity was extracted. The real and imaginary parts of the 100 nm thick ITO film's permittivity are shown as the blue and red solid lines, respectively, in Fig. 5.1. The ENZ wavelength of 100 nm ITO film is 1320 nm where the real part of ITO's permittivity crosses zero as indicated by the grey dashed line in Fig. 5.1 and the grey shaded region highlights the near-zero permittivity span which is from 1120 nm to 1520 nm.

5.2 Polarization-independent structure design

The next step was the design of a polarization-independent plasmonic nanoantenna on the ITO substrate. To imitate the polarization-independent response, the nanorods were alternatively arranged in two different orientations. Also, if two structures with different sizes are brought together in close vicinity i.e. in a single unit cell, then it is possible to achieve two distinct resonances; by taking advantage of this, two elongated rectangular rods were designed. By combining the antennas in two different directions, the polarization-independent plasmonic nanoantenna array was finalized as presented in the schematic in Fig. 5.2a.

The devised rectangular nanoantenna array was expected to provide two plasmon resonances: transversal surface plasmon resonance and longitudinal surface plasmon resonance. To verify this and optimize the nanoantenna dimensions and supercell periodicity, the numerical simulations were performed using Lumerical FDTD. The linearly polarized plane wave source of wavelengths 500 – 1600 nm was utilized in the simulation. As the designed structure was polarization independent, therefore the exact same results were observed in both X and Y polarizations of incident light. To define ITO, the experimentally recorded permittivity of ITO as per Fig. 5.1 was fed into the simulation, and the gold (Au) was modeled using Johnson and Christy material data from the in-built material library of Lumerical. The boundary conditions were set to periodic in x and y directions and PML in the direction perpendicular to the source propagation (Z). The simulation result from the supercell design is as

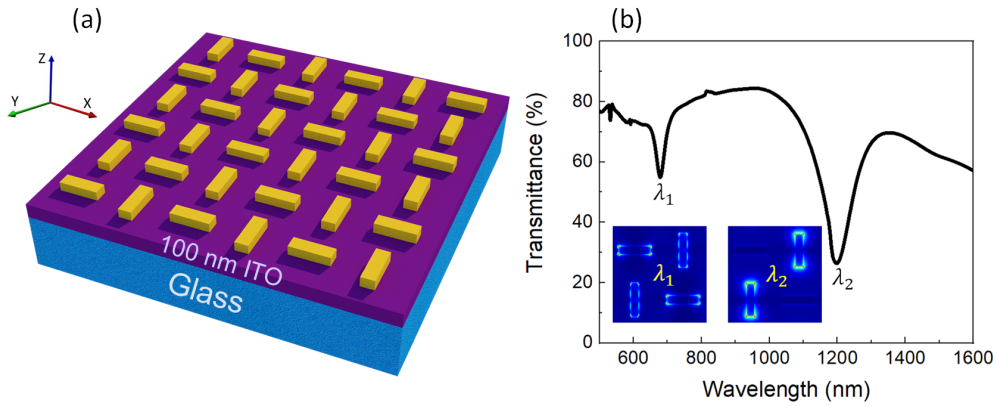


Figure 5.2 (a) Schematic of polarization-independent Au nanoantenna array of thickness 40 nm on a 100 nm-thick ITO layer on a glass substrate. (b) Simulated transmittance spectra of the plasmonic nanoantennas on the ITO substrate; the insets depict the electric field profile at the corresponding wavelength. [121]

presented in Fig. 5.2b.

For any incident polarization, there were two dipole resonances, one corresponding to the longer axis and another dipole resonance corresponding to the short axis of the elongated plasmonic nanorods. In both incident polarizations, either X or Y, two spectrally distinct resonance dips were observed in transmission spectra. The dimension of nanorods was optimized through simulations so that one of their plasmonic resonance lies in the ENZ region of the ITO film, and the second resonance is far from the ENZ region. Fig. 5.2b shows two dips, one in the ENZ region i.e., λ_2 (at 1200 nm), and another far from the ENZ region i.e., λ_1 (at 650 nm). The electric field profiles corresponding to λ_1 and λ_2 are shown in the inset of Fig. 5.2b.

The electron beam lithography (EBL) technique was utilized to fabricate the above-described polarization-independent nanostructures. The Au nanorods of different dimensions were fabricated on two different substrates; a commercially available 100 nm ITO layer and glass were used. A layer of positive resist, PMMA 950K A4, was spin-coated on top of the Glass and ITO film, and then to evaporate anisole, it was baked at 180 °C for 90 Sec. In the case of the glass substrate, after spin-coating the resist layer, the conducting polymer was spin-coated to avoid the charging effect. The array of polarization-independent nanostructure was patterned onto the resist using an electron beam lithography (EBL) technique, and the area dose used was 300 $\mu\text{C}/\text{cm}^2$. The glass sample exposed to an electron beam was washed with DI water to get rid of conducting polymer before development. Then both glass and ITO

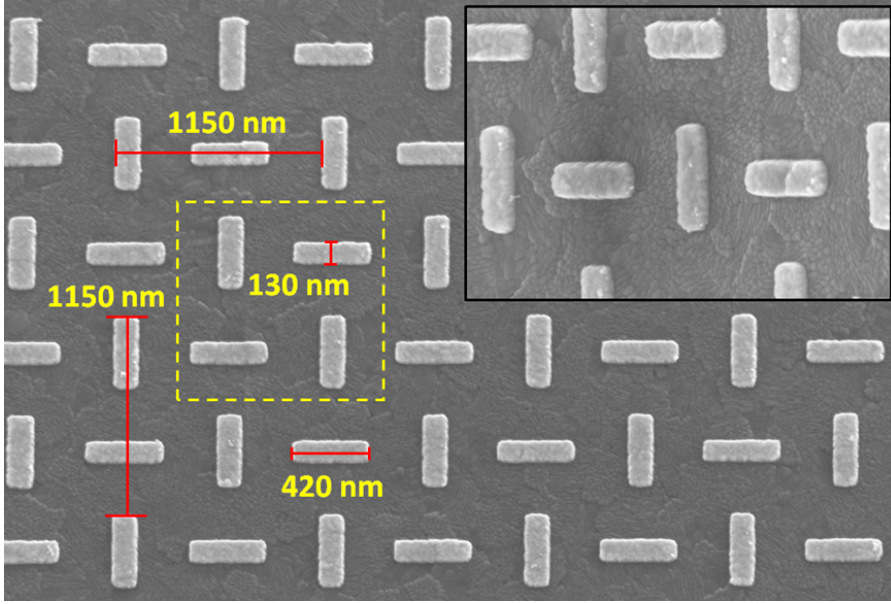


Figure 5.3 (a) SEM image shows the top view of Au nanoantenna array (scaling factor = 1, i.e., $l_s = 130$ nm and $l_l = 420$ nm), dashed yellow box indicates the supercell with supercell periodicity 1150 nm in x and y directions. The inset shows the SEM image taken at 30° tilt. [121]

samples were developed for 60 Sec in MIBK:IPA (1:3) solution, and IPA was used as a stopper. A 1/40 nm layer of Ti/Au was deposited on developed samples using an electron beam metal evaporator. After lift-off in S1165 remover at 80 °C, the sample was then cleaned using deionized water. Fig. 5.3 shows the SEM image of the top view of the fabricated nanoantenna array (corresponding to scaling factor 1) with all the spatial dimensions indicated by a red bar and supercell marked by a yellow dashed square. The inset shows the tilted SEM image captured at 30° tilt, indicating the thickness of Au rods as 40 nm. The supercell periodicity along both the x and y directions is 1150 nm.

5.3 Demonstration of resonance pinning

To verify the resonance pinning for the antennas on the ITO substrate and direct dependence of resonance wavelength position with antenna dimension for antennas on the glass substrate, a series of antennas with varying scaling factors from 0.8 to 1.2 were fabricated on both ITO and glass substrate. In Fig. 5.4, SEM images are pre-

sented with markings of all the spatial dimensions scaled by a common scaling factor that varied between 0.8 and 1.2. However, the periodicity and layer thicknesses are kept unchanged.

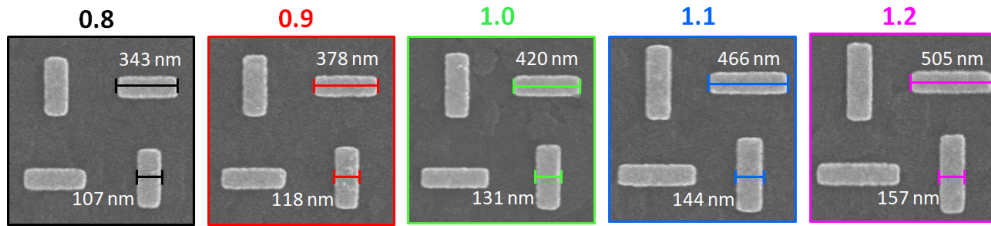


Figure 5.4 (a) SEM images of the fabricated set of samples with varying scaling factors from 0.8 to 1.2 and a constant periodicity of 1150 nm in both x and y.

Figs. 5.5a and b show the simulated transmission spectra for the plasmonic nanoantenna array upon incidence of unpolarized light for bare glass and ITO substrate, respectively, for varying scaling factors from 0.8 to 1.2. The simulated results show the slowing down of resonance shift with a change in antenna size, i.e., by varying scaling factor in the case of ITO substrate.

To further verify this, the transmission measurements were performed for all the fabricated plasmonic nanorod arrays using a multifunctional WITec alpha300C confocal Raman microscope. The samples were irradiated by a broadband light source (spectrum from 190 to 2100 nm) through a Zeiss EC 'Epiplan' DIC, 50X objective (NA=0.75) at normal incidence. The transmitted light was collected through a Zeiss EC 'Epiplan' DIC, 50X (NA=0.75) objective and launched through an optical fiber to Ocean Optics Flame spectrometer (visible region) NIRQuest spectrometer for the detection of NIR range. For both metasurfaces fabricated on ITO film and on a glass substrate, the transmission was normalized to the transmission spectrum of glass. The transmission results are as presented in Figs. 5.5c and d.

The experimental results show good agreement with the simulation results. The slight difference (resonance broadening) observed in the dip at a shorter wavelength (≈ 650 nm) can be because of experimental imperfection like detector noise in the visible range (Solid red line in Fig. 5.6) and fabrication imperfections such as inhomogeneous structures from lithographic patterning, imperfect antenna surfaces, and edges being little rounded off which were not considered in the simulations. Also, the 15% amplitude difference between experimental and simulation results mainly comes from reference baseline transmission measurement of 100 nm ITO film as

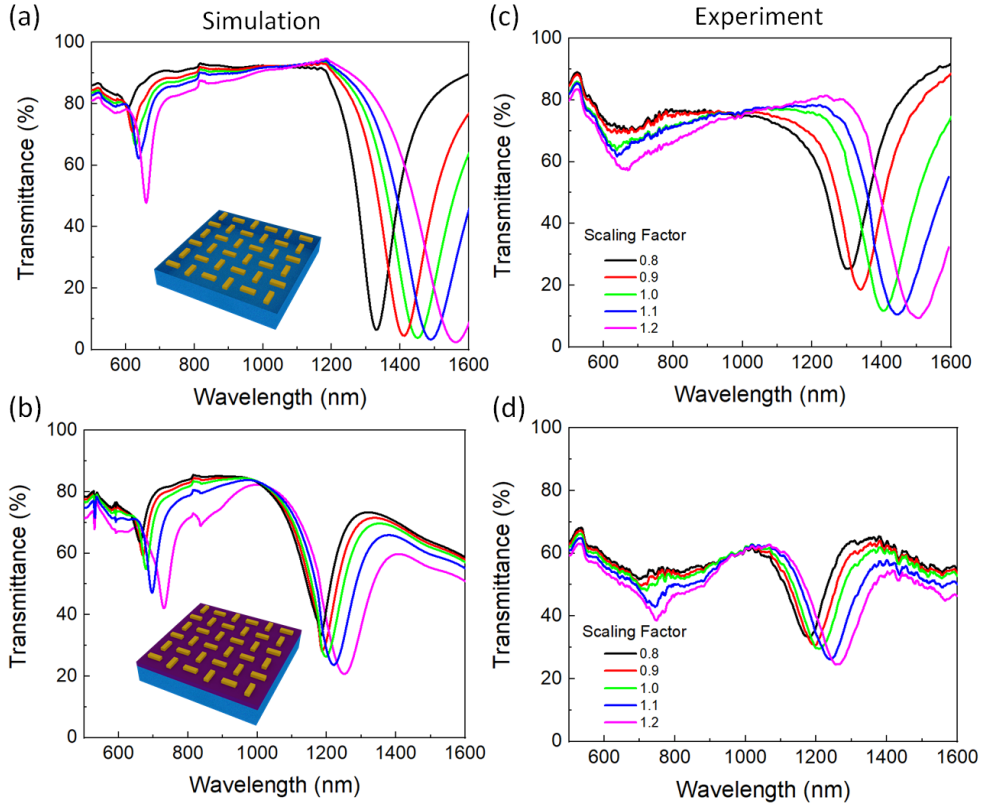


Figure 5.5 (a),(b) Simulated transmittance spectra of the supercell array of nanorods on glass and an ITO substrate at different scaling factors; the inset shows a schematic of the Au antenna array on glass and ITO, respectively. (c),(d) Experimentally recorded transmission spectra of the supercell array of nanorods on a glass and ITO substrate. [121]

shown in Fig. 5.6.

Notably, the experimental results confirm the same slowing down of resonance shift due to the presence of ENZ substrate. In both experimental and simulated results, it is evident that the change in resonance at lower wavelength is similar in both glass and ENZ substrate cases. Still, the change in resonance on the ENZ substrate is much less than the bare glass substrate with respect to different scaling factors in the ENZ region. The ITO substrate, with near zero index properties, slowed down the plasmon resonance shift near ENZ wavelength. This slowing down of the resonance can be termed pinning because the resonance was pinned in a small spectral region (ENZ wavelength region). The reason behind the pinning of spectral shift is that the mode field is predominantly concentrated (radiated) outside the ENZ substrate (in

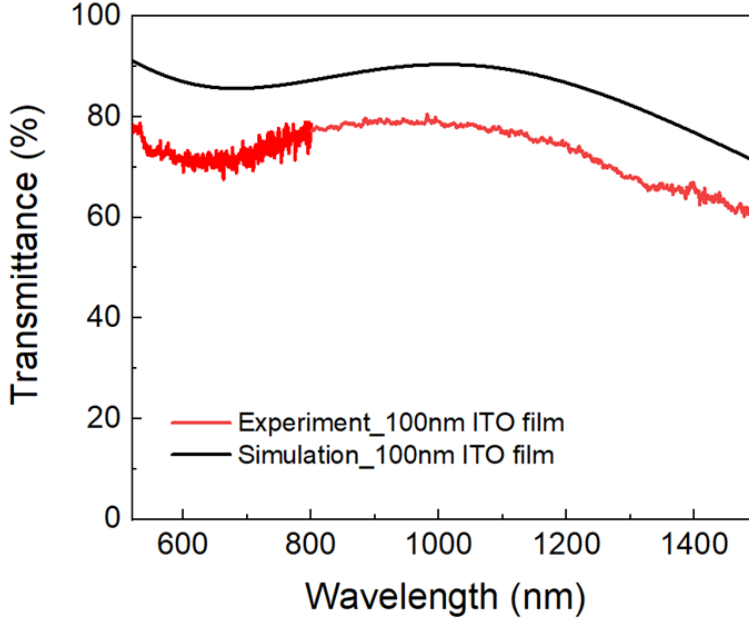


Figure 5.6 Simulated and experimental transmittance spectra of 100 nm ITO film on a glass substrate.

the air) since the air is more optically dense than the substrate at ENZ wavelength. In other words, a decrease in the effective refractive index of media surrounding the nanoantenna array compensates for the effect of the increase in antenna dimension. The spectral redshift of 80 nm on the ITO substrate while the redshift of 225 nm on a glass substrate with varying scaling factors from 0.8 to 1.2 was observed.

To clarify this observation, resonance shift ($\Delta\lambda$) was calculated from simulated and experimentally recorded transmittance spectra (Fig. 5.5) in the case of glass and ITO. The calculated shift ($\Delta\lambda$) in resonance wavelength is plotted as a function of the scaling factor for resonance at a lower wavelength (λ_1) as shown in Figs. 5.7a and b, numerically and experimentally, respectively. The solid black line represents the plasmon resonance shift on the glass, while the solid red line depicts the shift on ITO, which is evident from Figs. 5.7a and b that the change in lower wavelength resonance is nearly identical for both bare glass and ITO cases. However, in Figs. 5.7c and d, the spectral shifts at a higher wavelength (λ_2 resonance lies within the ENZ region of ITO), reveal that the shift is \approx three times smaller when nanoantennas were on ITO substrate (Plasmon-ENZ system) as compared to the case of a glass substrate.

To understand the physics behind the slowing down of resonance shift, i.e., pin-

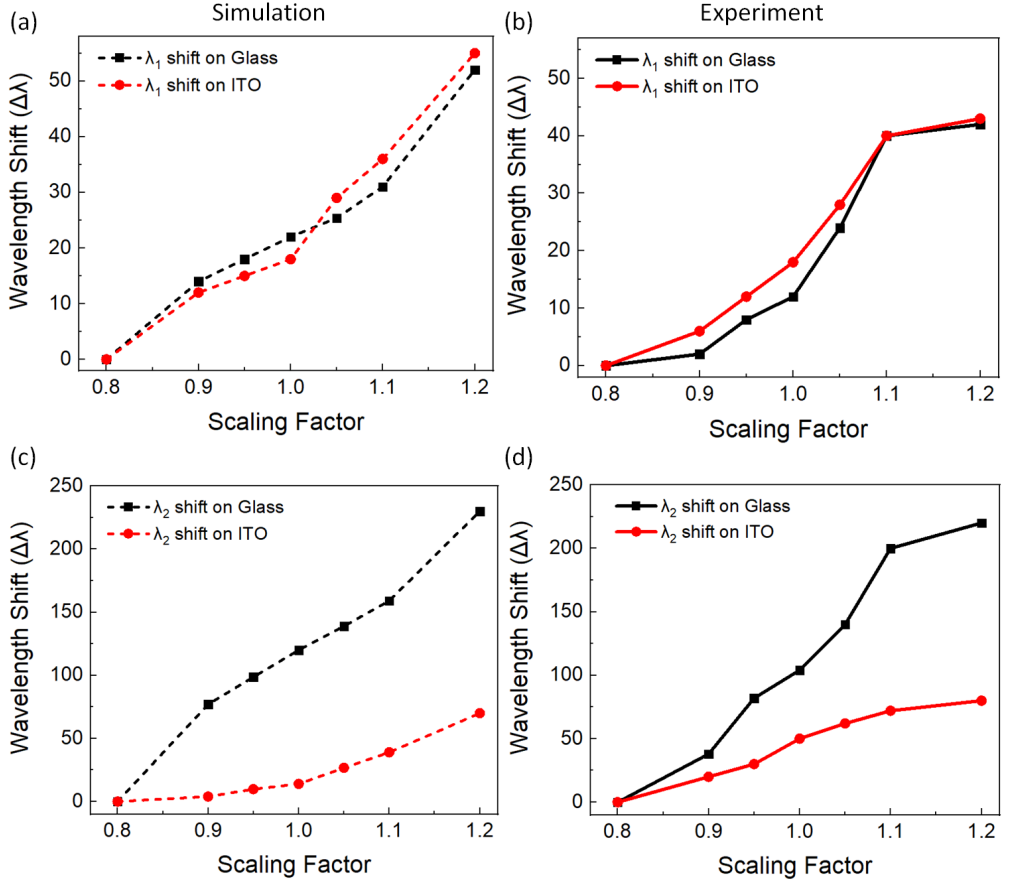


Figure 5.7 (a), (b) Simulated and experimental wavelength shift ($\Delta\lambda$) as a function of scaling factor respectively, at resonance 1 (λ_1) at a shorter wavelength. (c), (d) Simulated and experimentally recorded wavelength shifts corresponding to resonance 2 (λ_2) at a longer wavelength. [121]

ning, the rate of change of resonance wavelength as a function of antenna length [119] can be expressed as

$$\frac{\delta \lambda}{\delta l} = A \frac{n^2}{n - \lambda_0 \frac{\delta n}{\delta \lambda}}, \quad (5.1)$$

where n is the effective index, A is constant, and λ_0 is the free space wavelength. For non-dispersive medium, i.e., $\delta n / \delta \lambda = 0$, the resonance wavelength becomes proportional to the length of the nanoantenna and the index ($\lambda \propto Anl$).

Fig. 5.8 shows a comparative plot of the resonance wavelength for bare glass and ITO substrate. The resonance wavelength (λ) is plotted against antenna length (l_l) analytically according to the relation given in Ref. [119], which was based on the

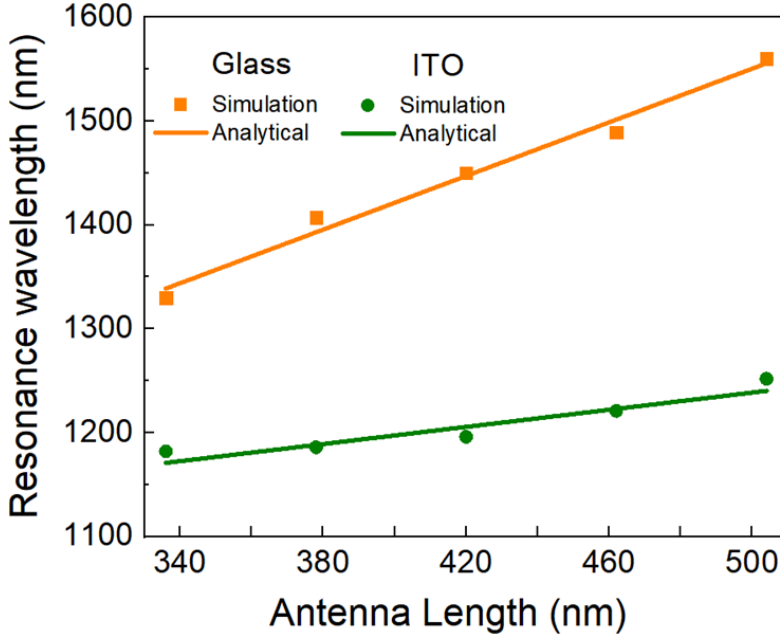


Figure 5.8 Resonant wavelength (λ) as a function of antenna length (l_1) for the Glass (orange) and ITO (Green) substrates. The solid lines are calculated analytically, and square and circular markers result from FDTD numerical calculations. [121]

Fabry-Perot model. The square and circular markers depict the resonance wavelength extracted using FDTD numerical calculations. The simulation results show good agreement with analytical results.

5.4 Conclusion

This chapter demonstrates that compared to the bare glass substrate, the designed plasmonic metasurface exhibits a three-fold reduction in the resonance wavelength shift only near ENZ wavelength as a function of antenna length. This work reflects an important study that would demonstrate selective control on plasmon resonance increases the versatility and functionality of plasmonic structures and provides foundational insight into this exotic phenomenon of ENZ material. Thus, these findings will create a new direction toward advanced plasmonic applications.

6 SUMMARY AND FUTURE WORK

The objective of this thesis was to demonstrate multiple paradigms of light-matter interactions and their applicability to unveil new physics and demonstrate novel applications. Keeping this theme, the organization of the thesis was outlined. The works presented in the thesis structured a new prospect to develop highly efficient and cost-effective photonic devices with active tunability. It lays the platform for next-generation photonic and optoelectronic devices.

The first chapter starts with the introduction of a broad perspective and the scope of the thesis. Since the significant breakthroughs of photonics are stimulated by the discovery of active nanophotonics, enabling on-demand tailoring of light-matter interaction, therefore, this chapter outlines the emergence and applications of nanophotonics. Then, chapter 2 lays down the foundation of the thesis by providing a brief theoretical overview of plasmonics, MIM, and ENZ materials. The plasmonic structures used in this thesis are primarily gold nanorods.

Furthermore, the MIM cavity is used to unveil the underlying mechanism for the enhancement of emission from a fluorescent dye under a large-density photonic environment. The structural configuration of the MIM cavity used in this thesis is as follows: an optically thick metal film at the bottom on the substrate, followed by a dielectric layer and an optically thin metal film at the top. The structural simplicity, ease of fabrication, and ability to tune the spectral position of resonance are the critical properties of MIM structure that allow tailoring the light-matter interactions. Chapter 3 presents a systematic study that is carried out to unveil the mechanism of emission enhancement when a fluorescent dye is kept under a photonic environment with a large density of states. Several MIM cavities with varying dielectric thickness were fabricated to achieve different resonance wavelengths. The thickness of the dielectric layer was judiciously chosen such that the spectral position of the MIM cavity resonance spanned from the absorption wavelength to the emission wavelength of the fluorescent dye. The studies revealed that the remarkable enhancement in

the photo-luminescent intensities is not only attributed to the spontaneous rate enhancement of dye, but a significant contribution also comes from the excitation rate enhancement. This opened up a new avenue to engineer the emission properties of any emitter and provide flexibility in designing a photonic device. After exploring the underlying mechanism for emission enhancement, this knowledge was used to achieve active tunable emission. Instead of passively changing the dielectric layer's thickness, the hydrogel was employed as a dielectric layer of the MIM, whose thickness was tuned by changing the ambient humidity. By incorporating dyes with hydrogel, an active tuning in the emission intensities is demonstrated by changing the ambient humidity. Interestingly, the whole process was reversible, further verified by the experiment.

The coupling strength is an important metric that quantifies the light-matter interactions. In particular, the strong coupling is viable as in this regime; the coupling mechanism dominates the competing loss mechanism. Motivated by the exciting opportunities and possibilities opened up by strong coupling, chapter 4 introduced a novel gating scheme to tune the coupling strength of strongly coupled systems. Indium tin oxide (ITO) and gold nanorod array were used as ENZ material and plasmonic system, respectively, to realize the strong coupling. The ionic gel was used as a medium that facilitates the biasing. Interestingly, integrating plasmonic systems with ENZ materials provides a fertile play for studying the strong coupling. More exciting and new phenomena emerge at the ENZ wavelength due to the vanishing nature of the refractive index. Leveraging this property, a polarization-independent plasmonic resonator on ENZ substrate is presented whose resonance wavelength exhibits less sensitivity toward geometrical perturbation.

6.1 Future research directions

Numerous threads of this thesis research works can potentially be extended into multiple subsequent works. For instance, one exciting extension of chapter 1 (Publication I) and research direction could be, designing a MIM planar system that supports two cavity modes in a single structure to overlap modes with the absorption and the emission spectrum of an emitter.

For MIM nano-cavities, it is possible to possess two distinct resonant modes with high-quality factors. One can shift the spectral position of these two modes by vary-

ing the thickness of the insulator layer. This creates the opportunity to overlap the absorption band of the emitter with the cavity mode. In contrast, the emission spectrum can be overlapped with the higher-order cavity mode with a larger wavelength. However, achieving these two spectral overlaps is a challenge, as the large spectral gap between the absorption and emission of the emitter is desired; plus, to the best of my knowledge, organic dye molecules don't exhibit enough significant Stokes shifts. Nevertheless, Lead sulfide (PbS) quantum dots with a broad absorption band in UV-VIS spectral range and emission spectrum in the NIR range can be an alternative to fulfill the criteria to achieve such a system. As a result, one can achieve a higher spontaneous emission enhancement for the incorporated quantum emitter inside the nano-cavity.

Another possibility is integrating the emitters exhibiting different emission and absorption wavelengths with hydrogel-based MIM cavities. This could be useful for holography applications, whereby spatially contorting regions can be created selectively by increasing the emission of specific wavelengths. Furthermore, a hydrogel-based MIM cavity offers large spectral tunability, which can be used further to design active band or color filters that are useful for communication applications.

Also, the devised gating scheme has the potential to operate both at transmission and reflection modes. Active beam steering can be achieved by incorporating this gating scheme into the phase gradient metasurface.

Importantly, so far, the resonance pinning effect on ENZ substrate was only shown without any real-time control; the real-time controlled resonance pinning counterpart is still elusive. In this context, further by incorporating a novel gating scheme, dynamic tuning of the resonance pinning effect can be realized, which is advantageous for various applications such as imaging and sensing.

REFERENCES

- [1] T. H. MAIMAN. Stimulated Optical Radiation in Ruby. *Nature* 187.4736 (1960), 493–494. DOI: 10.1038/187493a0.
- [2] H. A. Atwater and A. Polman. Plasmonics for improved photovoltaic devices. *Nature Materials* 9.3 (2010), 205–213. DOI: 10.1038/nmat2629.
- [3] L. Britnell, R. M. Ribeiro, A. Eckmann, R. Jalil, B. D. Belle, A. Mishchenko, Y.-J. Kim, R. V. Gorbachev, T. Georgiou, S. V. Morozov, A. N. Grigorenko, A. K. Geim, C. Casiraghi, A. H. C. Neto and K. S. Novoselov. Strong Light-Matter Interactions in Heterostructures of Atomically Thin Films. *Science* 340.6138 (2013), 1311–1314. DOI: 10.1126/science.1235547.
- [4] F. Fassioli, R. Dinshaw, P. C. Arpin and G. D. Scholes. Photosynthetic light harvesting: excitons and coherence. *Journal of The Royal Society Interface* 11.92 (2014), 20130901. DOI: 10.1098/rsif.2013.0901.
- [5] B. Keimer and J. E. Moore. The physics of quantum materials. *Nature Physics* 13.11 (2017), 1045–1055. DOI: 10.1038/nphys4302.
- [6] Y. Tokura, M. Kawasaki and N. Nagaosa. Emergent functions of quantum materials. *Nature Physics* 13.11 (2017), 1056–1068. DOI: 10.1038/nphys4274.
- [7] J. Demsar. Light-induced superconductivity. *Nature Physics* 12.11 (2016), 202–203. DOI: 10.1038/nphys3687.
- [8] J. Y. Ou, E. Plum, L. Jiang and N. I. Zheludev. Reconfigurable Photonic Metamaterials. *Nano Letters* 11.5 (2011), 2142–2144. DOI: 10.1021/nl200791r.
- [9] Y. Yao, R. Shankar, M. A. Kats, Y. Song, J. Kong, M. Loncar and F. Capasso. Electrically Tunable Metasurface Perfect Absorbers for Ultrathin Mid-Infrared Optical Modulators. *Nano Letters* 14.11 (2014), 6526–6532. DOI: 10.1021/nl503104n.

- [10] Z. Fang, Y. Wang, A. E. Schlather, Z. Liu, P. M. Ajayan, F. J. García de Abajo, P. Nordlander, X. Zhu and N. J. Halas. Active Tunable Absorption Enhancement with Graphene Nanodisk Arrays. *Nano Letters* 14.1 (2014), 299–304. DOI: 10.1021/nl404042h.
- [11] J. Lee, S. Jung, P.-Y. Chen, F. Lu, F. Demmerle, G. Boehm, M.-C. Amann, A. Alù and M. A. Belkin. Ultrafast Electrically Tunable Polaritonic Metasurfaces. *Advanced Optical Materials* 2.11 (2014), 1057–1063. DOI: <https://doi.org/10.1002/adom.201400185>.
- [12] R. Dhama, A. Panahpour, T. Pihlava, D. Ghindani and H. Caglayan. All-optical switching based on plasmon-induced Enhancement of Index of Refraction. *Nature Communications* 13.1 (2022), 3114. DOI: 10.1038/s41467-022-30750-5.
- [13] H.-T. Chen, J. F. O’Hara, A. K. Azad, A. J. Taylor, R. D. Averitt, D. B. Shrekenhamer and W. J. Padilla. Experimental demonstration of frequency-agile terahertz metamaterials. *Nature Photonics* 2.5 (2008), 295–298. DOI: 10.1038/nphoton.2008.52.
- [14] Y. Yang, W. Wang, A. Boulesbaa, I. I. Kravchenko, D. P. Briggs, A. Puretzky, D. Geohegan and J. Valentine. Nonlinear Fano-Resonant Dielectric Metasurfaces. *Nano Letters* 15.11 (2015), 7388–7393. DOI: 10.1021/acs.nanolett.5b02802.
- [15] T. Driscoll, S. Palit, M. M. Qazilbash, M. Brehm, F. Keilmann, B.-G. Chae, S.-J. Yun, H.-T. Kim, S. Y. Cho, N. M. Jokerst, D. R. Smith and D. N. Basov. Dynamic tuning of an infrared hybrid-metamaterial resonance using vanadium dioxide. *Applied Physics Letters* 93.2 (2008), 024101. DOI: 10.1063/1.2956675.
- [16] Y. G. Chen, T. S. Kao, B. Ng, X. Li, X. G. Luo, B. Luk’yanchuk, S. A. Maier and M. H. Hong. *Opt. Express* 21.11 (2013), 13691–13698. DOI: 10.1364/OE.21.013691.
- [17] Y.-W. Huang, H. W. H. Lee, R. Sokhoyan, R. A. Pala, K. Thyagarajan, S. Han, D. P. Tsai and H. A. Atwater. Gate-Tunable Conducting Oxide Metasurfaces. *Nano Letters* 16.9 (2016), 5319–5325. DOI: 10.1021/acs.nanolett.6b00555.

- [18] D. Ghindani, I. Issah, S. Chervinskii, M. Lahikainen, K. Kuntze, A. Priimagi and H. Caglayan. Humidity-Controlled Tunable Emission in a Dye-Incorporated Metal-Hydrogel-Metal Cavity. *ACS Photonics* 9.7 (2022), 2287–2294. DOI: 10.1021/acsp Photonics.2c00202.
- [19] S. Chervinskii, I. Issah, M. Lahikainen, A. R. Rashed, K. Kuntze, A. Priimagi and H. Caglayan. Humidity- and Temperature-Tunable Metal-Hydrogel-Metal Reflective Filters. *ACS Applied Materials and Interfaces* 13.42 (2021), 50564–50572. DOI: 10.1021/acsa mi.1c15616.
- [20] S. C. Ambhire, S. Palkhivala, A. Agrawal, A. Gupta, G. Rana, R. Mehta, D. Ghindani, A. Bhattacharya, V. G. Achanta and S. S. Prabhu. Pattern and Peel method for fabricating mechanically tunable terahertz metasurface on an elastomeric substrate. *Opt. Mater. Express* 8.11 (2018), 3382–3391. DOI: 10.1364/OME.8.003382.
- [21] H.-T. Chen, W. J. Padilla, J. M. O. Zide, A. C. Gossard, A. J. Taylor and R. D. Averitt. Active terahertz metamaterial devices. *Nature* 444.7119 (2006), 597–600. DOI: 10.1038/nature05343.
- [22] G. Kafaie Shirmanesh, R. Sokhoyan, R. A. Pala and H. A. Atwater. Dual-Gated Active Metasurface at 1550 nm with Wide (>300) Phase Tunability. *Nano Letters* 18.5 (2018), 2957–2963. DOI: 10.1021/acs.nanolett.8b00351.
- [23] R. Yan, D. Gargas and P. Yang. Large-area enhancement of far-field fluorescence intensity using planar nanostructures. *Nanowire photonics* 3.10 (2009), 569–576. DOI: 10.1038/nphoton.2009.184.
- [24] J. Yang, S. Gurung, S. Bej, P. Ni and H. W. H. Lee. Active optical metasurfaces: comprehensive review on physics, mechanisms, and prospective applications. *Reports on Progress in Physics* 85.3 (2022), 036101. DOI: 10.1088/1361-6633/ac2aaf.
- [25] G. K. Shirmanesh, R. Sokhoyan, P. C. Wu and H. A. Atwater. Electro-optically Tunable Multifunctional Metasurfaces. *ACS Nano* 14.6 (2020), 6912–6920. DOI: 10.1021/acsnano.0c01269.
- [26] B. Wang, B. Quan, J. He, Z. Xie, X. Wang, J. Li, Q. Kan and Y. Zhang. Wavelength de-multiplexing metasurface hologram. *Scientific Reports* 6.1 (2016), 35657. DOI: 10.1038/srep35657.

- [27] C. Spagele, M. Tamagnone, D. Kazakov, M. Ossiander, M. Piccardo and F. Capasso. Multifunctional wide-angle optics and lasing based on supercell metasurfaces. *Nature Communications* 12.1 (2021), 3787. DOI: 10.1038/s41467-021-24071-2.
- [28] A. Tittl, A. John-Herpin, A. Leitis, E. R. Arvelo and H. Altug. Metasurface-Based Molecular Biosensing Aided by Artificial Intelligence. *Angewandte Chemie International Edition* 58.42 (2019), 14810–14822. DOI: <https://doi.org/10.1002/anie.201901443>.
- [29] D. Lu and Z. Liu. Hyperlenses and metalenses for far-field super-resolution imaging. *Nature Communications* 3.1 (2012), 1205. DOI: 10.1038/ncomms2176.
- [30] Y. Intaravanne and X. Chen. Recent advances in optical metasurfaces for polarization detection and engineered polarization profiles. *Nanophotonics* 9.5 (2020), 1003–1014. DOI: [doi:10.1515/nanoph-2019-0479](https://doi.org/10.1515/nanoph-2019-0479).
- [31] G.-Y. Lee, J.-Y. Hong, S. Hwang, S. Moon, H. Kang, S. Jeon, H. Kim, J.-H. Jeong and B. Lee. Metasurface eyepiece for augmented reality. *Nature Communications* 9.1 (2018), 4562. DOI: 10.1038/s41467-018-07011-5.
- [32] J. Kim, Y. Jeong, M. Stengel, K. Aksit, R. Albert, B. Boudaoud, T. Greer, J. Kim, W. Lopes, Z. Majercik, P. Shirley, J. Spjut, M. McGuire and D. Luebke. Foveated AR: Dynamically-Foveated Augmented Reality Display. *ACM Trans. Graph.* 38.4 (2019), 15. DOI: 10.1145/3306346.3322987.
- [33] S. Lin, Y. Chen and Z. J. Wong. High-performance optical beam steering with nanophotonics. *Nanophotonics* 11.11 (2022), 2617–2638. DOI: [doi:10.1515/nanoph-2021-0805](https://doi.org/10.1515/nanoph-2021-0805).
- [34] Z. He, X. Sui, G. Jin and L. Cao. Progress in virtual reality and augmented reality based on holographic display. *Appl. Opt.* 58.5 (2019), A74–A81. DOI: 10.1364/AO.58.000A74.
- [35] J. Li, S. Kamin, G. Zheng, F. Neubrech, S. Zhang and N. Liu. Addressable metasurfaces for dynamic holography and optical information encryption. *Science Advances* 4.6 (2018), eaar6768. DOI: 10.1126/sciadv.aar6768.

- [36] J. Park, J.-H. Kang, X. Liu, S. J. Maddox, K. Tang, P. C. McIntyre, S. R. Bank and M. L. Brongersma. Dynamic thermal emission control with InAs-based plasmonic metasurfaces. *Science Advances* 4.12 (2018), eaat3163. DOI: 10.1126/sciadv.aat3163.
- [37] X. Guo, Y. Ding, Y. Duan and X. Ni. Nonreciprocal metasurface with space-time phase modulation. *Light: Science and Applications* 8.1 (2019), 123. DOI: 10.1038/s41377-019-0225-z.
- [38] F. Yesilkoy, E. R. Arvelo, Y. Jahani, M. Liu, A. Tittl, V. Cevher, Y. Kivshar and H. Altug. Ultrasensitive hyperspectral imaging and biodetection enabled by dielectric metasurfaces. *Nature Photonics* 13.6 (2019), 390–396. DOI: 10.1038/s41566-019-0394-6.
- [39] J. Leach, G. M. Gibson, M. J. Padgett, E. Esposito, G. McConnell, A. J. Wright and J. M. Girkin. Generation of achromatic Bessel beams using a compensated spatial light modulator. *Opt. Express* 14.12 (2006), 5581–5587. DOI: 10.1364/OE.14.005581.
- [40] Y. Liu, H. Xu, F. Stief, N. Zhitenev and M. Yu. Far-field superfocusing with an optical fiber based surface plasmonic lens made of nanoscale concentric annular slits. *Opt. Express* 19.21 (2011), 20233–20243. DOI: 10.1364/OE.19.020233.
- [41] M. G. Wood, S. Campione, S. Parameswaran, T. S. Luk, J. R. Wendt, D. K. Serkland and G. A. Keeler. Gigahertz speed operation of epsilon-near-zero silicon photonic modulators. *Optica* 5.3 (2018), 233–236. DOI: 10.1364/OPTICA.5.000233.
- [42] V. G. Kravets, A. V. Kabashin, W. L. Barnes and A. N. Grigorenko. Plasmonic Surface Lattice Resonances: A Review of Properties and Applications. *Chemical Reviews* 118.12 (2018), 5912–5951. DOI: 10.1021/acs.chemrev.8b00243.
- [43] K. L. Kelly, E. Coronado, L. L. Zhao and G. C. Schatz. The Optical Properties of Metal Nanoparticles: The Influence of Size, Shape, and Dielectric Environment. *The Journal of Physical Chemistry B* 107.3 (2003), 668–677. DOI: 10.1021/jp026731y.
- [44] W. L. Barnes. Particle plasmons: Why shape matters. *American Journal of Physics* 84.8 (2016), 593–601. DOI: 10.1119/1.4948402.

- [45] J. N. Anker, W. P. Hall, O. Lyandres, N. C. Shah, J. Zhao and R. P. Van Duyne. Biosensing with plasmonic nanosensors. *Nature Materials* 7.6 (2008), 442–453. DOI: 10.1038/nmat2162.
- [46] A. G. Brolo. Plasmonics for future biosensors. *Nature Photonics* 6.11 (2012), 709–713. DOI: 10.1038/nphoton.2012.266.
- [47] J. L. West and N. J. Halas. Engineered Nanomaterials for Biophotonics Applications: Improving Sensing, Imaging, and Therapeutics. *Annual Review of Biomedical Engineering* 5.1 (2003), 285–292. DOI: 10.1146/annurev.bioeng.5.011303.120723.
- [48] J. Homola. Present and future of surface plasmon resonance biosensors. *Analytical and Bioanalytical Chemistry* 377.3 (2003), 528–539. DOI: 10.1007/s00216-003-2101-0.
- [49] L. Ju, B. Geng, J. Horng, C. Girit, M. Martin, Z. Hao, H. A. Bechtel, X. Liang, A. Zettl, Y. R. Shen and F. Wang. Graphene plasmonics for tunable terahertz metamaterials. *Nature Nanotechnology* 6.10 (2011), 630–634. DOI: 10.1038/nnano.2011.146.
- [50] W. Zhou, J. Lee, J. Nanda, S. T. Pantelides, S. J. Pennycook and J.-C. Idrobo. Atomically localized plasmon enhancement in monolayer graphene. *Nature Nanotechnology* 7.3 (2012), 161–165. DOI: 10.1038/nnano.2011.252.
- [51] J. Hao, Q. Ren, Z. An, X. Huang, Z. Chen, M. Qiu and L. Zhou. Optical metamaterial for polarization control. *Phys. Rev. A* 80 (2009), 023807. DOI: 10.1103/PhysRevA.80.023807.
- [52] J. Hao, Y. Yuan, L. Ran, T. Jiang, J. A. Kong, C. T. Chan and L. Zhou. Manipulating Electromagnetic Wave Polarizations by Anisotropic Metamaterials. *Phys. Rev. Lett.* 99 (2007), 063908. DOI: 10.1103/PhysRevLett.99.063908.
- [53] H. Tao, C. M. Bingham, A. C. Strikwerda, D. Pilon, D. Shrekenhamer, N. I. Landy, K. Fan, X. Zhang, W. J. Padilla and R. D. Averitt. Highly flexible wide angle of incidence terahertz metamaterial absorber: Design, fabrication, and characterization. *Phys. Rev. B* 78 (2008), 241103. DOI: 10.1103/PhysRevB.78.241103.

- [54] N. Liu, M. Mesch, T. Weiss, M. Hentschel and H. Giessen. Infrared Perfect Absorber and Its Application As Plasmonic Sensor. *Nano Letters* 10.7 (2010), 2342–2348. DOI: 10.1021/nl9041033.
- [55] X. Li, S. Xiao, B. Cai, Q. He, T. J. Cui and L. Zhou. Flat metasurfaces to focus electromagnetic waves in reflection geometry. *Opt. Lett.* 37.23 (2012), 4940–4942. DOI: 10.1364/OL.37.004940.
- [56] A. Pors, M. G. Nielsen, R. L. Eriksen and S. I. Bozhevolnyi. Broadband Focusing Flat Mirrors Based on Plasmonic Gradient Metasurfaces. *Nano Letters* 13.2 (2013), 829–834. DOI: 10.1021/nl304761m.
- [57] W. T. Chen, K.-Y. Yang, C.-M. Wang, Y.-W. Huang, G. Sun, I.-D. Chiang, C. Y. Liao, W.-L. Hsu, H. T. Lin, S. Sun, L. Zhou, A. Q. Liu and D. P. Tsai. High-Efficiency Broadband Meta-Hologram with Polarization-Controlled Dual Images. *Nano Letters* 14.1 (2014), 225–230. DOI: 10.1021/nl403811d.
- [58] J. Kim, H. Oh, M. Seo and M. Lee. Generation of Reflection Colors from Metal–Insulator–Metal Cavity Structure Enabled by Thickness-Dependent Refractive Indices of Metal Thin Film. *ACS Photonics* 6.9 (2019), 2342–2349. DOI: 10.1021/acsp Photonics.9b00894.
- [59] J. Hao, J. Wang, X. Liu, W. J. Padilla, L. Zhou and M. Qiu. High performance optical absorber based on a plasmonic metamaterial. *Applied Physics Letters* 96.25 (2010), 251104. DOI: 10.1063/1.3442904.
- [60] C. Wu, B. Neuner, G. Shvets, J. John, A. Milder, B. Zollars and S. Savoy. Large-area wide-angle spectrally selective plasmonic absorber. *Phys. Rev. B* 84 (2011), 075102. DOI: 10.1103/PhysRevB.84.075102.
- [61] M. G. Nielsen, A. Pors, O. Albrechtsen and S. I. Bozhevolnyi. Efficient absorption of visible radiation by gap plasmon resonators. *Opt. Express* 20.12 (2012), 13311–13319. DOI: 10.1364/OE.20.013311.
- [62] M. K. Hedayati, M. Javaherirahim, B. Mozooni, R. Abdelaziz, A. Tavassolizadeh, V. S. K. Chakravadhanula, V. Zaporozhchenko, T. Strunkus, F. Faupel and M. Elbahri. Design of a Perfect Black Absorber at Visible Frequencies Using Plasmonic Metamaterials. *Advanced Materials* 23.45 (2011), 5410–5414. DOI: <https://doi.org/10.1002/adma.201102646>.

- [63] M. Anderegg, B. Feuerbacher and B. Fitton. Optically Excited Longitudinal Plasmons in Potassium. *Phys. Rev. Lett.* 27 (1971), 1565–1568. DOI: 10.1103/PhysRevLett.27.1565.
- [64] J. Kim, A. Dutta, G. V. Naik, A. J. Giles, F. J. Bezares, C. T. Ellis, J. G. Tischler, A. M. Mahmoud, H. Caglayan, O. J. Glembocki, A. V. Kildishev, J. D. Caldwell, A. Boltasseva and N. Engheta. Role of epsilon-near-zero substrates in the optical response of plasmonic antennas. *Optica* 3.3 (2016), 339–346. DOI: 10.1364/OPTICA.3.000339.
- [65] J. D. Caldwell, L. Lindsay, V. Giannini, I. Vurgaftman, T. L. Reinecke, S. A. Maier and O. J. Glembocki. Low-loss, infrared and terahertz nanophotonics using surface phonon polaritons. *Nanophotonics* 4.1 (2015), 44–68. DOI: doi: 10.1515/nanoph-2014-0003.
- [66] N. Kinsey, C. DeVault, J. Kim, M. Ferrera, V. M. Shalaev and A. Boltasseva. Epsilon-near-zero Al-doped ZnO for ultrafast switching at telecom wavelengths. *Optica* 2.7 (2015), 616–622. DOI: 10.1364/OPTICA.2.000616.
- [67] G. V. Naik, J. Kim and A. Boltasseva. Oxides and nitrides as alternative plasmonic materials in the optical range [Invited]. *Opt. Mater. Express* 1.6 (2011), 1090–1099. DOI: 10.1364/OME.1.001090.
- [68] G. V. Naik, V. M. Shalaev and A. Boltasseva. Alternative Plasmonic Materials: Beyond Gold and Silver. *Advanced Materials* 25.24 (2013), 3264–3294. DOI: 10.1002/adma.201205076.
- [69] D. Ghindani, A. R. Rashed, M. Habib and H. Caglayan. Gate Tunable Coupling of Epsilon-Near-Zero and Plasmonic Modes. *Advanced Optical Materials* 9.22 (2021), 2100800. DOI: <https://doi.org/10.1002/adom.202100800>.
- [70] C. Liu, M. Z. Alam, K. Pang, K. Manukyan, O. Reshef, Y. Zhou, S. Choudhary, J. Patrow, A. Pennathurs, H. Song, Z. Zhao, R. Zhang, F. Alishahi, A. Fallahpour, Y. Cao, A. Almain, J. M. Dawlaty, M. Tur, R. W. Boyd and A. E. Willner. Photon Acceleration Using a Time-Varying Epsilon-near-Zero Metasurface. *ACS Photonics* 8.3 (2021), 716–720. DOI: 10.1021/acsp Photonics.0c01929.
- [71] R. W. Ziolkowski. Propagation in and scattering from a matched metamaterial having a zero index of refraction. *Phys. Rev. E* 70 (2004), 046608. DOI: 10.1103/PhysRevE.70.046608.

- [72] M. Silveirinha and N. Engheta. Tunneling of Electromagnetic Energy through Subwavelength Channels and Bends using epsilon-Near-Zero Materials. *Phys. Rev. Lett.* 97 (2006), 157403. DOI: 10.1103/PhysRevLett.97.157403.
- [73] A. Alu, M. G. Silveirinha and N. Engheta. Transmission-line analysis of epsilon-near-zero-filled narrow channels. *Phys. Rev. E* 78 (2008), 016604. DOI: 10.1103/PhysRevE.78.016604.
- [74] B. Edwards, A. Alù, M. G. Silveirinha and N. Engheta. Reflectionless sharp bends and corners in waveguides using epsilon-near-zero effects. *Journal of Applied Physics* 105.4 (2009), 044905. DOI: 10.1063/1.3074506.
- [75] S. Enoch, G. Tayeb, P. Sabouroux, N. Guerin and P. Vincent. A Metamaterial for Directive Emission. *Phys. Rev. Lett.* 89 (2002), 213902. DOI: 10.1103/PhysRevLett.89.213902.
- [76] A. Alu, M. G. Silveirinha, A. Salandrino and N. Engheta. Epsilon-near-zero metamaterials and electromagnetic sources: Tailoring the radiation phase pattern. *Phys. Rev. B* 75 (2007), 155410. DOI: 10.1103/PhysRevB.75.155410.
- [77] M. Navarro-Cia, M. Beruete, I. Campillo and M. Sorolla. Enhanced lens by epsilon and mu near-zero metamaterial boosted by extraordinary optical transmission. *Phys. Rev. B* 83 (2011), 115112. DOI: 10.1103/PhysRevB.83.115112.
- [78] M. Navarro-Cia, M. Beruete, M. Sorolla and N. Engheta. Lensing system and Fourier transformation using epsilon-near-zero metamaterials. *Phys. Rev. B* 86 (2012), 165130. DOI: 10.1103/PhysRevB.86.165130.
- [79] V. Pacheco-Pena, V. Torres, B. Orazbayev, M. Beruete, M. Navarro-Cía, M. Sorolla and N. Engheta. Mechanical 144 GHz beam steering with all-metallic epsilon-near-zero lens antenna. *Applied Physics Letters* 105.24 (2014), 243503. DOI: 10.1063/1.4903865.
- [80] A. Alu and N. Engheta. Boosting Molecular Fluorescence with a Plasmonic Nanolauncher. *Phys. Rev. Lett.* 103 (2009), 043902. DOI: 10.1103/PhysRevLett.103.043902.
- [81] X. Niu, X. Hu, S. Chu and Q. Gong. Epsilon-Near-Zero Photonics: A New Platform for Integrated Devices. *Advanced Optical Materials* 6.10 (2018), 1701292. DOI: <https://doi.org/10.1002/adom.201701292>.

- [82] A. Alu and N. Engheta. All Optical Metamaterial Circuit Board at the Nanoscale. *Phys. Rev. Lett.* 103 (2009), 143902. DOI: 10.1103/PhysRevLett.103.143902.
- [83] A. Alu and N. Engheta. Optical ‘Shorting Wires’. *Opt. Express* 15.21 (2007), 13773–13782. DOI: 10.1364/OE.15.013773.
- [84] B. Edwards and N. Engheta. Experimental Verification of Displacement-Current Conduits in Metamaterials-Inspired Optical Circuitry. *Phys. Rev. Lett.* 108 (2012), 193902. DOI: 10.1103/PhysRevLett.108.193902.
- [85] Y. Li, I. Liberal, C. D. Giovampaola and N. Engheta. Waveguide metatronics: Lumped circuitry based on structural dispersion. *Science Advances* 2.6 (2016), e1501790. DOI: 10.1126/sciadv.1501790.
- [86] I. Liberal, A. M. Mahmoud and N. Engheta. Geometry-invariant resonant cavities. *Nature Communications* 7.1 (2016), 10989. DOI: 10.1038/ncomms10989.
- [87] S. Vassant, A. Archambault, F. Marquier, F. Pardo, U. Gennser, A. Cavanna, J. L. Pelouard and J. J. Greffet. Epsilon-Near-Zero Mode for Active Optoelectronic Devices. *Phys. Rev. Lett.* 109 (2012), 237401. DOI: 10.1103/PhysRevLett.109.237401.
- [88] S. Campione, I. Brener and F. Marquier. What is an epsilon-near-zero mode?: *Advanced Photonics 2015* (2015), IM4A.5. DOI: 10.1364/IPRSN.2015.IM4A.5.
- [89] V. Bruno, C. DeVault, S. Vezzoli, Z. Kudyshev, T. Huq, S. Mignuzzi, A. Jacassi, S. Saha, Y. D. Shah, S. A. Maier, D. R. S. Cumming, A. Boltasseva, M. Ferrera, M. Clerici, D. Faccio, R. Sapienza and V. M. Shalaev. Negative Refraction in Time-Varying Strongly Coupled Plasmonic-Antenna Epsilon-Near-Zero Systems. *Phys. Rev. Lett.* 124 (2020), 043902. DOI: 10.1103/PhysRevLett.124.043902.
- [90] S. Prayakarao, D. Miller, D. Courtwright, C. E. Bonner and M. A. Noginov. Non-resonant enhancement of spontaneous emission of HITC dye in metal-insulator-metal waveguides. *J. Opt. Soc. Am. B* 36.8 (2019), 2312–2316. DOI: 10.1364/JOSAB.36.002312.
- [91] M. Nyman, A. Shevchenko, I. Shavrin, Y. Ando, K. Lindfors and M. Kaivola. Large-area enhancement of far-field fluorescence intensity using planar nanostructures. *APL Photonics* 4.7 (2019), 076101. DOI: 10.1063/1.5096270.

- [92] Y. Liu, D. Wang, J. Shi, Q. Peng and Y. Li. Magnetic Tuning of Upconversion Luminescence in Lanthanide-Doped Bifunctional Nanocrystals. *Angewandte Chemie International Edition* 52.16 (2013), 4366–4369. DOI: <https://doi.org/10.1002/anie.201209884>.
- [93] Y. Wang and T. Ding. Optical tuning of plasmon-enhanced photoluminescence. *Nanoscale* 11 (2019), 10589–10594. DOI: [10.1039/C9NR03725J](https://doi.org/10.1039/C9NR03725J).
- [94] V. A. Fonseca Deichmann, V. Yakutkin, S. Balushev and L. Akcelrud. Optical Tuning of the Fluorescence Spectrum of a Pi-Conjugated Polymer through Excitation Power. *The Journal of Physical Chemistry B* 115.20 (2011), 6385–6394. DOI: [10.1021/jp111424w](https://doi.org/10.1021/jp111424w).
- [95] W. Xu, Y. Gao and M. J. Serpe. Electrochemically Color Tunable Poly(N-isopropylacrylamide) Microgel-based Etalons. *J. Mater. Chem. C* 2 (2014), 3873–3878. DOI: [10.1039/C4TC00271G](https://doi.org/10.1039/C4TC00271G).
- [96] A. Ahiabu and M. J. Serpe. Rapidly Responding pH- and Temperature-Responsive Poly (N-Isopropylacrylamide)-Based Microgels and Assemblies. *ACS Omega* 2 (2017), 1769–1777. DOI: [10.1021/acsomega.7b00103](https://doi.org/10.1021/acsomega.7b00103).
- [97] D. Ghindani, A. R. Rashed and H. Caglayan. Unveiling spontaneous emission enhancement mechanisms in metal-insulator-metal nanocavities. *Photonics Research* 9.2 (2021), 237–242. DOI: [10.1364/PRJ.411456](https://doi.org/10.1364/PRJ.411456).
- [98] S. K. Christensen, M. C. Chiappelli and R. C. Hayward. Gelation of Copolymers with Pendent Benzophenone Photo-Cross-Linkers. *Macromolecules* 45.12 (2012), 5237–5246. DOI: [10.1021/ma300784d](https://doi.org/10.1021/ma300784d).
- [99] M. E. Nash, W. M. Carroll, P. J. Foley, G. Maguire, C. O. Connell, A. V. Gorelov, S. Beloshapkin and Y. A. Rochev. Ultra-thin spin coated crosslinkable hydrogels for use in cell sheet recovery—synthesis, characterisation to application. *Soft Matter* 8 (2012), 3889–3899. DOI: [10.1039/C2SM06466A](https://doi.org/10.1039/C2SM06466A).
- [100] Y. Brasse, M. B. Müller, M. Karg, C. Kuttner, T. A. F. König and A. Fery. Magnetic and Electric Resonances in Particle-to-Film-Coupled Functional Nanostructures. *ACS applied materials and interfaces* 10.3 (2018), 3133–3141. DOI: [10.1021/acsaami.7b16941](https://doi.org/10.1021/acsaami.7b16941).
- [101] P. B. Johnson and R. W. Christy. Optical Constants of the Noble Metals. *Phys. Rev. B* 6 (1972), 4370–4379. DOI: [10.1103/PhysRevB.6.4370](https://doi.org/10.1103/PhysRevB.6.4370).

- [102] T. S. Luk, D. de Ceglia, S. Liu, G. A. Keeler, R. P. Prasankumar, M. A. Vincenti, M. Scalora, M. B. Sinclair and S. Campione. Enhanced third harmonic generation from the epsilon-near-zero modes of ultrathin films. *Applied Physics Letters* 106.15 (2015), 151103. DOI: 10.1063/1.4917457.
- [103] A. Capretti, Y. Wang, N. Engheta and L. D. Negro. Enhanced third-harmonic generation in Si-compatible epsilon-near-zero indium tin oxide nanolayers. *Opt. Lett.* 40.7 (2015), 1500–1503. DOI: 10.1364/OL.40.001500.
- [104] M. Clerici, N. Kinsey, C. DeVault, J. Kim, E. G. Carnemolla, L. Caspani, A. Shaltout, D. Faccio, V. Shalaev, A. Boltasseva and M. Ferrera. Controlling hybrid nonlinearities in transparent conducting oxides via two-colour excitation. *Nature Communications* 8.1 (2017), 15829. DOI: 10.1038/ncomms15829.
- [105] S. Campione, J. R. Wendt, G. A. Keeler and T. S. Luk. Near-Infrared Strong Coupling between Metamaterials and Epsilon-near-Zero Modes in Degenerately Doped Semiconductor Nanolayers. *ACS Photonics* 3.2 (2016), 293–297. DOI: 10.1021/acsp Photonics.5b00663.
- [106] S. Vassant, J.-P. Hugonin, F. Marquier and J.-J. Greffet. Berreman mode and epsilon near zero mode. *Opt. Express* 20.21 (2012), 23971–23977. DOI: 10.1364/OE.20.023971.
- [107] S. Campione, I. Brener and F. Marquier. Theory of epsilon-near-zero modes in ultrathin films. *Phys. Rev. B* 91.21 (2015), 121408. DOI: 10.1103/PhysRevB.91.121408.
- [108] A. C. Lesina, D. Goodwill, E. Bernier, L. Ramunno and P. Berini. On the performance of optical phased array technology for beam steering: effect of pixel limitations. *Opt. Express* 28.21 (2020), 31637–31657. DOI: 10.1364/OE.402894.
- [109] A. Howes, W. Wang, I. Kravchenko and J. Valentine. Dynamic transmission control based on all-dielectric Huygens metasurfaces. *Optica* 5.7 (2018), 787–792. DOI: 10.1364/OPTICA.5.000787.
- [110] G. T. Papadakis and H. A. Atwater. Field-effect induced tunability in hyperbolic metamaterials. *Phys. Rev. B* 92 (2015), 184101. DOI: 10.1103/PhysRevB.92.184101.

- [111] P. B. Johnson and R. W. Christy. Optical Constants of the Noble Metals. *Phys. Rev. B* 6 (1972), 4370–4379. DOI: 10.1103/PhysRevB.6.4370.
- [112] A. Benz, S. Campione, S. Liu, I. Montano, J. F. Klem, A. Allerman, J. R. Wendt, M. B. Sinclair, F. Capolino and I. Brener. Strong coupling in the sub-wavelength limit using metamaterial nanocavities. *Nature Communications* 4.1 (2013), 1–8. DOI: 10.1038/ncomms3882.
- [113] J. Park, J.-H. Kang, X. Liu and M. L. Brongersma. Electrically Tunable Epsilon-Near-Zero (ENZ) Metafilm Absorbers. *Scientific Reports* 5.1 (2015), 15754. DOI: 10.1038/srep15754.
- [114] E. Feigenbaum, K. Diest and H. A. Atwater. Unity-Order Index Change in Transparent Conducting Oxides at Visible Frequencies. *Nano Letters* 10.6 (2010), 2111–2116. DOI: 10.1021/nl1006307.
- [115] C. Ciuti, G. Bastard and I. Carusotto. Quantum vacuum properties of the intersubband cavity polariton field. *Phys. Rev. B* 72 (2005), 115303. DOI: 10.1103/PhysRevB.72.115303.
- [116] L. Han, H. Ding, T. Huang, X. Wu, B. Chen, K. Ren and S. Fu. Broadband Optical Reflection Modulator in Indium-Tin-Oxide-Filled Hybrid Plasmonic Waveguide with High Modulation Depth. *Plasmonics* 13.4 (2018), 1309–1314. DOI: 10.1007/s11468-017-0634-x.
- [117] K. Manukyan, M. Z. Alam, C. Liu, K. Pang, H. Song, Z. Zhao, M. Tur, R. W. Boyd and A. E. Willner. Dependence of the coupling properties between a plasmonic antenna array and a sub-wavelength epsilon-near-zero film on structural and material parameters. *Applied Physics Letters* 118.24 (2021), 241102. DOI: 10.1063/5.0042599.
- [118] X. Duan, F. Zhang, Z. Qian, H. Hao, L. Shan, Q. Gong and Y. Gu. Accumulation and directionality of large spontaneous emission enabled by epsilon-near-zero film. *Opt. Express* 27.5 (2019), 7426–7434. DOI: 10.1364/OE.27.007426.
- [119] C. T. DeVault, V. A. Zenin, A. Pors, K. Chaudhuri, J. Kim, A. Boltasseva, V. M. ShalaeV and S. I. Bozhevolnyi. Suppression of near-field coupling in plasmonic antennas on epsilon-near-zero substrates. *Optica* 5.12 (2018), 1557–1563. DOI: 10.1364/OPTICA.5.001557.

- [120] M. Habib, D. Briukhanova, N. Das, B. C. Yildiz and H. Caglayan. Controlling the plasmon resonance via epsilon-near-zero multilayer metamaterials. *Nanophotonics* 9.11 (2020), 3637–3644. DOI: doi : 10 . 1515 / nanoph - 2020 - 0245.
- [121] D. Ghindani, T. Pihlava and H. Caglayan. Suppressing the spectral shift of a polarization-independent nanostructure with multiple resonances. *Opt. Lett.* 47.21 (2022), 5553–5556. DOI: 10 . 1364 / OL . 472360.

A APPENDIX

The details of equipment and techniques that have been extensively used for device fabrication are discussed in the following sections.

A.1 Electron beam evaporator

The electron beam evaporator (e-beam evaporator) is a technique for making thin films in a high vacuum with high quality, and it was utilized in all the works for the deposition of metals (metallization). The system consists of crucibles with six different materials gold (Au), titanium (Ti), platinum (Pt), nickel (Ni), Silver (Ag), and Chromium (Cr); out of these materials, mostly used materials for this thesis were Au and Ag. The e-beam evaporation method was used because the e-beam evaporator gives the possibility to evaporate and deposit the materials at very high deposition rates. Also, the film deposition by an e-beam evaporator is better than the other techniques, like thermal evaporation, as it maintains the purity of the source material. In this process, the current is passed through a tungsten filament which gives rise to Joule heating and electron emission. To accelerate these free electrons in the direction of the crucible, which contains the desired material, a high voltage is applied between the filament and the hearth. The electrons make the focused beam because of a strong magnetic field. Additionally, the focused electron beam transfers its energy to the desired material to be deposited, which causes the sublimation and evaporation of metal and its deposition on the substrate.

A.2 Scanning electron microscope

The scanning electron microscope (SEM) images presented in this thesis were all captured by using Zeiss Ultra-55 SEM. An SEM is a type of electron microscope in

which the incident-focused electron beam with high energy scans over the sample's surface and produces high-resolution images. These images give information about the texture of the surface and about the geometry of patterns created on the substrate. The fundamental working principle of SEM is based on the interaction between the sample (substrate) and an incident electron beam. When the accelerated electrons incident onto the solid substrate, they start to decelerate by dissipating their energy in producing various signals through electron-substrate interaction. The generated signals consist of back-scattered and secondary electrons. The secondary electrons are detected by a secondary electron detector and are very useful in creating a morphological image of the sample. On the other hand, back-scattered electrons are valuable to find out the composition. Some SEMs can achieve resolutions better than 1 nanometer. To capture the images from electrically insulating samples, the samples must be coated with conducting layers such as carbon, conducting polymer, and a thin layer of metals to overcome the charging effect due to charge build-up.

A.3 Electron beam lithography

The Raith ElphyPLUS electron beam lithography (EBL) was used to fabricate the high-resolution gold nanostructures presented in Publications III and IV. The State-of-the-art EBL is a precise (sub-10 nm resolution) and mature technology that exhibits excellent control of the placement of structures. It uses an electron beam instead of a visible or UV light beam in the optical lithography process. In EBL, an organic film (resist layer) is directly patterned by electronically moving the highly-focused electron beam on the resist-coated substrate. The system mainly consists of an electron gun to supply electrons, the column that shapes and focuses the beam with the help of an objective and condenser lens, and a vibration-isolated mechanical stage that position the substrate under a focused e-beam. The EBL is a direct-write (writing without any mask) technology that can create structures of dimensions of sub-micrometers down to a few nanometers because electrons focus much more tightly than light. An EBL system uses hardware similar to SEM to guide a focused electron beam of nanometer size to make the desired structure on the resist layer. The desired pattern designed with suitable CAD tools is fed into the system. With all the merits mentioned above and the capabilities of EBL, the demerit is that it is a slow and expensive process because it produces the pattern in a 'serial' manner,

making it a slow process compared to optical lithography.

B APPENDIX

B.1 Other publication

R. Dhama, A. Panahpour, T. Pihlava, **D. Ghindani** and H. Caglayan. All-optical switching based on plasmon-induced Enhancement of Index of Refraction. Nature Communications 13.1 (2022), 3114.

PUBLICATIONS

PUBLICATION

I

**Unveiling spontaneous emission enhancement mechanisms in
metal-insulator-metal nanocavities**

D. Ghindani, A. R. Rashed and H. Caglayan

Photonics Research 9.2 (2021), 237–242

DOI: 10.1364/PRJ.411456

Publication reprinted with the permission of the copyright holders

PHOTONICS Research

Unveiling spontaneous emission enhancement mechanisms in metal–insulator–metal nanocavities

DIPA GHINDANI,  ALIREZA R. RASHED,  AND HUMEYRA CAGLAYAN* 

Faculty of Engineering and Natural Sciences, Photonics, Tampere University, 33720 Tampere, Finland

*Corresponding author: humeyra.caglayan@tuni.fi

Received 1 October 2020; revised 7 December 2020; accepted 19 December 2020; posted 21 December 2020 (Doc. ID 411456); published 27 January 2021

Recent advances in the development of a nanocavity based on a metal–insulator–metal (MIM) structure have provided a great opportunity to enhance the performance of photonic devices. However, the underlying physics behind the emission enhancement obtained from such cavities is under debate. Here, in this work, we designed and investigated MIM nanocavities to reveal the mechanisms for the observed 260-fold photoluminescence enhancement from LDS 798 fluorescent dye. This study provides a pathway to engineer the emission properties of an emitter not only through the enhancement of the Purcell factor but mainly through enhancement of the excitation rate. Our numerical simulations support the experimentally acquired results. We believe an MIM cavity and dye-based hybrid system design based on the revealed enhancement process and structural simplicity, will provide more efficient, lithography free, and low-cost advanced nanoscale devices. © 2021 Chinese Laser Press

<https://doi.org/10.1364/PRJ.411456>

1. INTRODUCTION

Tailoring the emission property of an emitter is of great interest in terms of understanding the fundamental physics as well as the application prospects. In particular, the coherent interaction of an atom with the electromagnetic field is an ideal testbed to study many fundamental aspects of quantum mechanics [1]. From an application point of view, the enhancement of spontaneous emission (SE) is vital because it can enable highly efficient light-emitting devices, low-threshold lasers [2,3], and highly efficient single-photon sources [4,5]. The emission of an emitter can be enhanced by properly tailoring its photonic environment. The environment can enhance the emission either by (i) increasing the spontaneous emission rate (i.e., Purcell enhancement), (ii) increasing the excitation rate intensity, or (iii) modifying the radiation pattern [6–8]. Among these three factors, local excitation field intensity modifies the excitation rate, while the modification in the radiative decay channels of an emitter enhances the Purcell factor. There have been several studies reported on the SE enhancement of an emitter predominantly focusing on Purcell enhancement [9,10]. These studies mainly used a photonic crystal cavity [11,12], a waveguide, and metallic structures such as metal thin film [13], grating [14], nanoantennas [15,16], and nanoapertures [17]. In all these approaches, the photonic environment is tailored to achieve the fluorescence enhancement. An efficient modification in the photonic environment of an emitter can be achieved by integrating it into an optical cavity

with a high-quality factor (Q -factor) and a low-mode profile. The photonic crystal (PC) cavity is an example of a cavity that supports high Q -factor resonance [11]. However, the minimum possible mode volume offered by the PC cavity is limited by the diffraction limit [18]. In addition, the integration of a narrow-band emitter with a high Q -factor cavity resonance requires intensive nanofabrication and lacks scalability. On the other hand, plasmonic nanostructures offer a low-mode volume at the plasmon resonance frequency [19]. However, due to the metallic losses, they suffer from a low Q -factor. In addition, the integration process for plasmonics nanostructures with deposited emitters in large areas is limited by their fabrication complexity. This restricts the translation of this approach for integrated photonics.

Metal–insulator–metal (MIM) structures, which emerged in recent years as high Q -factor Fabry–Perot resonators, are highly versatile to modify the properties of an emitter [20]. The ability to confine the light into the subwavelength-sized dielectric spacer is a remarkable property of an MIM cavity that has been used to demonstrate many disruptive applications in a plethora of fields from super absorption to high-resolution spatial color filters [21–23]. Among the diverse applications, the spontaneous emission rate enhancement has recently attracted the attention of the scientific community [24,25]. The fabrication simplicity and reproducibility of MIM structures are the major advantages compared to plasmonic nanocavity and PC cavity based approaches.

Prayakarao *et al.* studied the effect of the dielectric thickness of the MIM cavities on the SE rate enhancement [24]. In their study, they showed an emission enhancement of HITC dye molecules at the nonresonant wavelength of MIM cavities. On the other hand, Nyman *et al.* reported far-field fluorescence enhancement at the resonant wavelength of an IR780 dye embedded in an MIM structure [25]. They showed that the achieved enhanced emission is attributed to both the excitation rate enhancement and the Purcell factor enhancement. However, since the Stokes shift in these studied dyes is very low, the cavity resonance wavelength of the MIM overlaps efficiently with both the absorption and emission spectra of the dye molecules. In such experimental circumstances, the participation of each phenomenon in the emission enhancement process is not clearly distinguishable. These recent studies presented MIM cavities as potential candidates for SE enhancement due to their outstanding optical properties. Nevertheless, the exact mechanisms for the enhanced SE were not revealed.

We performed systematic theoretical and experimental studies to investigate underlying mechanisms related to the observed enhanced SE rate in MIM cavities. In this work, we use a silver (Ag) based MIM cavity [Ag–polymethylmethacrylate (PMMA)–Ag] to enhance the spontaneous emission rate of LDS 798 dye molecules. We observed enhancement in the photoluminescence (PL) intensity along with a change in the fluorescent lifetime components. In the studied dye-integrated hybrid system, two main mechanisms play a role in the emission enhancement process: Purcell effect enhancement due to confinement of the electromagnetic field between the two metallic films and excitation rate enhancement due to the strong cavity mode. A simultaneous overlap of the absorption and emission spectra of LDS 798 dye molecules with the cavity resonance of the designed MIM nanocavity provides the opportunity to exploit both processes to enhance the emission of hybrid systems with the highest efficiency. We show the role of the excitation rate enhancement to achieve an intensified emission in such a design. We believe our approach to the design of dye-integrated hybrid MIM systems opens the way to realize more efficient, lithography-free, and low-cost advanced nanoscale devices.

2. RESULTS AND DISCUSSION

The schematic of the fabricated MIM cavity is shown in Fig. 1(a), where the thickness of top and bottom metallic layers is 35 and 150 nm, respectively. Ag has been used for the metal layers due to its excellent plasmonic property and low losses. We deposited Ag layers using an e-beam evaporator and confirmed each layer's thickness using a profilometer. PMMA was spincoated as a dielectric layer and the thickness of the dielectric layer was varied to tune the cavity resonance. The thickness of the dielectric layer was optimized using numerical simulation (Lumerical FDTD Solutions) based on finite-difference time-domain (FDTD) method. In simulations, the periodic boundary conditions were applied in the x axis and y axis while PML (perfectly matched layer) was used in z axis. A plane wave was launched in the z axis to excite the resonance modes. The simulated reflection results for different thicknesses of the dielectric (PMMA) layers are shown in

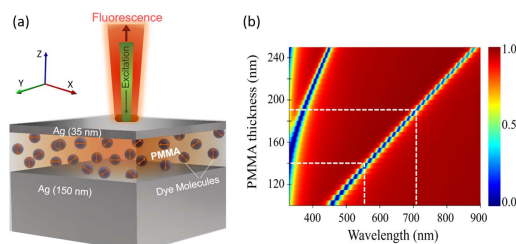


Fig. 1. (a) Schematic of MIM (Ag–PMMA + LDS 798 dye–Ag) cavity. (b) Simulated reflection result for different thicknesses of dielectric layer. White dashed lines show resonance position of both cavities with thicknesses of 140 nm and 190 nm.

Fig. 1(b). Based on these results, 140 nm and 190 nm, which correspond to the cavity resonance wavelengths of 567 and 710 nm, were chosen as the dielectric layer thicknesses to match the MIM cavity resonance with the absorption and emission spectra of LDS 798 dye molecules. We call the MIMs with PMMA thicknesses 140 nm and 190 nm MIM-I and MIM-II, respectively, in the rest of this paper. Another resonance that is blue-shifted with respect to the main resonance of the nanocavity is evident in these simulation results.

Figures 2(a) and 2(b) show the experimentally recorded absorption (black solid line) and emission spectra (red solid line) of the LDS 798 dye molecules, which confirms the absorption and emission peaks at 567 nm and 670 nm, respectively. The experimentally recorded reflection spectra for MIM-I and MIM-II are shown in Fig. 2 (blue solid line) and have good agreement with simulated reflectance results [Fig. 1(b)]. From Figs. 2(a) and 2(b), it is important to note that the resonance of the MIM-I cavity has a strong overlap with the absorption spectrum, whereas the resonance of the MIM-II cavity overlaps with the emission spectrum of the dye, but barely overlaps with the absorption spectrum.

To elucidate the effect of strong field confinement on the emission property of LDS 798, we experimentally recorded the intensity counts of the fluorescent dye molecules using PL measurement with a 532 nm excitation source. Figures 3(a) and 3(b) show PL counts for the dye integrated with MIM-I and MIM-II, respectively. From Fig. 3(a), it is evident that the incorporation of the dye molecules with the MIM-I cavity exhibits remarkable emission enhancement. We observed a 260-fold emission enhancement for the dye molecules integrated with MIM-I and only a 3-fold emission enhancement for MIM-II. In the case of MIM-I, the higher multifold enhancement can be attributed to an unequal combination of the Purcell effect enhancement and enhancement of the local excitation field, because the resonance band of the MIM-I structure overlaps strongly with the absorption spectrum and partially with the emission spectrum of the LDS 798 dye molecules. On the other hand, for MIM-II, excitation rate enhancement and Purcell factor enhancement work as two weak gateways to modify the spontaneous emission rate of the hybrid system.

Furthermore, the transient PL decay traces of the dye molecules were measured through time-resolved fluorescence

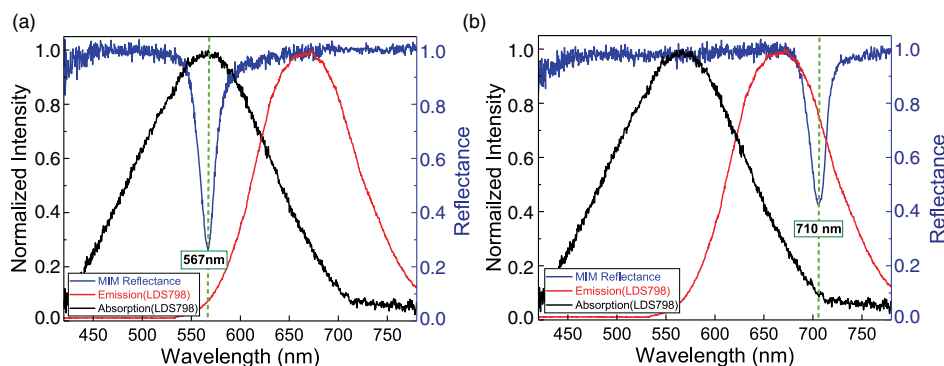


Fig. 2. Measured reflectance spectra of (a) MIM-I and (b) MIM-II cavities. The absorption and emission spectra of LDS 798 dye molecules are presented as black and red curves in both panels, respectively. The reflectance band of MIM-I cavity overlaps with the absorption peak and the emission tail of fluorescent dye, while the reflectance band of MIM-II overlaps with the emission of the dye and barely with absorption of dye.

spectroscopy. The experimentally recorded transient decay dynamics is shown in Figs. 3(c) and 3(d). We have acquired the PL lifetime of the LDS 798 dye integrated with MIM cavities I and II, and embedded them in PMMA as a reference sample. We have used a bi-exponential function to fit kinetics of the reference and main samples, as shown in Table 1. The presence of LDS 798 molecules in a rigid matrix like PMMA hinders the large-amplitude motion and intermolecular beatings of the excited molecules. Moreover, in such a dense environment, the probability of the aggregation for the monomers of the dye increases. These effects can result in two fluorescent lifetime

Table 1. Time-Resolved Fluorescence Spectroscopy Results for the MIM-I and MIM-II Nanocavities and LDS 798 Dye Molecules Embedded in PMMA^a

Sample Table	τ_{Short} (ns)	A_{Short}	τ_{Long} (ns)	A_{Long}
LDS 798	1.144	41%	2.408	59%
MIM-I	1.074	75%	3.691	25%
MIM-II	0.990	33%	2.404	67%

^aA bi-exponential function is used to fit kinetics of the reference and main samples. A_{Short} and A_{Long} are the amplitudes of the τ_{Short} and τ_{Long} components in percentage, respectively.

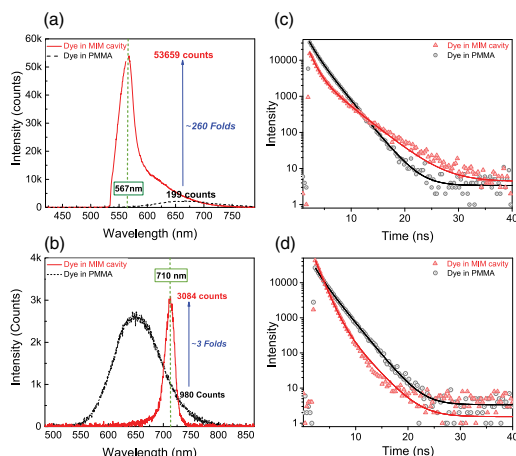


Fig. 3. Experimentally recorded steady-state PL spectra of LDS 798 dye molecules embedded in cavities (red solid lines): (a) MIM-I cavity and (b) MIM-II cavity. The recorded emission of embedded dye molecules in PMMA as a reference sample is shown as a black dotted line. Time-resolved fluorescence spectroscopy results of embedded dye molecules in the MIM cavities (red triangles): (c) MIM-I and (d) MIM-II. The recorded fluorescent lifetime of embedded dye in PMMA as a reference sample is shown as a black dotted line.

components rather than a single component, which is the case for the dissolved LDS dye molecules in low viscous solvents [26,27]. The applied bi-exponential function to fit PL kinetics of dye molecules in the reference sample (black circles) results in two characteristic lifetime components of $\tau_1 \approx 1.144 \pm 0.009$ ns and $\tau_2 \approx 2.408 \pm 0.009$ ns, where the first component characterizes the fast decay rate, while the latter represents the slow decay process. The incorporation of the dye molecule with the MIM-I cavity induces a reduction in the fast decay component ($\tau_1 \approx 1.074 \pm 0.002$ ns), but the slow decay component ($\tau_2 \approx 3.691 \pm 0.016$ ns) gets elongated, as shown in Fig. 3(c) (red triangles).

The reduction in the fast decay component can be attributed to the emission rate enhancement due to the Purcell effect. However, the slower component increases due to leakage radiation from the MIM-I cavity. Since the cavity resonance of MIM-I (at 567 nm) is far from the emission peak [670 nm, Fig. 2(a) red solid line], the part of the emission that does not couple with the MIM-I cavity results in slow leakage field. This leakage occurs due to the thin metallic top layer (35 nm), which is unable to effectively confine the emission of the non-resonant dye molecules embedded inside the cavity in the off-resonant spectral region. In the case of MIM-II, the characteristic lifetime components are $\tau_1 \approx 0.99 \pm 0.013$ ns and $\tau_2 \approx 2.404 \pm 0.009$ ns. The reduction in τ_1 arises due to the Purcell factor enhancement as the emitted radiation of

dye molecules resonantly couples with the MIM-II cavity. On the other hand, the τ_2 decay component remains almost unchanged, which depicts nonresonant emission from uncoupled dye molecules. Comparison of the fast components of the excited dye molecules in both cavities reveals an almost similar coupling strength. This happens even though the spectral overlaps between the emission of the dye molecules and the resonance bands of the two nanocavities are not similar. These results prove the occurrence of the Purcell enhancement in the MIM-I and MIM-II cavities, which leads to a similar intensified emission for both of the nanocavities through this enhancement gateway. Therefore, the excitation rate enhancement as an extra emission enhancement channel works as the main gateway to achieve a much more intensified emission only in the MIM-I cavity.

Consider that the absorption of the metallic layers can influence the emission enhancement process of the excited dye molecules. Moreover, the occurrence of nonradiative quenching mechanisms such as nanosurface energy transfer (NSET) [28] and resonance energy transfer (RET) [29] between the dye molecules and probable roughness of the metallic films is possible. In addition, the resonance energy transfer between the monomers and multimers of the dye molecules is probable [30]. However, as the time-resolved fluorescence spectroscopy results for both nanocavities do not depict extremely short lifetime components, nonradiative loss channels evidently are not influential in the emission enhancement process. This is due to the fact that the evaporated metal layers are smooth enough and a small portion of the excited dye molecules are located in the vicinity of the metallic films. Therefore, in our case, the influence of the loss mechanisms on the spontaneous decay rate enhancement is negligible.

To unveil the underlying physics for multifold enhancement, we performed numerical simulations to calculate the electric field confined inside nanocavities. Figures 4(a) and 4(b) show the electric field contour plot of MIM nanocavities with a strong electric field confinement in the dielectric region (PMMA) at cavity resonance wavelengths; i.e., 567 nm and 710 nm, respectively. Thus, one can expect that the incorporation of dye molecules with the designed MIM cavities can lead to fluorescence enhancement.

In this study, the resonance of the MIM-I cavity overlaps partially with emission spectrum while efficiently with the absorption band of the dye, as shown in Fig. 2(a), that results in an increase in fluorescence emission via two gateways: mainly by enhancing the local field intensity, which leads to a stronger population of the excited state, and slightly by increasing the spontaneous emission rate of emitter (i.e., the Purcell enhancement). Further, to emphasize our reasoning, we numerically calculated the Purcell factor of our integrated devices, as shown in Figs. 4(c) and 4(d) for the MIM-I and MIM-II cavities, respectively. For the Purcell factor calculations, we used Lumerical FDTD Solutions software, where a dipole source is used to emulate the photoexcited dye molecule. The dipole source is located in the middle of the dielectric layer of the MIM structure. The orientation of the dipole is varied from the x to y direction and the Purcell factor is averaged to capture the ensemble feature of the dye molecules that are randomly

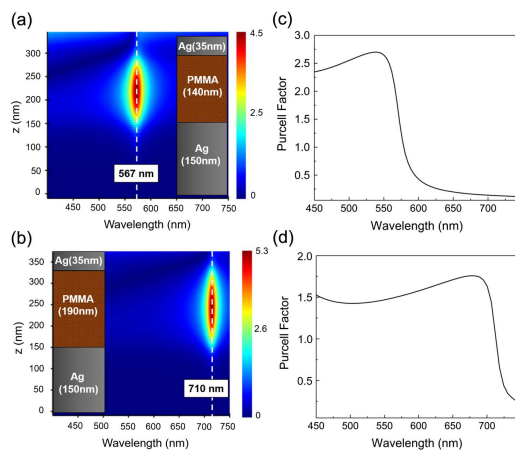


Fig. 4. Simulation results for the electric field contour plot in the two nanocavities: (a) MIM-I and (b) MIM-II. The insets in panels (a) and (b) show the schematics of the MIM-I and MIM-II designs, respectively. The Purcell factor calculation for the two cavities: (c) MIM-I and (d) MIM-II. The higher mode profile describes the lower Purcell factor of the MIM-II cavity with respect to that of MIM-I.

oriented in the x - y plane. The calculated Purcell factor for MIM-I is higher than that of MIM-II. This can be explained based on the lower mode profile of MIM-I compared to MIM-II, due to the thinner dielectric layer. As the leakage occurs in the off-resonant spectral region (above 580 nm), the observed leakage cannot influence the calculated Purcell factor for the on-resonance spectral region (540–580 nm) of the MIM-I cavity. The simulation result in Fig. 4(c) shows that, at the resonance wavelength, the Purcell factor has a value of 1.8. Such a small value of Purcell factor supports the fact that for MIM-I, the major contribution for the 260-fold enhancement is mainly coming from the excitation rate enhancement. The calculated Purcell factor for the MIM-II cavity is 1.2. This proves that, for this cavity, the contribution of the excitation rate enhancement in the acquired enhanced emission is not considerable. According to the presented approach in previous works [31,32], one can obtain the Purcell factor of a quantum emitter located inside a resonator by dividing the uncoupled emitters' lifetime by that of the coupled emitter in the cavity. Subsequently, we extracted the Purcell factor from measured lifetime results for the MIM-I and MIM-II cavities as 1.2 and 1.1, respectively. These results show adequate agreement with the calculated Purcell factors.

3. CONCLUSION

In conclusion, we have shown a fluorescence enhancement of LDS 798 dye molecules by integrating them with an MIM cavity. We unveiled the mechanisms behind the emission enhancement process in the MIM nanocavities integrated with quantum emitters. This is performed by designing two different MIM cavities. The absorption spectrum of the dye overlaps

efficiently with the resonance of MIM-I, but barely with the resonance of MIM-II. Our comprehensive study shows that the dye integrated with MIM-II shows only a 3-fold enhancement. On the other hand, the MIM cavity that is optimized to have a resonance peak overlapping with the absorption of the dye exhibits an exceptionally high enhancement of 260-fold in the photoluminescence intensity. This arises as a combination of the Purcell effect and the excitation rate enhancement. Hence, according to our findings, the observed remarkable high emission enhancement for quantum emitters embedded in MIM nanocavities is attributed mainly to the excitation rate enhancement rather than the Purcell enhancement.

The MIM-nanocavity-based approach can be used to engineer the emission properties of an emitter by using enhanced light-matter interactions that would potentially lead to the development of efficient light-emitting devices or an enhanced energy transfer. Because MIM nanocavities possess multiple cavity modes with a high quality factor, this creates an opportunity to overlap the absorption band of a quantum emitter with the mode at the lower wavelength of the spectrum, while the emission spectrum can be overlapped with the mode at the higher wavelength. As a result, one can achieve a higher spontaneous emission enhancement for the incorporated quantum emitter inside the nanocavity. Another approach might be to integrate the dye molecule with an MIM with metasurfaces. In this way, it is possible to develop highly efficient, multifunctional integrated photonic devices where emission properties can be actively or passively tuned by changing the polarization of incident light and geometrical parameters of the metasurface. Thus, we believe our findings allow the design of low-cost, effective nanophotonic devices with enhanced functionalities.

Funding. Academy of Finland (320165 Flagship Programme PREIN).

Acknowledgment. The authors acknowledge the support of the Academy of Finland's Flagship Programme (PREIN) and The Finnish National Agency for Education through an EDUFi Fellowship for author Dipa Ghindani. The authors also thank Jussi Toppari and Gerit Groenhof for scientific discussions of the results.

Disclosures. The authors declare no conflicts of interest.

REFERENCES

- H. Walther, B. T. H. Varcoe, B.-G. Englert, and T. Becker, "Cavity quantum electrodynamics," *Rep. Prog. Phys.* **69**, 1325–1382 (2006).
- M. A. Noginov, G. Zhu, A. M. Belgrave, R. Bakker, V. M. Shalae, E. E. Narimanov, S. Stout, E. Herz, T. Suteewong, and U. Wiesner, "Demonstration of a spaser-based nanolaser," *Nature* **460**, 1110–1112 (2009).
- Q. Zhang, G. Li, X. Liu, F. Qian, Y. Li, T. C. Sum, C. M. Lieber, and Q. Xiong, "A room temperature low-threshold ultraviolet plasmonic nanolaser," *Nat. Commun.* **5**, 4953 (2014).
- A. Jeantet, Y. Chassagneux, C. Raynaud, P. Roussignol, J. S. Lauret, B. Besga, J. Estève, J. Reichel, and C. Voisin, "Widely tunable single-photon source from a carbon nanotube in the Purcell regime," *Phys. Rev. Lett.* **116**, 247402 (2016).
- J. Claudon, J. Bleuse, N. S. Malik, M. Bazin, P. Jaffrennou, N. Gregersen, C. Sauvan, P. Lalanne, and J.-M. Gérard, "A highly efficient single-photon source based on a quantum dot in a photonic nanowire," *Nat. Photonics* **4**, 174–177 (2010).
- W. L. Barnes, "Fluorescence near interfaces: the role of photonic mode density," *J. Mod. Opt.* **45**, 661–699 (1998).
- J. R. Lakowicz, "Radiative decay engineering 5: metal-enhanced fluorescence and plasmon emission," *Anal. Biochem.* **337**, 171–194 (2005).
- E. Fort and S. Grésillon, "Surface enhanced fluorescence," *J. Phys. D* **41**, 013001 (2007).
- A. Neogi, C.-W. Lee, H. O. Everitt, T. Kuroda, A. Tackeuchi, and E. Yablonovitch, "Enhancement of spontaneous recombination rate in a quantum well by resonant surface plasmon coupling," *Phys. Rev. B* **66**, 153305 (2002).
- K. Okamoto, I. Niki, A. Shvartser, Y. Narukawa, T. Mukai, and A. Scherer, "Surface-plasmon-enhanced light emitters based on InGaP quantum wells," *Nat. Mater.* **3**, 601–605 (2004).
- S. Ogawa, M. Imada, S. Yoshimoto, M. Okano, and S. Noda, "Control of light emission by 3D photonic crystals," *Science* **305**, 227–229 (2004).
- K. Aoki, D. Guimard, M. Nishioka, M. Nomura, S. Iwamoto, and Y. Arakawa, "Coupling of quantum-dot light emission with a three-dimensional photonic-crystal nanocavity," *Nat. Photonics* **2**, 688–692 (2008).
- Y.-J. Hung, I. I. Smolyaninov, C. C. Davis, and H.-C. Wu, "Fluorescence enhancement by surface gratings," *Opt. Express* **14**, 10825–10830 (2006).
- Y. Liu and S. Blair, "Fluorescence enhancement from an array of sub-wavelength metal apertures," *Opt. Lett.* **28**, 507–509 (2003).
- S. Kühn, U. Håkanson, L. Rogobete, and V. Sandoghdar, "Enhancement of single-molecule fluorescence using a gold nanoparticle as an optical nanoantenna," *Phys. Rev. Lett.* **97**, 017402 (2006).
- O. G. Tovmachenko, C. Graf, D. J. van den Heuvel, A. van Blaaderen, and H. C. Gerritsen, "Fluorescence enhancement by metal-core/silica-shell nanoparticles," *Adv. Mater.* **18**, 91–95 (2006).
- H. Rigneault, J. Capoulade, J. Dintinger, J. Wenger, N. Bonod, E. Popov, T. W. Ebbesen, and P.-F. Lenne, "Enhancement of single-molecule fluorescence detection in subwavelength apertures," *Phys. Rev. Lett.* **95**, 117401 (2005).
- M. Pelton, "Modified spontaneous emission in nanophotonic structures," *Nat. Photonics* **9**, 427–435 (2015).
- N. J. Halas, S. Lal, W.-S. Chang, S. Link, and P. Nordlander, "Plasmons in strongly coupled metallic nanostructures," *Chem. Rev.* **111**, 3913–3961 (2011).
- Y. Kurokawa and H. T. Miyazaki, "Metal-insulator-metal plasmon nanocavities: analysis of optical properties," *Phys. Rev. B* **75**, 035411 (2007).
- F. Ding, L. Mo, J. Zhu, and S. He, "Lithography-free, broadband, omnidirectional, and polarization-insensitive thin optical absorber," *Appl. Phys. Lett.* **106**, 061108 (2015).
- Z. Li, S. Butun, and K. Aydin, "Large-area, lithography-free super absorbers and color filters at visible frequencies using ultrathin metallic films," *ACS Photon.* **2**, 183–188 (2015).
- A. Ghobadi, H. Hajian, A. R. Rashed, B. Butun, and E. Ozbay, "Tuning the metal filling fraction in metal-insulator-metal ultra-broadband perfect absorbers to maximize the absorption bandwidth," *Photon. Res.* **6**, 168–176 (2018).
- S. Prayakarao, D. Miller, D. Courtwright, C. E. Bonner, and M. A. Noginov, "Non-resonant enhancement of spontaneous emission of HITC dye in metal-insulator-metal waveguides," *J. Opt. Soc. Am. B* **36**, 2312–2316 (2019).
- M. Nyman, A. Shevchenko, I. Shavrin, Y. Ando, K. Lindfors, and M. Kaivola, "Large-area enhancement of far-field fluorescence intensity using planar nanostructures," *APL Photon.* **4**, 076101 (2019).
- A. R. Rashed, M. Habib, N. Das, E. Ozbay, and H. Caglayan, "Plasmon-modulated photoluminescence enhancement in hybrid plasmonic nano-antennas," *New J. Phys.* **22**, 093033 (2020).
- R. Fan, Y. Xia, and D. Chen, "Solid state dye lasers based on LDS 698 doped in modified polymethyl methacrylate," *Opt. Express* **16**, 9804–9810 (2008).
- C. S. Yun, A. Javier, T. Jennings, M. Fisher, S. Hira, S. Peterson, B. Hopkins, N. O. Reich, and G. F. Strouse, "Nanometal surface energy transfer in optical rulers, breaking the FRET barrier," *J. Am. Chem. Soc.* **127**, 3115–3119 (2005).



29. G.-C. Li, Q. Zhang, S. A. Maier, and D. Lei, "Plasmonic particle-on-film nanocavities: a versatile platform for plasmon-enhanced spectroscopy and photochemistry," *Nanophotonics* **7**, 1865–1889 (2018).
30. A. B. Serrano-Montes, J. Langer, M. Henriksen-Lacey, D. Jimenez de Aberasturi, D. M. Solís, J. M. Taboada, F. Obelleiro, K. Sentosun, S. Bals, A. Bekdemir, F. Stellacci, and L. M. Liz-Marzán, "Gold nanostar-coated polystyrene beads as multifunctional nanoprobes for SERS bioimaging," *J. Phys. Chem. C* **120**, 20860–20868 (2016).
31. T. B. Hoang, G. M. Akselrod, C. Argyropoulos, J. Huang, D. R. Smith, and M. H. Mikkelsen, "Ultrafast spontaneous emission source using plasmonic nanoantennas," *Nat. Commun.* **6**, 7788 (2015).
32. K. L. Tsakmakidis, R. W. Boyd, E. Yablonovitch, and X. Zhang, "Large spontaneous-emission enhancements in metallic nanostructures: towards LEDs faster than lasers," *Opt. Express* **24**, 17916–17927 (2016).

PUBLICATION

II

Humidity-Controlled Tunable Emission in a Dye-Incorporated Metal-Hydrogel-Metal Cavity

D. Ghindani, I. Issah, S. Chervinskii, M. Lahikainen, K. Kuntze, A. Priimagi and
H. Caglayan

ACS Photonics 9.7 (2022), 2287–2294

DOI: 10.1021/acsp Photonics.2c00202

Publication reprinted with the permission of the copyright holders

Humidity-Controlled Tunable Emission in a Dye-Incorporated Metal–Hydrogel–Metal Cavity

Dipa Ghindani, Ibrahim Issah, Semyon Chervinskii, Markus Lahikainen, Kim Kuntze, Arri Priimagi, and Humeyra Caglayan*



Cite This: <https://doi.org/10.1021/acsphotonics.2c00202>



Read Online

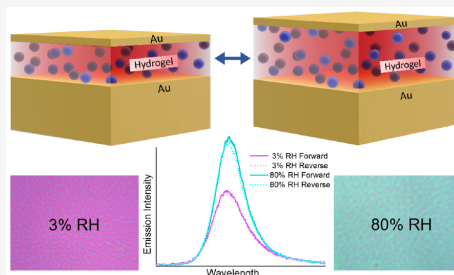
ACCESS |

Metrics & More

Article Recommendations

ABSTRACT: Actively controllable photoluminescence is potent for a wide variety of applications from biosensing and imaging to optoelectronic components. Traditionally, methods to achieve active emission control are limited due to complex fabrication processes or irreversible tuning. Here, we demonstrate active emission tuning, achieved by changing the ambient humidity in a fluorescent dye-containing hydrogel integrated into a metal–insulator–metal (MIM) system. Altering the overlapping region of the MIM cavity resonance and the absorption and emission spectra of the dye used is the underlying principle to achieving tunability of the emission. We first verify this by passive tuning of cavity resonance and further experimentally demonstrate active tuning in both air and aqueous environments. The proposed approach is reversible, easy to integrate, and spectrally scalable, thus providing opportunities for developing tunable photonic devices.

KEYWORDS: metal–insulator–metal system, hydrogels, fluorescent dye, humidity, tunable emission, stimuli-responsive materials



INTRODUCTION

Manipulating the optical properties of an emitter is of paramount importance for developing efficient light sources for advanced nanophotonic devices,^{1,2} fluorescence microscopy,³ and various optoelectronic applications.⁴ Over the past decades, numerous efforts have been made to control the emission properties of organic dye molecules, owing to their high photoluminescence (PL) quantum yield and broadband emission,⁵ paving the way for new solutions for photonic devices such as LEDs,⁶ lasers,⁷ and single-photon sources.⁸ To improve the efficiency and functionalities of the photonic devices, it is highly desirable to control and enhance the emission properties of the photonic structures. In addition, a facile, real-time, reversible, and actively tunable luminescence system is of great importance, as it serves as the basis for next-generation photonic elements. Furthermore, on-demand control of the emission will enable broadband sensing and full-color display devices. To date, plasmonic⁹ and dielectric cavities^{10,11} are routinely utilized to boost the PL signals by increasing the local density of photonic states^{12,13} around the emitter. For instance, thin metallic films and plasmonic nanoantennae tightly confine the electromagnetic field into a small volume due to plasmonic resonance. Similarly, high-index dielectric nanostructures, such as 1D gratings,¹⁴ 2D photonic crystals,^{15,16} and dielectric resonators,^{17,18} localize the electromagnetic fields by Mie-resonances. Although these

approaches have shown notable PL enhancement, they bring along some limitations. First, the resonance modes corresponding to these resonators are subwavelength, which require careful alignment of dye molecules with the resonance hot spots. Secondly, continuous tuning of resonance frequency in plasmonic and dielectric resonator systems possesses fabrication complexity. In addition to the PL enhancement, its active tunability is also important. Several ways exist to actively tune the emission properties. These include the application of magnetic,^{19,20} electric,²¹ and optical^{22,23} fields. Furthermore, a diverse range of tunable metasurfaces based on mechanical actuation,^{24–26} phase-change materials,^{27–31} and liquid crystals^{32–34} exist, offering dynamic tuning of optical properties. For a metasurface, the collective response of subwavelength-sized resonators is primarily determined by the resonator geometry and size.^{35,36} Integrating the emitter into a tunable metasurfaces would allow for active emission tuning. However, all these approaches either require complex experimental setup, fabrication techniques, lack reversibility, or exhibit small

Received: February 4, 2022

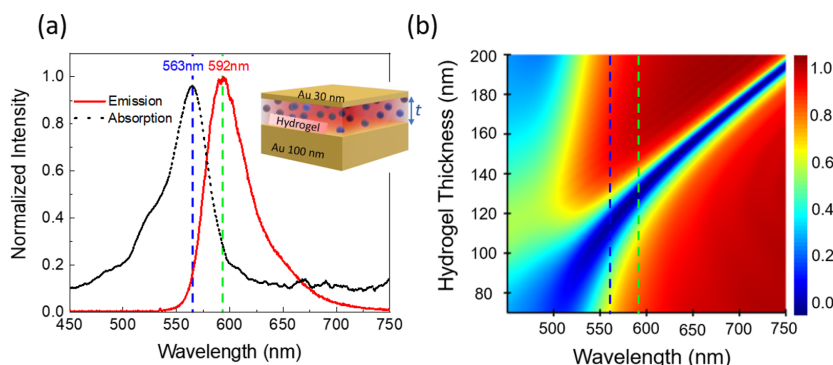


Figure 1. (a) The absorption and emission spectra of RhB are presented as black dotted and red solid curves, respectively. Inset: schematic representation of the RhB-containing hydrogel incorporated into the MIM device. (b) Simulated reflection from the MIM for different hydrogel thicknesses.

spectral tunability.³⁷ In addition, complex and time-consuming fabrication procedures hamper their translation into real-world applications. To circumvent this, we utilize a metal–insulator–metal platform for tuning the emission.

The metal–insulator–metal (MIM) structure is relatively simple and exhibits high-quality-factor resonance.³⁸ The resonance wavelength of the MIM cavity is scalable by simply changing the thickness of the insulating layer. We exploited this property to demonstrate an active emission tuning using a hydrogel as the insulating layer. Hydrogel is a stimuli-responsive hydrophilic cross-linked polymer network capable of holding a large amount of water in its network. The volume and the optical and mechanical properties of the hydrogels can be changed due to the reversible swelling–deswelling process in a humid and aqueous environment.³⁹ An increment in humidity allows the hydrogel to absorb water from the environment and swell, resulting in a relatively large thickness change of the thin hydrogel.^{40,41} Due to this remarkable feature, hydrogels have stood out as promising materials for developing actively tunable plasmonic devices.^{42–44}

To showcase the active emission tuning, we integrated a photoluminescent hydrogel, obtained via covalent functionalization with rhodamine B (RhB) as an emitter (see the [Methods](#) section for further details) into a MIM cavity as a tunable platform. Our results reveal an active emission tuning by varying the thickness of the hydrogel, resulting in maximum emission enhancement when the MIM cavity resonance overlaps with both the absorption and emission bands of the emitter. We demonstrate humidity-responsive PL of the emitter coupled to an actively tunable MIM cavity at room temperature, via both passive and active tuning schemes. In the passive tuning, we fabricated MIM cavities with different thicknesses of the hydrogel-based insulating layer, while for the active tuning, the hydrogel thickness was varied in response to humidity or the presence of water. We envision that our study will pave the way for engineering light–matter interactions, advancing the fundamental understanding and in the longer-term potentially contributing to the technological development of luminescent devices. The proposed solution exhibits real-time tunability, reversibility, and large spectral tuning of the cavity resonance with relatively easy fabrication and experimental setup. The planar topography and scalability of our structure will enable large-area devices to function at the

desired spectral region, being well-positioned to enable tunable light sources.

RESULTS AND DISCUSSION

MIM (Metal–Hydrogel+Dye–Metal) Design. The simultaneous overlap of dye’s emission and absorption bands with the cavity resonance leads to enhanced emission. This arises from a combination of the Purcell effect and the excitation rate enhancement.⁴⁵ This guideline defines the design of the particular MIM structure, especially the dielectric thickness to enhance the emission. The measured absorption and emission of RhB depicted in [Figure 1a](#) show a small Stokes shift of ≈ 30 nm. The black dotted curve represents the absorption spectrum, peaking at 563 nm, which is marked with a blue dashed line, and the red solid line is the emission of RhB with a peak at 592 nm, highlighted using the green dashed line. As [Figure 1a](#) suggests, the wavelength range of 540 to 650 nm is optimal for simultaneous overlap of the cavity resonance with both the emission and absorption of RhB. To identify the suitable thickness range of the dielectric layer of the MIM structure, we utilized both the dye characteristics and the MIM cavity resonance presented in [Figure 1](#). The latter is obtained between the required wavelength region when the dielectric thickness is between ≈ 90 and ≈ 150 nm.

The MIM design and the thickness of the hydrogel layer were obtained using numerical simulation software based on the finite-difference time-domain (FDTD) method. The hydrogel was modeled with a refractive index $n = 1.503$,⁴⁶ and further simulation details are given in [Methods](#). The simulated reflection for the MIM cavity at varying hydrogel thicknesses is shown in [Figure 1b](#), and the positions of absorption and emission maxima of RhB are shown by blue and green dashed lines, respectively.

In order to realize emission-tunable MIM, we deposited a gold (Au) layer using an e-beam evaporator and confirmed its thickness with a stylus profilometer under cleanroom conditions. The insulator layer, the poly(*N*-isopropylacrylamide)-acrylamidobenzophenone (PNIPAm-BP) hydrogel with pendant RhB molecules, was spin-coated on the bottom Au layer and cross-linked with a UV light (see [Methods](#) for more details). The thickness of the hydrogel was varied to tune the cavity resonance using different spin coating conditions. The schematic of the MIM cavity is shown in the inset of [Figure 1a](#),

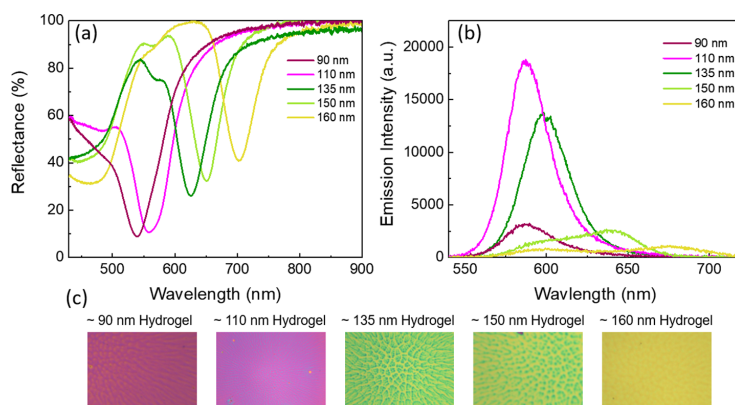


Figure 2. (a) Measured reflectance spectra for the MIM cavities with different hydrogel thicknesses. (b) Steady-state PL spectra of RhB in the different MIM cavities. (c) Optical images of the MIM samples with different hydrogel thicknesses exhibit different bright colors as per their reflectance. The thicknesses of hydrogels were measured with profilometer.

where the thicknesses of the top and bottom metallic layers are 30 and 100 nm, respectively. The bottom layer serves as a reflector while the top layer is partially transparent, allowing to collect the reflected light. Au has been used for the metal layers owing to its nonoxidizing nature and stable plasmonic properties.⁴⁷ We have selected PNIPAm-BP as the insulating layer owing to its excellent thin-film forming^{41,48} and swelling properties.^{49,50} Because of the thin hydrogel layer, the swelling/deswelling modulates the hydrogel thickness, hence changing the resonance of the whole MIM structure.⁵¹

Passive Emission Tuning. To demonstrate passive (i.e., without real-time control) emission tuning by varying the thickness of the MIM, we investigated the effect that the overlap between the cavity resonance and the absorption and emission of the RhB dye has on the emission intensity, by using MIM cavities with dry hydrogel thicknesses from ~ 90 to ~ 160 nm. Here, the dry hydrogel thickness implies its thickness at a relative humidity of 28%. We measured the reflectance and emission from the samples using a $20\times$ air objective as detailed in the [Methods](#) section. [Figure 2a](#) shows the measured reflectance spectra for the MIM cavities with various hydrogel thicknesses. With an increase in the hydrogel thickness, the MIM cavity resonance redshifts, which is also evident from the change in the color of the fabricated samples, as shown in [Figure 2c](#).

[Figure 2b](#) shows the tunable emission of the emitters coupled with different resonance cavities of the MIM structures for passively varying the dry hydrogel thickness to tune the spectral overlapping. The MIM cavity with a dry hydrogel thickness of 90 nm exhibits cavity resonance at 540 nm, which strongly overlaps with the absorption spectrum of RhB and barely with its emission spectrum. This yields very low emission intensity, as shown by the magenta solid line in [Figure 2b](#). Upon increasing the hydrogel thickness to 110 nm, the cavity resonance redshifts and lies at 558 nm ([Figure 2a](#), pink solid line), exhibiting a significant overlap with both the absorption and the emission spectra of RhB. This leads to an opportunity to exploit both the Purcell factor enhancement and the excitation rate enhancement to boost the overall emission of the system.⁴⁵ The simultaneous contribution from both processes yields the maximum PL intensity, and we

observed the highest emission as shown by the pink solid line in [Figure 2b](#) (enhancement factor of ~ 7 as compared to the dry thickness of 90 nm). For the sample with a dry hydrogel thickness of 135 nm, where the cavity resonance overlaps with the emission and only slightly with the tail of the absorption, the emission further redshifts, and its intensity decreases. We also further increased the dry hydrogel thicknesses to 150 nm, which shifted the cavity resonance away from the absorption and emission of RhB, with only a minor overlap with the emission tail. As a result, we observed further reduction of emission intensity with a small shoulder at about 650 nm, as shown in [Figure 2b](#).

We would like to highlight that the underlying principle behind the emission intensity change is either the Purcell factor enhancement (when the cavity resonance overlaps with only the emission band) or both the Purcell enhancement and the excitation rate enhancement (when the cavity resonance overlaps with the absorption and emission bands simultaneously). Since the Stokes shift for RhB is small, it is difficult to completely isolate the contributions arising from the Purcell factor and the excitation rate enhancement. Therefore, the wavelength corresponding to the maximal emission enhancement slightly offsets the cavity resonance wavelength.

Reversible and Active Emission Tuning in Air. Serpe et al. have worked extensively on tunable etalons where the dielectric layer comprises a PNIPAm microgel, which in an aqueous environment responds to different stimuli and displays color tuning.^{52–58} In addition, Chervinskii et al. have shown the dynamic tuning of the MIM cavity resonance by tuning the thickness of a hydrogel insulating layer.⁴⁸ However, all aforementioned studies do not converse emission tuning. Herein, after first exploring the passive tuning of emission, we demonstrate active tuning of emission via hydrogel-based MIM in response to ambient humidity. The humidity-based tuning allows controlling the overlapping region with the emission and absorption of RhB, which manifests as tunable emission.

The passive tuning study revealed 110 nm (see [Figure 2b](#)) as the optimized hydrogel thickness for enhancing the emission intensity. Therefore, for demonstrating the active tuning, we selected the MIM with a dry hydrogel thickness of 110 nm. We used a humidity-controlled chamber to measure the PL spectra

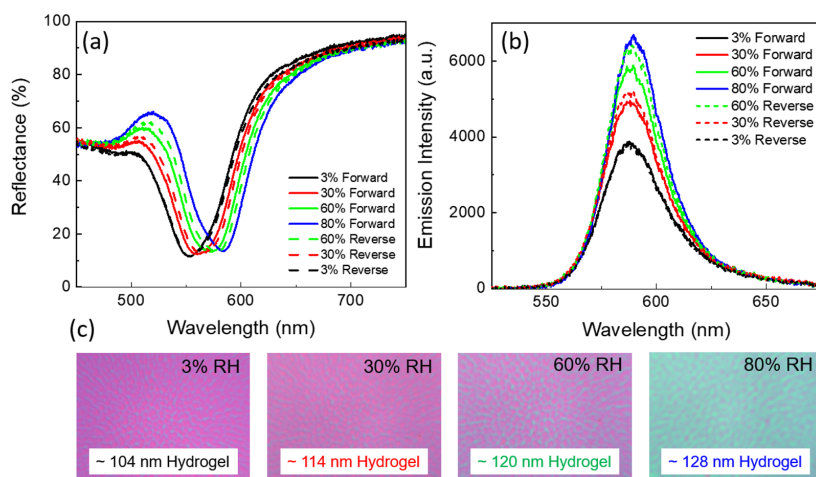


Figure 3. (a) Measured reflectance spectra of MIM with dry hydrogel thickness 110 nm at different humidities. Solid curves show the forward cycle (humidity increases from 3% to 80%) and dashed curves represent the reverse cycle (humidity reduces from 80% to 3%). (b) Steady-state PL spectra of the RhB embedded in the MIM cavity at different humidities. (c) Optical images of the MIM sample at different humidities. The labeled thicknesses are extracted from the simulation.

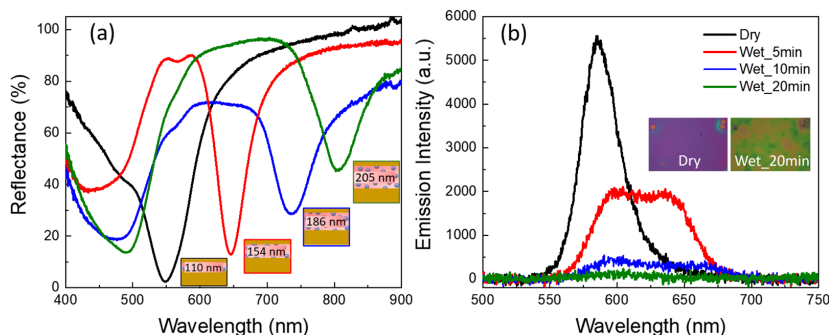


Figure 4. (a) Measured reflectance spectra of MIM with dry hydrogel thickness 110 nm when immersed in deionized water for 5, 10, and 20 min. Insets: the corresponding hydrogel thicknesses for each case, extracted from the simulation. (b) Steady-state PL spectra of MIM in dry case and when immersed in water for 5, 10, and 20 min. Inset: optical images of the sample in two cases: dry and after 20 min immersion.

of the structures, using a customized experimental setup with controlled relative humidity (RH) and performed reflectance and PL measurements (see Figure 3a,b) of the samples in the controlled environment. The measurements were conducted at 3%, 30%, 60%, and 80% RH. Furthermore, measurements were taken in a reversible manner (i.e., from 80% back to 3% RH value) to attain the reversibility of the PL response. Figure 3c shows the optical micrographs of the MIM sample at different RH values. We observed distinct color changes in the samples with the increment of the RH value. This signifies that with the increase in humidity, the hydrogel thickness changes, which in turn modifies the cavity resonance wavelength. We note that the swelling of the hydrogel is strongly dependent on its initial thickness and uniformity. Due to defects present in the spin-coated samples, the swelling process is inevitably somewhat nonuniform. To minimize the nonuniformity, an alternative solution of two-step spin coating was utilized.⁴¹

To quantify the swelling and the corresponding overlap with the RhB absorption and emission spectra, we extracted the

hydrogel thickness from the simulation results. At a constant temperature, with an increase in RH from 3 to 80%, the hydrogel thickness changes from 104 to 128 nm. As a result, the cavity resonance red-shifted by 30 nm, from 548 to 588 nm, as shown in Figure 3a. During this process, the cavity resonance overlaps better with both the absorption and emission bands of the RhB. Hence, we observed an almost 2-fold increase in the emission intensity while increasing the humidity from 3% to 80%, as shown in Figure 3b. The increase in humidity does not directly affect the intrinsic properties of the covalently bonded dye in the hydrogel matrix. Therefore, this increase in emission is solely due to the significant overlap of the cavity with the dye's absorption and emission.

The humidity-induced emission tuning is reversible, and by decreasing the RH from 80% to 3%, the original spectrum is retained. However, the reverse cycle (3.5 h) is slightly slower than the forward cycle (3 h), because the rate at which the hydrogel expels water and the rate at which it absorbs water are different.⁵⁹ We observed that in the reverse cycle, the

humidified sample (80% RH) started expelling the absorbed water gradually with a decrease in RH value, and the cavity resonance retains its original position, as shown in Figure 3a (black, red, and green dashed line). The decrease in the hydrogel thickness during the reverse cycle also allowed to retrieve the PL intensity, as shown in Figure 3b (black, red, and green dashed line). The swelling and deswelling of the hydrogel allowed the reversible humidity-induced tuning of the optical response of the MIM cavity and, hence, reversible control of the PL intensity.

Active Emission Tuning in Water. The previous active tuning scheme was performed in the air where the change in humidity was controlling the hydrogel thickness. However, controlling the thickness of the hydrogel with humidity does not allow large thickness variations. Therefore, to find the limits of our system, we immersed the hydrogel-integrated MIM sample in water. By immersing the sample in deionized water for different time periods, we achieved various hydrogel thicknesses that were generally larger than in the air humidity-controlled case, which allowed us to tune the MIM cavity resonance with large spectral shifts compared to the humidity-based control.

We submerged the sample for 5, 10, and 20 min and monitored the change in the cavity resonance as well as the changes in the PL response of the dyes incorporated within the MIM cavity. Figure 4a shows the measured reflectance spectra of the MIM cavity with a dry hydrogel thickness of 110 nm and three submerged cases.

The inset of Figure 4b shows the optical images of the sample in the dry case, corresponding to a thinner hydrogel layer, and the wet case, where the hydrogel swells⁵¹ and shifts the MIM resonance to a higher wavelength. To evaluate the tuning range of MIM structures, we compared the dry case with the wet case. The dry hydrogel (ambient conditions) thickness was 110 nm. After immersing the sample in deionized water for 20 min, we identified a spectral shift of 255 nm from 550 to 805 nm, as shown in Figure 4a, with black and green solid lines, respectively. As the cavity resonance shifts to a higher wavelength, its overlap with the dye's absorption and emission spectra decrease. As a result, we observed a decrease in the emission intensity, as shown in Figure 4b. Subsequently, for the swollen hydrogel thickness of 205 nm, in which the cavity resonance does not overlap with the dye's emission at all, we observed negligible emission intensity as shown by the green solid line Figure 4b.

CONCLUSION

We report active emission tuning based on emitters embedded within the PNIPAm hydrogel-based metal–insulator–metal device. We demonstrate a 30 nm spectral shift and significant tunability in PL intensity in response to the humidity stimulus. Our structures showed reversible behavior and almost reproduced the initial results by utilizing the deswelling property of hydrogels. The maximum resonance shift (255 nm) and emission tunability were obtained by immersion of incorporated PNIPAm hydrogel-based MIM structure in deionized water. This large spectral shift is remarkable and of great importance, especially for sensing applications. Our approach mitigates the complex fabrication challenges and is versatile in nature that potentially can be translated to a broad spectral range to achieve on-demand tunability by judiciously choosing various hydrogel thicknesses integrated with different dye molecules. We envision a wide range of opportunities in

targets that require on-demand optoelectronic tunability, ranging from integrated circuits to flat optics. Our findings may also provide new possibilities in actively tunable reversible photonic devices and contactless optical sensors.

METHODS

PNIPAm-BP-RhB Copolymer Synthesis. *N*-Isopropylacrylamide (NIPAm) and azobis(isobutyronitrile) (AIBN) were commercially available. NIPAm was used as received, and AIBN was recrystallized from methanol before use. Rhodamine B acrylate was synthesized from commercial rhodamine B as described below. Benzophenone acrylamide (BP) and the copolymer were prepared in a similar fashion to the procedures in our earlier publication,⁴⁸ yielding the copolymer with composition 98.5:2.0:0.5 (NIPAm/BP/RhB), determined with ¹H NMR (500 MHz, CDCl₃).

Rhodamine B (500 mg, 1.04 mmol) and a droplet of *N,N*-dimethylformamide were stirred in dry dichloromethane (6 mL) at 0 °C under argon, and oxalyl chloride (128 μ L, 1.5 mmol) was added dropwise. The mixture was stirred at 0 °C for 30 min, until gas evolution was not observed. This solution was added into a solution of 2-hydroxyethyl acrylate (115 μ L, 1.1 mmol), dry triethylamine (415 μ L, 3.0 mmol), and a catalytic amount of *N,N*-dimethyl-4-aminopyridine in dry dichloromethane (10 mL) and stirred under argon for 24 h. The crude mixture was purified by column chromatography (from pure ethyl acetate to 10% methanol/ethyl acetate) to yield the product (352.5 mg, 59%) as a violet-red crystalline solid. ¹H NMR (500 MHz, DMSO-*d*₆) δ 8.26 (d, *J* = 7.4 Hz, 1H), 7.92 (t, *J* = 7.4 Hz, 1H), 7.86 (t, *J* = 7.4 Hz, 1H), 7.51 (d, *J* = 7.4 Hz, 1H), 7.07 (dd, *J* = 9.5, 2.0 Hz, 2H), 6.99 (d, *J* = 9.2 Hz, 2H), 6.95 (s, 2H), 6.21 (d, *J* = 16.6 Hz, 1H), 5.87–6.02 (2H), 4.14–4.28 (2H), 3.87–4.01 (2H), 3.55–3.74 (8H), 1.20 (t, *J* = 6.9 Hz, 12H).

Solution Preparation, Film Thickness Optimization, and Photopolymerization. PNIPAm-BP-RhB copolymer (this is the composition of the copolymer after polymerization) was dissolved in filtered (filtered using 0.2 μ m pore sized PTFE Teflon filter) 94% ethanol with concentrations of 20 and 30 mg/mL. Using the 20 mg/mL solution, we acquired 90 and 110 nm thicknesses. For higher thicknesses (135–160 nm), we utilized the 30 mg/mL solution. Different thicknesses were achieved by using different spin coating parameters and two solutions. For better dissolution of the copolymer in ethanol, the solutions were sonicated for 10 min. Then magnetic stirring was used at 1400 rpm, 50 °C for 1 h. The solutions were filtered through PTFE membranes with 0.45 μ m pores, then spin-coated the solution on a glass sample to optimize the desired thickness of the hydrogel layer. We used dynamic two-step spin-coating: (1) 10 s at 150 rpm, 100 acceleration during which the PNIPAm-BP-RhB solution was dispensed and predistributed onto the sample; (2) 30 s at 2000 rpm/3000 rpm/4500 rpm, 1000 acceleration to form the final coatings. The deposition was followed by drying for 45 min at 50 °C in a vacuum. The next step was photopolymerization under UV light (365 nm from CoolLED pE-4000 focused on sample area), the time required for complete cross-linking of PNIPAm-BP-RhB copolymer was 40 min. This time was confirmed by the disappearance of the 301 nm peak in the optical transmittance spectra of the reference hydrogel coatings on glass.⁴⁸

FDTD Simulations. MIM design and the thickness of the insulator layer (hydrogel) were optimized using numerical

simulation (Ansys Lumerical FDTD Solutions) based on the finite-difference time-domain (FDTD) method. In the simulation, the symmetric and antisymmetric boundary conditions were applied in the x and y directions to minimize the simulation time, while PML (perfectly matched layer) was used along the z -axis to remove the unwanted reflections. A plane wave was launched from the z -axis to excite the resonance cavity mode. The complex refractive index of Au layers was assigned from the "Johnson and Christy"⁶⁰ data set that was in-built in the software material library. The hydrogel was modeled with a refractive index $n = 1.503$,⁴⁶ which corresponds to the state where there is no water absorbed into the hydrogel. An increase in hydrogel thickness depicts the absorption of water in the hydrogel, and the refractive index of water will influence the effective index of the hydrogel–water complex. However, the change in effective refractive index is relatively small, and its effect on the resonance shift is quite minimal.

MIM Sample Fabrication. The samples were fabricated on $1\text{ cm} \times 1\text{ cm}$ fused silica substrates. First, the samples were cleaned by sonicating them in acetone, isopropanol, and deionized water for 10 min each. The fused silica substrates were blow-dried and treated with oxygen plasma for pristine clean substrates. Subsequently, the adhesive layer of 1 nm Ti, followed by a 100 nm layer of Au was deposited by e-beam evaporation. After that, Au-coated samples were activated by plasma treatment (20 min, 30 W RF power, 1000 mTorr O_2) and started the spin coating right after plasma treatment. Thenceforth, for coating hydrogels of different thicknesses, different spin-coating parameters were used, followed by cross-linking, as explained in [Solution Preparation, Film Thickness Optimization, and Photopolymerization](#). The final gold layer (25–30 nm) was deposited on top of the hydrogel layer by a thermal evaporation system.

Optical Measurements. Microscopic reflectance measurements were performed with a multifunctional WITec alpha300C confocal microscope. The samples with different hydrogel thicknesses were illuminated with a broadband light source (LDLS EQ-99X) through a Zeiss EC "Epiplan" DIC, 20 \times objective (NA = 0.4, WD = 3.0 mm). The reflected light was collected through the same objective and coupled to spectrometers via an optical fiber. For the spectral range of 400–900 nm, we used Ocean Optics Flame UV–vis spectrometer with 1.33 nm full width at half-maximum (FWHM) spectral resolution for detecting the spectral response from the fabricated sample. The samples were measured at room conditions (23 $^{\circ}\text{C}$, 28% room RH - dry state) and after immersion in deionized water for 5, 10, and 20 min (wet state). Here, the relatively long hydrogel swelling time is due to the MIM structure, as the Au layers on the top/bottom of the hydrogel restrict water molecules from penetrating into the cross-linked polymer network.

Additionally, measurements in a controlled humid environment were performed using Linkam Scientific LTS420-H stage with RH95 humidity controller. Reflectance spectra were measured using the same WITec microscope and the samples were illuminated with a broadband light source. We utilized a 2.5 \times air objective with a relatively long working distance to enable the focusing of the optical field onto the samples embedded within the Linkam Scientific LTS420-H stage. For the PL measurement of the samples, we utilized a 532 nm laser to excite the samples to attain the emission peak intensity of the RhB dye incorporated within the MIM structure utilizing a

532 nm long-pass filter (LPF). The response of the samples was coupled to an optical fiber connected to an Ocean Optics Flame UV–vis spectrometer for PL measurement.

AUTHOR INFORMATION

Corresponding Author

Humeyra Caglayan – Tampere University, Faculty of Engineering and Natural Sciences, 33720 Tampere, Finland;
✉ orcid.org/0000-0002-0656-614X;
Email: humeyra.caglayan@tuni.fi

Authors

Dipa Ghindani – Tampere University, Faculty of Engineering and Natural Sciences, 33720 Tampere, Finland

Ibrahim Issah – Tampere University, Faculty of Engineering and Natural Sciences, 33720 Tampere, Finland;
✉ orcid.org/0000-0001-7663-4972

Semyon Chervinskii – Tampere University, Faculty of Engineering and Natural Sciences, 33720 Tampere, Finland;
✉ orcid.org/0000-0002-8560-5679

Markus Lahikainen – Tampere University, Faculty of Engineering and Natural Sciences, 33720 Tampere, Finland;
✉ orcid.org/0000-0002-4891-5352

Kim Kuntze – Tampere University, Faculty of Engineering and Natural Sciences, 33720 Tampere, Finland

Arri Priimagi – Tampere University, Faculty of Engineering and Natural Sciences, 33720 Tampere, Finland;
✉ orcid.org/0000-0002-5945-9671

Complete contact information is available at:
<https://pubs.acs.org/10.1021/acsp Photonics.2c00202>

Funding

This work has been conducted in the framework of the Academy of Finland Flagship Programme (PREIN 320165). H.C. acknowledges the financial support of the European Research Council (Starting Grant Project aQUARiUM; Agreement No. 802986). D.G. acknowledges support from Finnish Cultural Foundation. A.P. acknowledges the financial support of the Academy of Finland (P-Cap, No. 324353 & Center of Excellence Program LIBER, No. 346107).

Notes

The authors declare no competing financial interest.

ACKNOWLEDGMENTS

K.K. is grateful for the Tampere University Graduate School. The authors thank Tuomas Pihlava for the help in collecting some of the PL measurements.

REFERENCES

- (1) Chen, R.; Ng, K. W.; Ko, W. S.; Parekh, D.; Lu, F.; Tran, T.-T. D.; Li, K.; Chang-Hasnain, C. Nanophotonic integrated circuits from nanoresonators grown on silicon. *Nat. Commun.* **2014**, *5*, 4325.
- (2) Atabaki, A. H.; et al. Integrating photonics with silicon nanoelectronics for the next generation of systems on a chip. *Nature* **2018**, *556*, 349–354.
- (3) Leung, B. O.; Chou, K. C. Review of Super-Resolution Fluorescence Microscopy for Biology. *Appl. Spectrosc.* **2011**, *65*, 967–980.
- (4) Lin, K.; et al. Perovskite light-emitting diodes with external quantum efficiency exceeding 20%. *Nature* **2018**, *562*, 245–248.
- (5) Campbell, P. S.; Yang, M.; Pitz, D.; Cybinska, J.; Mudring, A.-V. Highly Luminescent and Color-Tunable Salicylate Ionic Liquids. *Chem. Eur. J.* **2014**, *20*, 4704–4712.

- (6) Huang, Y.; Cohen, T. A.; Luscombe, C. K. Naturally Derived Organic Dyes for LED Lightings of High Color Rendering and Fidelity Index. *Advanced Sustainable Systems* **2022**, *6*, 2000300.
- (7) Duarte, F. J. Organic Dye Lasers: Brief History and Recent Developments. *Opt. Photon. News* **2003**, *14*, 20–25.
- (8) Toninelli, C.; et al. Single organic molecules for photonic quantum technologies. *Nat. Mater.* **2021**, *20*, 1615–1628.
- (9) Hoang, T. B.; Akselrod, G. M.; Mikkelsen, M. H. Ultrafast Room-Temperature Single Photon Emission from Quantum Dots Coupled to Plasmonic Nanocavities. *Nano Lett.* **2016**, *16*, 270–275.
- (10) Jin, C.-Y.; John, R.; Swinkels, M. Y.; Hoang, T. B.; Midolo, L.; van Veldhoven, P. J.; Fiore, A. Ultrafast non-local control of spontaneous emission. *Nat. Nanotechnol.* **2014**, *9*, 886–890.
- (11) Staude, I.; Khardikov, V. V.; Fofang, N. T.; Liu, S.; Decker, M.; Neshev, D. N.; Luk, T. S.; Brener, I.; Kivshar, Y. S. Shaping Photoluminescence Spectra with Magnetoelectric Resonances in All-Dielectric Nanoparticles. *ACS Photonics* **2015**, *2*, 172–177.
- (12) Pelton, M. Modified spontaneous emission in nanophotonic structures. *Nat. Photonics* **2015**, *9*, 427–435.
- (13) Novotny, L.; Hecht, B. *Principles of Nano-Optics*, 2nd ed., Frontmatter; Cambridge University Press, 2012; pp 1–VI.
- (14) Pokhriyal, A.; Lu, M.; Huang, C. S.; Schulz, S.; Cunningham, B. T. Multicolor fluorescence enhancement from a photonics crystal surface. *Appl. Phys. Lett.* **2010**, *97*, 121108.
- (15) Pokhriyal, A.; Lu, M.; Chaudhry, V.; George, S.; Cunningham, B. T. Enhanced fluorescence emission using a photonic crystal coupled to an optical cavity. *Appl. Phys. Lett.* **2013**, *102*, 221114.
- (16) Chen, W.; Long, K. D.; Yu, H.; Tan, Y.; Choi, J. S.; Harley, B. A.; Cunningham, B. T. Enhanced live cell imaging via photonic crystal enhanced fluorescence microscopy. *Analyst* **2014**, *139*, 5954–5963.
- (17) Staude, I.; Schilling, J. Metamaterial-inspired silicon nanophotonics. *Nat. Photonics* **2017**, *11*, 274–284.
- (18) Kuznetsov, A. I.; Miroshnichenko, A. E.; Brongersma, M. L.; Kivshar, Y. S.; Luk'yanchuk, B. Optically resonant dielectric nanostructures. *Science* **2016**, *354*, aag2472.
- (19) Hayne, M.; Bansal, B. High-field magneto-photoluminescence of semiconductor nanostructures. *Luminescence* **2012**, *27*, 179–196.
- (20) Liu, Y.; Wang, D.; Shi, J.; Peng, Q.; Li, Y. Magnetic Tuning of Upconversion Luminescence in Lanthanide-Doped Bifunctional Nanocrystals. *Angew. Chem.* **2013**, *125*, 4462–4465.
- (21) Empedocles, S. A.; Bawendi, M. G. Quantum-confined stark effect in single CdSe nanocrystallite quantum dots. *Science* **1997**, *278*, 2114–2117.
- (22) Wang, Y.; Ding, T. Optical tuning of plasmon-enhanced photoluminescence. *Nanoscale* **2019**, *11*, 10589–10594.
- (23) Fonseca Deichmann, V. A.; Yakutkin, V.; Balushev, S.; Akcelrud, L. Optical Tuning of the Fluorescence Spectrum of a π -Conjugated Polymer through Excitation Power. *J. Phys. Chem. B* **2011**, *115*, 6385–6394.
- (24) Arbabi, E.; Arbabi, A.; Kamali, S. M.; Horie, Y.; Faraji-Dana, M.; Faraon, A. MEMS-tunable dielectric metasurface lens. *Nat. Commun.* **2018**, *9*, 812.
- (25) Holsteen, A. L.; Raza, S.; Fan, P.; Kik, P. G.; Brongersma, M. L. Purcell effect for active tuning of light scattering from semiconductor optical antennas. *Science* **2017**, *358*, 1407–1410.
- (26) Liu, J.; Zeng, H.; Cheng, M.; Wang, Z.; Wang, J.; Cen, M.; Luo, D.; Priimagi, A.; Liu, Y. J. Photoelastic plasmonic metasurfaces with ultra-large near infrared spectral tuning. *Mater. Horiz.* **2022**, *9*, 942–951.
- (27) Rensberg, J.; Zhang, S.; Zhou, Y.; McLeod, A. S.; Schwarz, C.; Goldflam, M.; Liu, M.; Kerbusch, J.; Nawrodt, R.; Ramanathan, S.; Basov, D. N.; Capasso, F.; Ronning, C.; Kats, M. A. Active Optical Metasurfaces Based on Defect-Engineered Phase-Transition Materials. *Nano Lett.* **2016**, *16*, 1050–1055.
- (28) Kats, M. A.; Sharma, D.; Lin, J.; Genevet, P.; Blanchard, R.; Yang, Z.; Qazilbash, M. M.; Basov, D. N.; Ramanathan, S.; Capasso, F. Ultra-thin perfect absorber employing a tunable phase change material. *Appl. Phys. Lett.* **2012**, *101*, 221101.
- (29) Krishnamoorthy, H. N. S.; Zhou, Y.; Ramanathan, S.; Narimanov, E.; Menon, V. M. Tunable hyperbolic metamaterials utilizing phase change heterostructures. *Appl. Phys. Lett.* **2014**, *104*, 121101.
- (30) Gholipour, B.; Zhang, J.; MacDonald, K. F.; Hewak, D. W.; Zheludev, N. I. An All-Optical, Non-volatile, Bidirectional, Phase-Change Meta-Switch. *Adv. Mater.* **2013**, *25*, 3050–3054.
- (31) Zhu, Z.; Evans, P. G.; Haglund, R. F.; Valentine, J. G. Dynamically Reconfigurable Metadevice Employing Nanostructured Phase-Change Materials. *Nano Lett.* **2017**, *17*, 4881–4885.
- (32) Sautter, J.; Staude, I.; Decker, M.; Rusak, E.; Neshev, D. N.; Brener, I.; Kivshar, Y. S. Active Tuning of All-Dielectric Metasurfaces. *ACS Nano* **2015**, *9*, 4308–4315.
- (33) Komar, A.; Paniagua-Domínguez, R.; Miroshnichenko, A.; Yu, Y. F.; Kivshar, Y. S.; Kuznetsov, A. I.; Neshev, D. Dynamic Beam Switching by Liquid Crystal Tunable Dielectric Metasurfaces. *ACS Photonics* **2018**, *5*, 1742–1748.
- (34) Komar, A.; Fang, Z.; Bohn, J.; Sautter, J.; Decker, M.; Miroshnichenko, A.; Pertsch, T.; Brener, I.; Kivshar, Y. S.; Staude, I.; Neshev, D. N. Electrically tunable all-dielectric optical metasurfaces based on liquid crystals. *Appl. Phys. Lett.* **2017**, *110*, 071109.
- (35) Smith, D. R.; Pendry, J. B.; Wiltshire, M. C. K. Metamaterials and Negative Refractive Index. *Science* **2004**, *305*, 788–792.
- (36) Pendry, J. B.; Schurig, D.; Smith, D. R. Controlling Electromagnetic Fields. *Science* **2006**, *312*, 1780–1782.
- (37) Bohn, J.; Bucher, T.; Chong, K. E.; Komar, A.; Choi, D.-Y.; Neshev, D. N.; Kivshar, Y. S.; Pertsch, T.; Staude, I. Active Tuning of Spontaneous Emission by Mie-Resonant Dielectric Metasurfaces. *Nano Lett.* **2018**, *18*, 3461–3465.
- (38) Ogawa, S.; Kimata, M. Metal-Insulator-Metal-Based Plasmonic Metamaterial Absorbers at Visible and Infrared Wavelengths: A Review. *Materials* **2018**, *11*, 458.
- (39) Wei, M.; Gao, Y.; Li, X.; Serpe, M. J. Stimuli-responsive polymers and their applications. *Polym. Chem.* **2017**, *8*, 127–143.
- (40) Tang, L.; Wang, L.; Yang, X.; Feng, Y.; Li, Y.; Feng, W. Poly(N-isopropylacrylamide)-based smart hydrogels: Design, properties and applications. *Prog. Mater. Sci.* **2021**, *115*, 100702.
- (41) Nash, M. E.; Carroll, W. M.; Foley, P. J.; Maguire, G.; Connell, C. O.; Gorelov, A. V.; Beloshapkin, S.; Rochev, Y. A. Ultra-thin spin coated crosslinkable hydrogels for use in cell sheet recovery—synthesis, characterisation to application. *Soft Matter* **2012**, *8*, 3889–3899.
- (42) Song, J. E.; Cho, E. C. Dual-responsive and Multi-functional Plasmonic Hydrogel Valves and Biomimetic Architectures Formed with Hydrogel and Gold Nanocolloids. *Sci. Rep.* **2016**, *6*, 34622.
- (43) Tian, E.; Wang, J.; Zheng, Y.; Song, Y.; Jiang, L.; Zhu, D. Colorful humidity sensitive photonic crystal hydrogel. *J. Mater. Chem.* **2008**, *18*, 1116–1122.
- (44) van Heeswijk, E. P. A.; Kragt, A. J. J.; Grossiord, N.; Schenning, A. P. H. J. Environmentally responsive photonic polymers. *Chem. Commun.* **2019**, *55*, 2880–2891.
- (45) Ghindani, D.; Rashed, A. R.; Caglayan, H. Unveiling spontaneous emission enhancement mechanisms in metal–insulator–metal nanocavities. *Photonics Research* **2021**, *9*, 237.
- (46) Brasse, Y.; Müller, M. B.; Karg, M.; Kuttner, C.; König, T. A. F.; Fery, A. Magnetic and Electric Resonances in Particle-to-Film-Coupled Functional Nanostructures. *ACS applied materials and interfaces* **2018**, *10*, 3133–3141.
- (47) Maier, S. A. *Plasmonics: Fundamentals and Applications*. Springer Science and Business Media; Springer: New York, NY, 2007; p 159.
- (48) Chervinskii, S.; Issah, I.; Lahikainen, M.; Rashed, A. R.; Kuntze, K.; Priimagi, A.; Caglayan, H. Humidity- and Temperature-Tunable Metal–Hydrogel–Metal Reflective Filters. *ACS Appl. Mater. Interfaces* **2021**, *13*, 50564–50572.
- (49) Christensen, S. K.; Chiappelli, M. C.; Hayward, R. C. Gelation of Copolymers with Pendant Benzophenone Photo-Cross-Linkers. *Macromolecules* **2012**, *45*, 5237–5246.

- (50) Lee, E.; Kim, D.; Yang, S. Y.; Oh, J.-W.; Yoon, J. Photocrosslinkable comb-type copolymers bearing a benzophenone moiety for the enhanced swelling kinetics of hydrogels. *Polym. Chem.* **2017**, *8*, 6786–6794.
- (51) Yoon, J.; Cai, S.; Suo, Z.; Hayward, R. C. Poroelastic swelling kinetics of thin hydrogel layers: comparison of theory and experiment. *Soft Matter* **2010**, *6*, 6004–6012.
- (52) Xu, W.; Gao, Y.; Serpe, M. J. Electrochemically Color Tunable Poly(N-isopropylacrylamide) Microgel-based Etalons. *J. Mater. Chem. C* **2014**, *2*, 3873–3878.
- (53) Ahiabu, A.; Serpe, M. J. Rapidly Responding pH- and Temperature-Responsive Poly (N-Isopropylacrylamide)-Based Microgels and Assemblies. *ACS Omega* **2017**, *2*, 1769–1777.
- (54) Carter, M. C. D.; Sorrell, C. D.; Serpe, M. J. Deswelling Kinetics of Color Tunable Poly(N-Isopropylacrylamide) Microgel-Based Etalons. *J. Phys. Chem. B* **2011**, *115*, 14359–14368.
- (55) Hu, L.; Serpe, M. J. Color-Tunable Etalons Assembled from Poly (N-Isopropylacrylamide) Based Microgels. *Polymers* **2012**, *4*, 134–149.
- (56) Sorrell, C. D.; Carter, M. C. D.; Serpe, M. J. Color Tunable Poly (N-Isopropylacrylamide)-co-Acrylic Acid Microgel–Au Hybrid Assemblies. *Adv. Funct. Mater.* **2011**, *21*, 425–433.
- (57) Sorrell, C. D.; Serpe, M. J. Reflection Order Selectivity of Color-Tunable Poly(N-isopropylacrylamide) Microgel Based Etalons. *Adv. Mater.* **2011**, *23*, 4088–4092.
- (58) Gao, Y.; Serpe, M. J. Light-Induced Color Changes of Microgel-Based Etalons. *ACS Appl. Mater. Interfaces* **2014**, *6*, 8461–8466.
- (59) Salzmann, P.; Perrotta, A.; Coclite, A. M. Different Response Kinetics to Temperature and Water Vapor of Acrylamide Polymers Obtained by Initiated Chemical Vapor Deposition. *ACS Appl. Mater. Interfaces* **2018**, *10*, 6636–6645.
- (60) Johnson, P. B.; Christy, R. W. Optical Constants of the Noble Metals. *Phys. Rev. B* **1972**, *6*, 4370–4379.

Recommended by ACS

A Deformable Low-Threshold Optical Limiter with Oligothiophene-Doped Liquid Crystals

Koji Usui, Atsushi Shishido, *et al.*

MAY 04, 2021

ACS APPLIED MATERIALS & INTERFACES

READ 

Markedly Improved Performance of Optically Pumped Organic Lasers with Two-Dimensional Distributed-Feedback Gratings

Chathurangani A. M. Senevirathne, Chihaya Adachi, *et al.*

MARCH 11, 2021

ACS PHOTONICS

READ 

Organic Microlaser Arrays: From Materials Engineering to Optoelectronic Applications

Jie Liang, Yong Sheng Zhao, *et al.*

APRIL 27, 2021

ACCOUNTS OF MATERIALS RESEARCH

READ 

A Photochromic Zinc–Viologen Framework with a High-Contrast Nonlinear Optical Switchable Behavior

Shi-Li Li, Xian-Ming Zhang, *et al.*

SEPTEMBER 03, 2021

CRYSTAL GROWTH & DESIGN

READ 

Get More Suggestions >

PUBLICATION

III

Gate Tunable Coupling of Epsilon-Near-Zero and Plasmonic Modes

D. Ghindani, A. R. Rashed, M. Habib and H. Caglayan

Advanced Optical Materials 9.22 (2021), 2100800

DOI: <https://doi.org/10.1002/adom.202100800>

Publication reprinted with the permission of the copyright holders

Gate Tunable Coupling of Epsilon-Near-Zero and Plasmonic Modes

Dipa Ghindani, Alireza R. Rashed, Mohsin Habib, and Humeyra Caglayan*

In this work, an active tuning of the coupling strength in a strongly coupled system comprised of a thin epsilon-near-zero material and gold nanorods as plasmonic resonators is demonstrated. A novel gating scheme is developed where an ionic liquid is employed to bias the coupled system and tune the coupling in transmission mode. A significant tuning of the coupled resonance up to 30 nm is observed by changing the bias voltages from 0 to 4.5 V. This control mechanism on strong coupling opens exciting opportunities for various disruptive applications by offering advanced control and tunability on strongly coupled systems.

1. Introduction

The strong-coupling phenomenon has been exploited in different systems as it enables the hybrid modes with an increased degree of freedom. Metallic structures are widely employed to achieve strong coupling owing to their ability to confine the electromagnetic field to deep subwavelength volumes.^[1,2] The strong coupling manifests itself as splitting of the resonance into two hybrid states in the spectral domain where the separation defines the coupling strength.^[3,4] However, the low-quality factor of metallic nanostructures put the limitation to achieve strong coupling. Fortunately, this limitation can be lifted by employing epsilon-near-zero (ENZ) materials that offer subwavelength field enhancement^[5,6] or quantum heterostructures that offer large dipole transitions.^[7] ENZ materials such as highly doped transparent conducting oxide (TCO) can confine the electromagnetic fields into the deep subwavelength volume at the wavelength where the real part of the dielectric permittivity crosses zero. Furthermore, it has been demonstrated that ultrathin ENZ films support ENZ modes^[8] with strong electric field confinement and excitation of the enhanced local density

of optical states. Integration of metallic resonators with such materials to realize strong coupling provides advantages in spectral scalability and device miniaturization. The combination of ENZ film with plasmonic nanostructures has shown striking performance in enhanced nonlinearity,^[9–11] subwavelength tunneling, beam shaping, and steering.^[12,13] In a similar direction, previous studies with ENZ-plasmonic nanostructures hybrid system have shown to exhibit strong coupling.^[14,15] Moreover, the strongly coupled mode is modified passively by changing the geometrical parameters of the antenna^[5] and changing the doping levels in quantum well-plasmonic resonator system.^[7]

In recent studies, various applications where ENZ material is integrated with different photonics platforms^[16,17] has been demonstrated. For example, the inclusion of ENZ material with metallic structures exhibited diverse functionalities like tunable absorbers,^[18,19] beam steering,^[20] waveguides^[21] and integrated plasmonic devices.^[22] It is highly desired to achieve an active tuning in a strongly coupled system that offers the coupling of light–matter interactions to uplift the application capability and achieve advanced functionality. Although, the permittivity of ENZ materials is utilized in several studies to tune the optical properties by electrical biasing,^[18,20,22] so far, the tuning of strong coupling has been demonstrated only by passive means. While on the other hand, most of the electrical biasing schemes are limited to operating in reflection mode due to the presence of a back reflector.

Motivated by the exciting possibilities and opportunities opened up by the strong coupling of ENZ modes and plasmonic modes for different applications, in this work, we introduce the dynamic tuning of this coupling with a novel gating scheme using ionic liquid. We experimentally demonstrated the electrical tuning of the coupling strength in the hybrid structure consisting of a gold nanorod array on a thin film of indium tin oxide (ITO). Besides, all the results presented here are compared with numerical simulations, demonstrating good agreement with the design and experiments. The hybridization of ENZ mode on the ITO thin film and localized surface plasmon (LSP) mode on the nanorods manifests as splitting in the transmission spectra that signifies the strong coupling regime. In our work, we employed a novel gating scheme that operates in transmission mode without the requirement of a back metallic gating layer. Notably, same design can be operated to achieve the tuning in reflection mode which can be enhanced further introducing a back reflector. This diversifies the application range of our gating scheme.

D. Ghindani, A. R. Rashed, M. Habib, H. Caglayan
 Photonics
 Faculty of Engineering and Natural Sciences
 Tampere University
 Tampere 33720, Finland
 E-mail: humeyra.caglayan@tuni.fi

 The ORCID identification number(s) for the author(s) of this article can be found under <https://doi.org/10.1002/adom.202100800>.

© 2021 The Authors. Advanced Optical Materials published by Wiley-VCH GmbH. This is an open access article under the terms of the Creative Commons Attribution License, which permits use, distribution and reproduction in any medium, provided the original work is properly cited.

DOI: 10.1002/adom.202100800

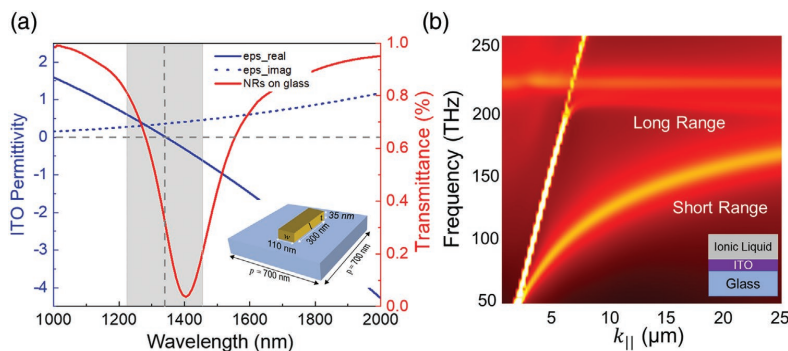


Figure 1. a) Experimentally recorded complex permittivity of 40 nm thin ITO film (blue solid and dotted line). Simulated transmittance spectra of the optimized nanorods (NRs) array on a glass substrate (red solid line) with the ionic liquid background and the inset shows schematic of the unit cell consisting of gold nanorod fabricated on a glass substrate. b) Dispersion relation of the ionic liquid-ENZ-glass three-layered system.

2. Results and Discussion

ITO is compatible with semiconductor processing and has been widely used in commercial devices such as displays, solar panels, etc. ITO is adopted as an active material for this study due to its remarkable properties like tunable permittivity,^[23–25] lower optical losses in combination with a large electrical conductivity. To characterize the dispersion of ITO, we performed the ellipsometry measurement on 40 nm ITO thin film and extracted the complex permittivity. In **Figure 1a**, the real and imaginary parts of the ITO thin film's permittivity are shown as the blue solid and dotted line, respectively. The zero permittivity ($\epsilon \approx 0$) region that spans from 1230 to 1450 nm is highlighted in **Figure 1a**. The dispersion relation for ITO thin film embedded in ionic liquid (inset **Figure 1b**) was calculated using the finite-difference time-domain (FDTD) technique. The simulation was performed using Bloch boundary conditions and experimentally recorded permittivity of ITO is fed into the simulation. The cloud of dipoles with different phase and orientations were placed in the simulation region. To obtain the dispersion graph (**Figure 1b**), we swept different values of wave vector k_x (i.e., $k_{||}$) and calculated the corresponding eigen-frequencies. In this process, the simulation time was kept sufficiently long enough to attenuate the modes which are not supported by our structure. In **Figure 1b**, the short-range and long-range surface plasmon modes of ITO thin films are marked. The dispersion of long-range mode is nearly flat for a large range of transverse wave vectors ($k_{||}$) near 220 THz frequency. This is consistent with the ellipsometry result shown in **Figure 1a**, which identifies the ENZ wavelength at 1340 nm (≈ 223 THz). Therefore, the long-range surface plasmon is referred as the ENZ mode.^[14] However, due to the impedance mismatch at the interface between the ionic liquid and the ENZ medium, the ENZ modes' excitation is inefficient.

Whereas the plasmonic nanostructures confine the incident electromagnetic field at a deep subwavelength scales due to excitation of LSP which leads to a remarkable enhancement of the local field. Therefore, in order to enable high electromagnetic fields inside the ENZ film and generate the LSP mode, we

have used Au nanorods in this study. To optimize Au nanorod's dimension such that their plasmonic resonance is in the ENZ region of the ITO film, we performed FDTD numerical simulation using Ansys Lumerical FDTD Solutions. The linearly polarized plane wave source of wavelengths 1000–2000 nm was utilized to excite the nanorod with polarization along the nanorod's long edge. The gold (Au) was modeled by using Johnson and Christy material data^[26] from the in build material library of Lumerical. In the optimization process, we kept the background refractive index to 1.41 to emulate ionic liquid ambiance. As will be shown, the ionic liquid is needed for tunability. The simulated transmission plot for the optimized nanorod is shown in **Figure 1a** (solid red line). The transmission spectra for various other dimensions are presented in **Figure S4a**, Supporting Information. The dimensions of the optimized nanorod antenna are length (l) = 300 nm, width (w) = 110 nm, and thickness (t) = 35 nm as marked in the inset of **Figure 1a**. We kept the square periodicity (p) of 700 nm to maximize the density of the nanorod while avoiding the cross-talks between them.

Once we identified the modes, the strong coupling of these modes is investigated by bringing them to the same platform. We experimentally recorded the ENZ-integrated plasmonic hybrid system's transmission spectra with (solid red line) and without ionic liquid (solid black line), as shown in **Figure 2a**. The presence of the ionic liquid red-shifts the overall spectra due to an increase in background refractive index ($n_{\text{air}} = 1$ to $n_{\text{ionicliquid}} \approx 1.41$). In the optimization process of the plasmonic antenna, the background refractive index is included as 1.41. As a result, its resonance position is red-shifted to the ENZ region. Therefore, in **Figure 2a**, both upper and lower polaritons are clearly visible, which shows that in the presence of ionic liquid, the system exhibits strong coupling that manifests as apparent spectral splitting (solid red line). In contrast, the system without ionic liquid is only weakly coupled. The inset of **Figure 2a** represents the scanning electron microscope (SEM) image of the plasmonic structures (top view), showing the geometry of the gold antennas (square lattice Au nanorods). Note that fabricated nanoantennas are slightly different from the simulated

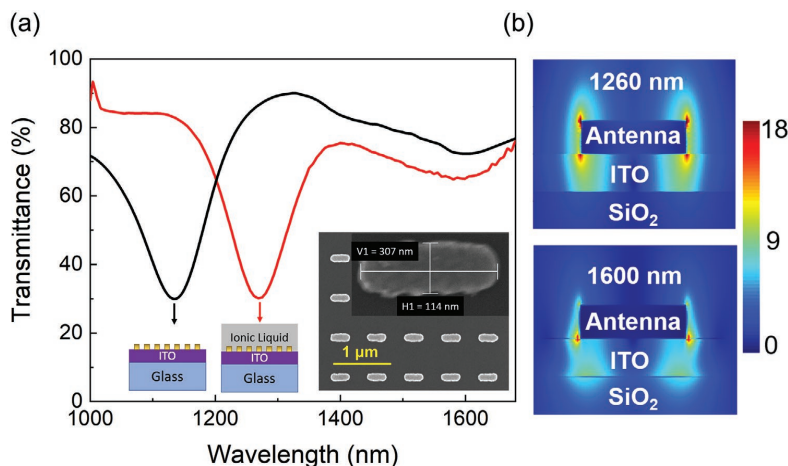


Figure 2. a) Experimentally recorded transmission spectra of ITO integrated plasmonic antenna hybrid system with and without ionic liquid and inset shows SEM image of the nanorods (top view) showing the gold antennas (square lattice Au nanorods). b) Electric field (E_z) distribution at lower polariton (1260 nm) and upper polariton (1600 nm) for nanorod-ITO integrated system.

ones due to the fabrication imperfections, which results in antenna edges being rounded off.

The electric field confinement in the plasmonic structure and ENZ layer of the strongly coupled system shows the hybrid characteristics' features. The antennas placed on the ITO film allow the electric field to be concentrated inside the ITO layer resulting in enhancement of the field intensity at polaritonic wavelengths. Figure 2b shows electric field distribution of the ENZ-integrated system, calculated at lower polariton (1260 nm) and upper polariton (1600 nm) that display a mixture of localized plasmons and ENZ mode confinement. The resonance mode of the nanorod used in our study is electric in nature, as the calculated surface currents (Section S2, Supporting Information) show the dipole like oscillations of the modes.

To achieve the dynamic tunability of ENZ-LSP coupling, we designed a novel electrical gating scheme that allows transmission measurements providing an extra dimension of performance. In previous studies to achieve the tunability, the gating schemes require the metallic plate to be present at the backside of metadevices which severely limits the mode of operation to be only in reflection.^[18,20,22] In contrast, our designed gating is versatile in nature, which is compatible with operating in both the transmission and reflection modes. The schematic of the designed architecture to achieve the electrical gating in transmission mode is shown in Figure 3a. The gating assembly consists of two plates: bottom plate includes the substrate with 40 nm ITO thin film followed by a square array of gold nanorods as shown in Figure 2a inset, and the top plate is a bare glass. On both of the substrates, we created a gold periphery window in order to connect copper wires with good ohmic contact. To avoid a short circuit, these two substrates are separated from each other by insulating tapes. The ionic liquid^[27] is sandwiched between these two plates, which serve as media to accumulate ions at ITO and ionic liquid interface upon electrical biasing.

The active tuning of strongly coupled ENZ-LSP modes is achieved by electrical biasing. The experimentally acquired spectra for various bias voltages are shown in Figure 3b. For clarity, in this figure, we have shown only the lower polariton, and the individual spectrum for different voltages is offset vertically. By increasing the bias voltage from 0 to 4.5 V, the lower polariton shifts from 1260 to 1288 nm, while there is a subtle change in the upper polariton as shown in Section S3, Supporting Information. As the electric field confinement at lower polariton (as shown in Figure 2b) is more intense than the upper polariton, the lower polariton shows better tuning with respect to upper polariton. Additionally, the change in the permittivity with different external bias voltages is more effective closer to the ENZ wavelength where we observe the lower polariton.

Since the splitting between the upper and lower polariton is proportional to the coupling strength,^[28] change in the lower polariton's wavelength represents the change in the coupling strength of the strongly coupled system. Further, this coupling's tunability was verified using different nanorod dimensions, as shown in Figure S4, Supporting Information. The nanorods' size is considered so that the plasmon resonance still resides inside the ENZ region (gray shaded region of Figure 1a), which ensures the system remains in the strong coupling regime.

The achieved tunability lies under the occurred modification in the permittivity of the ITO film as a response to the applied DC voltage. Under the presence of the electrical bias, the ions in an ionic liquid get polarized and accumulate at both the top and bottom interfaces. The increase in the voltage results in an increment of charge concentration at the interface of ITO and ionic liquid. These assembled ions at the interface induce charge increment that in turn changes the permittivity of the ITO. By increasing the bias voltage, the density of the ions increases and saturates after a threshold voltage which

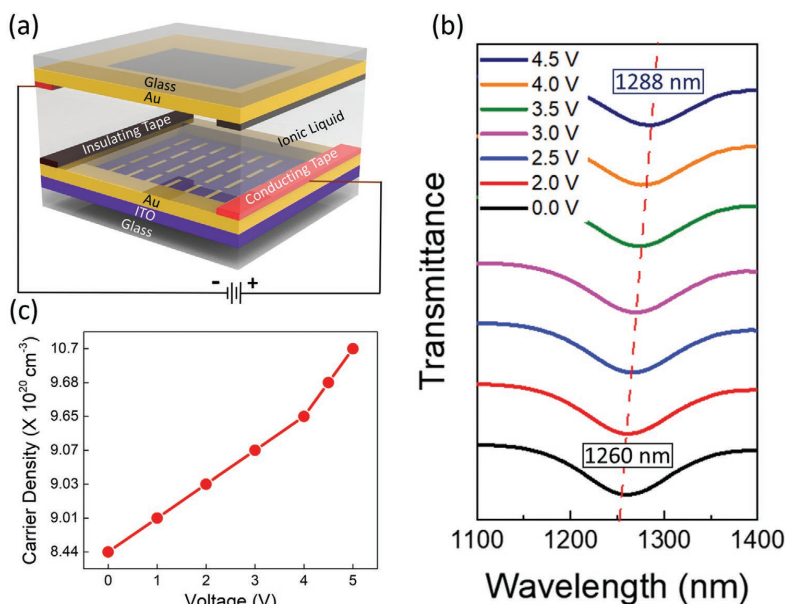


Figure 3. a) The schematic of a novel gating architecture for the electrical gating in transmission mode. b) Experimentally recorded transmission spectra near lower polariton wavelength at different bias voltages (for clarity, individual spectra are offset vertically). c) Experimentally recorded carrier densities in ITO for various voltages using Hall measurement system.

is 4.5 V in our case. To validate this point, we performed the Hall measurement on the ITO gated system (Figure S6a, Supporting Information) with developed biasing architecture. Figure 3c shows the measured carrier concentration in ITO for various voltages using the Hall measurement system. It is evident that by increasing the voltage, the carrier concentration changes due to the polarized ionic liquid. This enhanced carrier density changes the ITO permittivity, allowing us to tune the strong coupling between plasmonic nanorods and the ENZ layer. Thus, changing the bias voltage offers electrical tunability of ENZ-LSP hybrid modes' coupling strength that manifests as a change in the spectral splitting, as shown in Figure S3, Supporting Information.

3. Conclusion

We developed an electrically tunable strongly coupled ENZ-LSP system based on a novel gating scheme. The strong coupling between optimally designed plasmonic nanorods and thin ITO film manifests as splitting in transmission spectra of the structure. The developed ionic liquid based gating system allows tuning the permittivity of the ITO film. Subsequently, the coupling strength between ENZ and LSP mode gets changed by changing the applied DC voltage. We observed up to 30 nm of shift in lower polariton. Since the lower and upper polaritons' frequency difference quantifies the coupling strength, the spectral shift of the lower polariton via applied voltage signifies tuning the coupling strength. Dynamically

tunable strongly coupled systems are essential for exploring fundamental physics and developing applications. Therefore, our study opens up a new avenue to explore many new phenomena and enhance integrated nanodevice performance by offering advanced control and tunability on strongly coupled systems. Additionally, the system exhibits reversible behavior and our gating scheme can be implemented in both transmission and reflection mode thus broadens the application horizon of photonic devices toward tunable flat lens, beam steering, and transmissive spatial light modulators which is vital for LIDAR and wireless communication.

Supporting Information

Supporting Information is available from the Wiley Online Library or from the author.

Acknowledgements

The authors acknowledge the financial support of the Academy of Finland Flagship Programme (PREIN - decisions 320165). H.C. acknowledges financial support of the European Research Council (Starting Grant project aQUARium; Agreement No. 802986). D.G. acknowledges support from The Finnish National Agency for Education through an EDUFI Fellowship and The Finnish Cultural Foundation. The authors also thank Bilge Can Yildiz for the initial scientific discussions, Antti Tukiainen for Hall measurements, and Ibrahim Issah for his help in the dispersion calculations.

Conflict of Interest

The authors declare no conflict of interest.

Data Availability Statement

The data that support the findings of this study are available from the corresponding author upon reasonable request.

Keywords

epsilon-near-zero mode, epsilon-near-zero materials, gating, indium tin oxide, plasmonic mode, strong coupling

Received: April 19, 2021

Revised: July 28, 2021

Published online:

- [1] A. Benz, S. Campione, S. Liu, I. Montañó, J. F. Klem, A. Allerman, J. R. Wendt, M. B. Sinclair, F. Capolino, I. Brener, *Nat. Commun.* **2013**, 4.
- [2] G. Scalari, C. Maissen, D. Turčinková, D. Hagenmüller, S. De Liberato, C. Ciuti, C. Reichl, D. Schuh, W. Wegscheider, M. Beck, J. Faist, *Science* **2012**, 335, 1323.
- [3] S. D. Liberato, C. Ciuti, I. Carusotto, *Phys. Rev. Lett.* **2007**, 98, 103602.
- [4] P. Törmä, W. L. Barnes, *Rep. Prog. Phys.* **2014**, 78, 013901.
- [5] S. Campione, J. R. Wendt, G. A. Keeler, T. S. Luk, *ACS Photonics* **2016**, 3, 293.
- [6] B. C. Yildiz, H. Caglayan, *Phys. Rev. B* **2020**, 102, 165303.
- [7] A. Benz, S. Campione, M. W. Moseley, J. J. Wierer, A. A. Allerman, J. R. Wendt, I. Brener, *ACS Photonics* **2014**, 1, 906.
- [8] S. Campione, I. Brener, F. Marquier, *Phys. Rev. B* **2015**, 91, 121408.
- [9] M. Z. Alam, S. A. Schulz, J. Upham, I. De Leon, R. W. Boyd, *Nat. Photonics* **2018**, 12, 79.
- [10] J. Bohn, T. S. Luk, C. Tollerton, S. W. Hutchings, I. Brener, S. Horsley, W. L. Barnes, E. Hendry, *Nat. Commun.* **2021**, 12, 1017.
- [11] Y. Yang, J. Lu, A. Manjavacas, T. S. Luk, H. Liu, K. Kelley, J.-P. Maria, E. L. Runnerstrom, M. B. Sinclair, S. Ghimire, I. Brener, *Nat. Phys.* **2019**, 15, 1022.
- [12] X. Niu, X. Hu, S. Chu, Q. Gong, *Adv. Opt. Mater.* **2018**, 6, 21951071.
- [13] Y.-W. Huang, H. W. H. Lee, R. Sokhoyan, R. A. Pala, K. Thyagarajan, S. Han, D. P. Tsai, H. A. Atwater, *Nano Lett.* **2016**, 16, 5319.
- [14] V. Bruno, C. DeVault, S. Vezzoli, Z. Kudyshev, T. Huq, S. Mignuzzi, A. Jacassi, S. Saha, Y. D. Shah, S. A. Maier, D. R. S. Cumming, A. Boltasseva, M. Ferrera, M. Clerici, D. Faccio, R. Sapienza, V. M. Shalae, *Phys. Rev. Lett.* **2020**, 124, 043902.
- [15] K. Manukyan, M. Z. Alam, C. Liu, K. Pang, H. Song, Z. Zhao, M. Tur, R. W. Boyd, A. E. Willner, *Appl. Phys. Lett.* **2021**, 118, 241102.
- [16] C.-W. Lee, H. J. Choi, H. Jeong, *Nano Convergence* **2020**, 7, 3.
- [17] A. Forouzmand, M. M. Salary, G. K. Shirmanesh, R. Sokhoyan, H. A. Atwater, H. Mosallaei, *Nanophotonics* **2019**, 8, 415.
- [18] J. Park, J.-H. Kang, X. Liu, M. L. Brongersma, *Sci. Rep.* **2015**, 5, 15754.
- [19] J. R. Hendrickson, S. Vangala, C. Dass, R. Gibson, J. Goldsmith, K. Leedy, D. E. Walker, J. W. Cleary, W. Kim, J. Guo, *ACS Photonics* **2018**, 5, 776.
- [20] G. Kafaie Shirmanesh, R. Sokhoyan, R. A. Pala, H. A. Atwater, *Nano Lett.* **2018**, 18, 2957.
- [21] L. Tao, A. Anopchenko, S. Gurung, J. Zhang, H. W. H. Lee, *Sci. Rep.* **2019**, 9, 2789.
- [22] E. Feigenbaum, K. Diest, H. A. Atwater, *Nano Lett.* **2010**, 10, 2111. PMID: 20481480.
- [23] A. Calá Lesina, D. Goodwill, E. Bernier, L. Ramunno, P. Berini, *IEEE J. Sel. Top. Quantum Electron.* **2021**, 27, 4700116.
- [24] A. Howes, W. Wang, I. Kravchenko, J. Valentine, *Optica* **2018**, 5, 787.
- [25] G. T. Papadakis, H. A. Atwater, *Phys. Rev. B* **2015**, 92, 184101.
- [26] P. B. Johnson, R. W. Christy, *Phys. Rev. B* **1972**, 6, 4370.
- [27] O. Ozdemir, A. M. Aygar, O. Balci, C. Kocabas, H. Caglayan, E. Ozbay, *Carbon* **2016**, 108, 515.
- [28] C. Ciuti, G. Bastard, I. Carusotto, *Phys. Rev. B* **2005**, 72, 115303.

PUBLICATION

IV

**Suppressing the spectral shift of a polarization-independent nanostructure
with multiple resonances**

D. Ghindani, T. Pihlava and H. Caglayan

Opt. Lett. 47.21 (2022), 5553–5556

DOI: 10.1364/OL.472360

Publication reprinted with the permission of the copyright holders

Optics Letters

Suppressing the spectral shift of a polarization-independent nanostructure with multiple resonances

DIPA GHINDANI,  TUOMAS PIHLAVA,  AND HUMEYRA CAGLAYAN* 

Faculty of Engineering and Natural Sciences, Tampere University, Tampere 33720, Finland

*Corresponding author: humeyra.caglayan@tuni.fi

Received 5 August 2022; revised 27 September 2022; accepted 1 October 2022; posted 3 October 2022; published 20 October 2022

Resonances are the cornerstone of photonic applications in many areas of physics and engineering. The spectral position of a photonic resonance is dominated by the structure design. Here, we devise a polarization-independent plasmonic structure comprising nanoantennas with two resonances on an epsilon-near-zero (ENZ) substrate in order to loosen this correlation to obtain less sensitivity to geometrical perturbations of the structure. Compared with the bare glass substrate, the designed plasmonic nanoantennas on an ENZ substrate exhibit a nearly three-fold reduction only in the resonance wavelength shift near the ENZ wavelength as a function of antenna length.

Published by Optica Publishing Group under the terms of the [Creative Commons Attribution 4.0 License](#). Further distribution of this work must maintain attribution to the author(s) and the published article's title, journal citation, and DOI.

<https://doi.org/10.1364/OL.472360>

Introduction. Resonant optical devices play a significant role in the rapid development of nanotechnology and photonics-based technologies. Numerous applications such as filters [1,2], switches [3], modulators [4], and sensors [5] are realized by employing resonant devices. In addition to these applications, resonances are vital for studying several fundamental phenomena such as ultra-strong coupling [6] and nonlinear effects [7,8]. In principle, the resonance wavelength of a plasmonic antenna is significantly influenced by its shape, dimensions, and local environment, particularly its substrate [9–11], which can be a great advantage for sensing applications. However, the resonance modes are prone to geometrical inhomogeneity, this may arise as an issue for the fabrication or packaging of the integrated devices. Therefore, it is imperative to develop a novel way to endow the robustness of the plasmonic resonance from the geometrical perturbation for certain applications.

In recent years, the investigation of epsilon-near-zero (ENZ) materials in plasmonic systems has provided a great platform from the beam shaping to long-range qubit entanglement [12–19]. One particular concept is using the ENZ materials as a substrate as a means of reducing the index of the substrate, and because of the high dispersion of ENZ, the sensitivity of the plasmonic resonance on geometrical parameters can be reduced

significantly [20–25]. Slowing down the change in the plasmonic resonances near the ENZ wavelength, an effect referred to as resonance pinning, has been shown with an ENZ substrate such as Al-doped ZnO (AZO), indium tin oxide (ITO) and SiC [20,22,23], and using a hyperbolic ENZ metamaterial [21].

In this work, we investigate elongated nanoantenna arrays that support two resonances: one in the ENZ region while the other one is out of the ENZ region. The spectral shift of the plasmonic antenna exhibits the pinning effect only for the resonances close to the ENZ region. Therefore, this is especially a strong method when one wants to fix one of the resonances but not all of them when interacting with unpolarized light. We experimentally explored and characterized plasmonic antennas that are designed to exhibit polarization-independent dual resonances, one of them lies within the ENZ wavelength region and the other is spectrally far from the ENZ region. We further compared the resonance characterization of a plasmonic nanoantenna on a glass substrate (non-zero effective index). Our results show the utilization of ENZ materials for increasing the versatility and functionality of plasmonic structures. Additionally, our approach can be exploited to manipulate the resonance for advanced nanostructures and plasmonic applications, especially selectively controlling one of the resonances of the nanoantenna array designs for an unpolarized illumination.

Results and discussion. For probing the influence of ENZ properties upon local plasmon resonance, we utilized a commercially available 100 nm-thick ITO on glass as an ENZ substrate. An ITO is the widely used transparent conducting oxide (TCO) that exhibits a vanishing real part of the permittivity in the near-infrared spectral region with remarkably low optical losses. To characterize the dispersion of an ITO, we performed the spectroscopic ellipsometry measurement on 100 nm ITO thick film and extracted the complex permittivity. In Fig. 1(a), the real and imaginary parts of the 100 nm ITO thick film's permittivity are shown as the blue and red solid lines, respectively. The real part of the permittivity vanishes at 1320 nm and is marked as ENZ wavelength $\lambda_{ENZ} = 1320$ nm. The near-zero permittivity ($\epsilon_r \approx 0$) region that spans from 1120 to 1520 nm is highlighted by a gray shaded region in Fig. 1(a).

In order to achieve two resonances, it is possible to bring two structures with different dimensions into a single unit cell, or one can take advantage of an elongated structure such as an

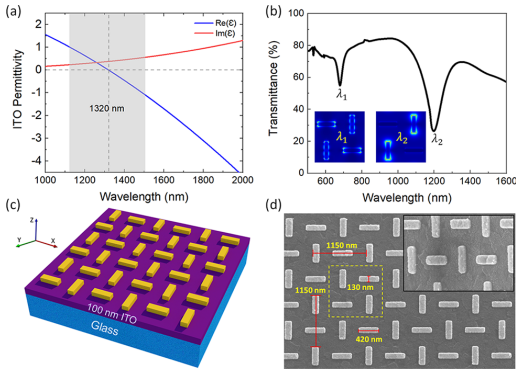


Fig. 1. (a) Experimentally recorded complex permittivity of 100 nm-thick ITO film. The blue and red solid lines depict the real and imaginary parts of the ITO's permittivity, respectively. (b) Simulated transmittance spectra of the plasmonic nanoantennas on the ITO substrate; the insets depict the electric field profile at the corresponding wavelength. (c) Schematic of polarization-independent Au nanoantenna array of thickness 40 nm on a 100 nm-thick ITO layer on a glass substrate. (d) Scanning electron microscope (SEM) image shows the top view of the Au nanoantenna array (scaling factor = 1, i.e., $l_s = 130$ nm and $l_l = 420$ nm); the dashed yellow box indicates the supercell with supercell periodicity 1150 nm in the x and y directions. The inset shows the SEM image taken at 30° tilt.

ellipse or rectangle. Here, we utilized a rectangular nanoantenna that can provide two plasmon resonances: TSPR (transversal surface plasmon resonance) and LSPR (longitudinal surface plasmon resonance). Furthermore, through the combination of the nanoantennas in two different orientations, we finalized the supercell design. We performed finite-difference time-domain (FDTD) numerical simulations to optimize nanoantenna dimensions and supercell periodicity. The experimentally recorded permittivity of the ITO is fed into the simulations, and was modeled by using Johnson and Christy material data from the in-build material library of Ansys Lumerical. The boundary conditions are set to periodic in the x and y directions and perfectly matched layers (PMLs) in the direction perpendicular to the source propagation (z). For any incident polarization, there exist two dipole resonances in the supercell, one corresponding to the long axis and another to the short axis of the elongated nanorods. This yields two spectrally distinct resonance dips in transmission spectra for any incident polarization (either x or y) as the design is rotationally symmetric, as shown in Fig. 1(b). We optimized the dimensions of the nanorods such that one resonance falls within the ENZ region of the ITO and the other resonance lies spectrally far from the ENZ region, shown in Fig. 1(b).

The transmission spectra corresponding to our devised polarization-independent plasmonic nanostructure shows the dips at shorter ($\lambda_1 = 650$ nm) and longer ($\lambda_2 = 1200$ nm) wavelengths in transmission spectra correspond to the dipole resonances along the short and long axes, respectively. The simulated electric field profiles corresponding to λ_1 and λ_2 are shown in inset of Fig. 1(b). From the electric field profile, it is evident that the dipole resonances for λ_1 and λ_2 are localized along the short and long axes, respectively.

Figure 1(c) shows the schematic of the ITO integrated polarization-independent plasmonic nanoantenna array. To emulate the polarization-independent response, the nanorods are alternatively arranged in two different orientations. To create these nanostructures with high precision, on glass and ITO substrates, we utilized electron beam lithography (EBL). In the glass substrate case, after spin coating PMMA 950K positive resist, the conducting polymer was spin-coated to avoid the charging effect. After exposure, both glass and ITO samples were developed in MIBK : IPA (1 : 3) solution. A 1 nm/40 nm layer of Ti/Au was deposited on developed samples using an electron beam metal evaporator followed by lift-off in S1165 remover. Figure 1(d) shows the SEM image of the top view of the fabricated plasmonic nanoantennas, where the supercell is marked by a yellow dashed square. The periodicity of the supercell along the x and y directions is $P = 1150$ nm, while the length of nanorod along short (l_s) and long (l_l) axes are $l_s = 130$ nm and $l_l = 420$ nm and the thickness of the nanorod is 40 nm. We employed gold (Au) as the plasmonic material owing to low loss and ease of deposition.

By varying the length of the nanorods in the supercell, i.e., scaling with a common factor that varied between 0.8 and 1.2 and keeping the periodicity constant, the plasmonic resonance response can be tuned systematically. The optimized spatial dimensions of the plasmonic nanorod that corresponds to scaling factor “1” are $l_s = 130$ nm and $l_l = 420$ nm. Further, we fabricated a set of samples on both the ITO substrate and bare glass substrate with varying scaling factors from 0.8 to 1.2, the SEM images are shown in Fig. 2(a). For varying the scaling factors, the

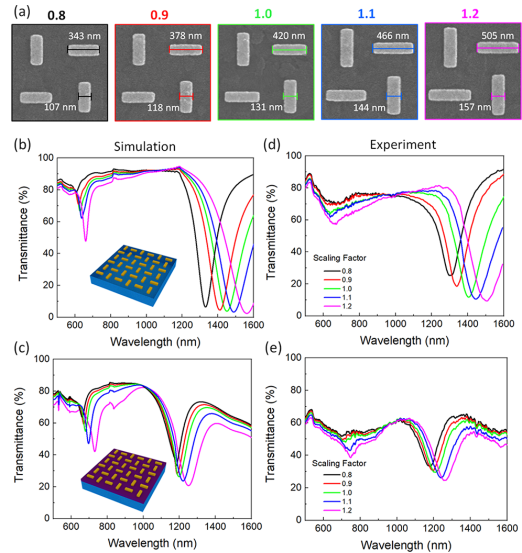


Fig. 2. (a) SEM images of the fabricated set of samples with varying scaling factors from 0.8 to 1.2 and a constant periodicity of 1150 nm in both x and y . (b),(c) Simulated transmittance spectra of the supercell array of nanorods on a glass and ITO substrate for various scaling factors (0.8 to 1.2); the inset shows a schematic of the Au antenna array on glass and ITO, respectively. (d),(e) Experimentally recorded transmission spectra of the supercell array of nanorods on a glass and ITO substrate for various scaling factors of 0.8 to 1.2.

lengths of short and long axes change simultaneously; however, the periodicity of the supercell is fixed at $P = 1150$ nm. Figures 2(b) and 2(c) show the simulated transmission spectra for the plasmonic nanoantenna array upon incidence of unpolarized light for bare glass and ITO substrate, respectively, at different scaling factors. The simulated results clearly illustrate that the resonance wavelength that lies within the ENZ region of the ITO substrate (λ_2) exhibits much less sensitivity to dimension change as compared with the bare glass substrate.

To further verify this, we experimentally recorded the transmission spectra for all the fabricated plasmonic nanorod array using a multifunctional WITec alpha300C confocal Raman microscope. For both nanoantennas fabricated on ITO film and on a glass substrate, the transmission was normalized to the transmission spectrum of glass. The results corresponding to nanostructures on the bare glass and ITO substrate are shown in Figs. 2(d) and 2(e), respectively. The experimental results show good agreement with the simulation results for both cases. The small difference in simulated and experimental transmission spectra at the shorter wavelength around 650 nm, e.g., resonance broadening, can be attributed to the fabrication imperfections such as slight inhomogeneity, rounding the edge of the nanoantenna, and experimental noise in the visible range due to the detector. Importantly, the experimental results confirm the effect of the ENZ on the resonance. The change in plasmonic resonance that lies within the ENZ region of ITO, i.e., λ_2 exhibits nearly 80 nm spectral shift when changing the scaling factor from 0.8 to 1.2, while the plasmonic nanorod on bare glass substrate shows 225 nm shift in resonance wavelength [see Figs. 2(d) and 2(e)]. It is important to note that the shift of resonance dip at a lower wavelength (λ_1) is similar for both ITO and bare glass substrate.

To illustrate the shift in resonance wavelength more clearly, we plotted the change in resonance wavelength ($\Delta\lambda$) as a function of the scaling factor. Figure 3 compares the shift in resonance wavelengths numerically as well as experimentally. Figures 3(a) and 3(b) depict the $\Delta\lambda$ for lower resonance (λ_1), where the black and red lines represent the resonance wavelength of the plasmonic nanorod on bare glass and ITO substrate, respectively. As is clear from Figs. 3(a) and 3(b), the shift in lower wavelength resonance is nearly identical for both cases. However, the shift in longer wavelength resonance, which lies within the ENZ region of ITO, exhibits less susceptibility toward geometrical changes when it is fabricated on an ENZ substrate. Figures 3(c) and 3(d) reveal that the spectral shift in longer wavelength resonance on the ITO substrate is three times less compared with the resonance shift on a bare glass substrate. This slowdown in the change in resonance wavelength is attributed to the resonance pinning around the ENZ wavelength.

To understand the underlying physics behind the resonance pinning effect, we express the rate of change of resonance wavelength as a function of antenna length [23] as

$$\frac{\delta\lambda}{\delta l} = A \frac{n^2}{n - \lambda_0 \frac{\partial n}{\partial \lambda}}, \quad (1)$$

where n is the effective index, A is constant, and λ_0 is the free space wavelength. For the non-dispersive medium, i.e., $\delta n / \delta \lambda = 0$, the resonance wavelength becomes proportional to the length of the nanoantenna and the index ($\lambda \propto Anl$).

We numerically calculated the effective mode index of the nanorod on the ITO substrate and glass substrate using a finite-difference eigenmode (FDE) mode solver in Ansys. The

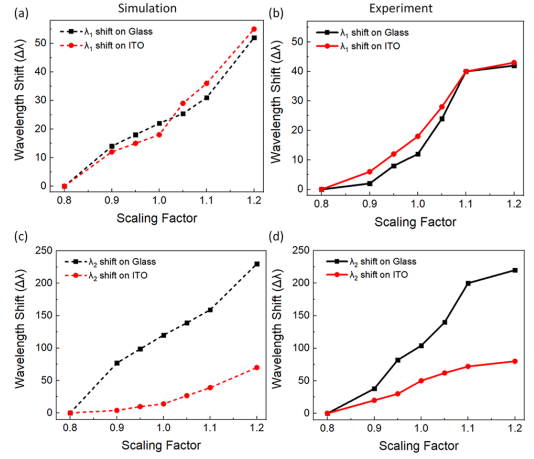


Fig. 3. (a),(b) Simulated and experimental wavelength shift result ($\Delta\lambda$) as a function of scaling factor, respectively, at resonance 1 (λ_1) at a shorter wavelength. (c),(d) Simulated and experimentally recorded wavelength shifts, respectively, corresponding to resonance 2 (λ_2) at a longer wavelength.

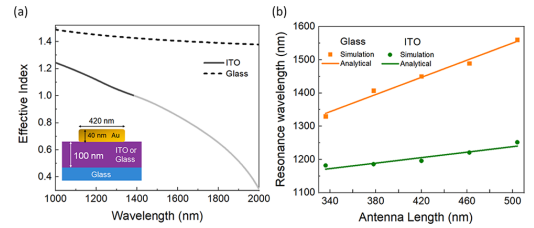


Fig. 4. (a) Numerically calculated effective mode index for a gold nanorod on the ITO (black solid line and values below unity are colored in gray) and a glass substrate (black dashed line). The inset shows the configuration of the finite-element solver. (b) Resonant wavelength (λ) as a function of antenna length (l) for the glass (orange) and ITO (green) substrates. The solid lines are calculated analytically, and square and circular markers are the results of FDTD numerical calculations.

calculated results are shown in Fig. 4(a), which reveal that the effective index of the nanorod on the ENZ substrate has strong negative dispersion and is less than unity for the wavelength past the ENZ wavelength of ≈ 1320 nm. We noticed that the effective index value is below unity at higher wavelengths, which is not physical and arises due to the approximations of the boundary conditions in the numerical calculation, therefore, we colored that part gray. On the contrary, the effective index of the nanorod on a glass substrate is nearly constant (i.e., weakly dispersive) with a value close to ≈ 1.46 . The pinning effect is due to a reduction in the effective mode index and highly negative dispersive nature of the ENZ substrate, which limits the spectral shift of the nanorod antenna beyond the ENZ region.

Furthermore, Fig. 4(b) shows a comparative plot of the resonance wavelength for bare glass and ITO substrate. The resonance wavelength (λ) is plotted against antenna length (l) analytically according to the relation in Ref. [23], which is based

on the Fabry–Perot model. The square and circular markers depict the resonance wavelength extracted using FDTD numerical calculations. The simulation results show good agreement with these analytical results.

Conclusion and outlook. We devised a plasmonic nanoantenna exhibiting a polarization-independent spectral response. By incorporating the plasmonic structure with an ITO substrate, we showed the spectral pinning of plasmonic resonance within the ENZ region. To showcase this experimentally, we judiciously designed a plasmonic nanoantenna array that yields dual resonances: one lies within the ENZ region, and the other exists spectrally far from the ENZ region. Our results reveal that the shift in resonance wavelength for the plasmonic nanorod array fabricated on ITO substrate exhibits less susceptibility toward geometrical changes. We benchmarked the performance of the plasmonic nanoantennas devised on ITO substrate with the nanoantennas on a bare glass substrate. We showed the spectral shift of the polarization-independent nanoantennas suppressing by approximately three times in the case of the ITO substrate due to the near-zero index of the substrate. We verified numerically, analytically, and experimentally that the shift in resonance wavelength becomes nearly independent of the antenna length near the ENZ wavelength. This control over plasmon resonance and the reduced dependence on antenna dimensions relax the requirement of precise subwavelength features. Furthermore, less sensitivity of the nanoantenna's resonance toward its length results in a narrow spectral bandwidth, which is important for sensing, color filtering, and switching applications. However, some applications, such as data communication which requires large bandwidth, may not benefit.

Additionally, we demonstrate the universality of the pinning effect by showing the slowing down of resonance near the ENZ point in a multi-resonance plasmonic system. Also, selectively controlling one of the resonances of the nanoantenna designs for unpolarized illumination is of great importance for advanced plasmonic applications. Our approach can compensate for fabrication errors, reduce the need for advanced fabrication, and increase flexibility in plasmonic nanoantenna designing. The demonstrated results pave the path for utilizing ENZ materials to increase the versatility and functionality of plasmonic structures and provide foundational insight into this exotic material phenomenon. Moreover, we foresee the plasmon resonance wavelength being adjusted by dynamically tuning the permittivity of the substrate around the ENZ point via optical or electrical control in both reflection and transmission modes, allowing more functional implementations of this platform.

Funding. Academy of Finland (320165); H2020 European Research Council (802986).

Acknowledgments. The authors thank Anil Atalay Appak for effective index calculation and Mohsin Habib for the initial scientific discussions. H.C. acknowledges the financial support of the European Research Council

(Starting Grant project aQUARIUM; agreement no. 802986).

Disclosures. The authors declare no conflicts of interest.

Data availability. Data underlying the results presented in this paper are not publicly available at this time but may be obtained from the authors upon reasonable request.

REFERENCES

1. T. Xu, Y.-K. Wu, X. Luo, and L. J. Guo, *Nat. Commun.* **1**, 59 (2010).
2. D. Ghindani, I. Issah, S. Chervinskii, M. Lahikainen, K. Kuntze, A. Priimagi, and H. Caglayan, *ACS Photonics* **9**, 2287 (2022).
3. S. Sederberg, D. Driedger, M. Nielsen, and A. Elezzabi, *Opt. Express* **19**, 23494 (2011).
4. Q. Xu, B. Schmidt, S. Pradhan, and M. Lipson, *Nature* **435**, 325 (2005).
5. X. Ma, S. Fan, H. Wei, Z. Zuo, S. Krishnaswamy, and J. Fang, *Opt. Express* **27**, 33051 (2019).
6. P. Forn-Díaz, L. Lamata, E. Rico, J. Kono, and E. Solano, *Rev. Mod. Phys.* **91**, 025005 (2019).
7. G. Li, S. Zhang, and T. Zentgraf, *Nat. Rev. Mater.* **2**, 17010 (2017).
8. Y. Yang, W. Wang, A. Boulesbaa, I. I. Kravchenko, D. P. Briggs, A. Poretzky, D. Geoghegan, and J. Valentine, *Nano Lett.* **15**, 7388 (2015).
9. B. Gerislioglu, L. Dong, A. Ahmadivand, H. Hu, P. Nordlander, and N. J. Halas, *Nano Lett.* **20**, 2087 (2020).
10. B. C. Yildiz, M. Habib, A. R. Rashed, and H. Caglayan, *J. Appl. Phys.* **126**, 113104 (2019).
11. F. J. González and J. Alda, *Opt. Commun.* **284**, 1429 (2011).
12. I. Issah, M. Habib, and H. Caglayan, *Nanophotonics* **10**, 4579 (2021).
13. L. Caspani, R. P. M. Kaipurath, M. Clerici, M. Ferrera, T. Roger, J. Kim, N. Kinsey, M. Pietrzyk, A. Di Falco, V. M. Shalae, A. Boltasseva, and D. Faccio, *Phys. Rev. Lett.* **116**, 233901 (2016).
14. D. Ghindani, A. R. Rashed, M. Habib, and H. Caglayan, *Adv. Opt. Mater.* **9**, 2100800 (2021).
15. V. Bruno, C. DeVault, S. Vezzoli, Z. Kudyshev, T. Huq, S. Mignuzzi, A. Jacassi, S. Saha, Y. D. Shah, S. A. Maier, D. R. S. Cumming, A. Boltasseva, M. Ferrera, M. Clerici, D. Faccio, R. Sapienza, and V. M. Shalae, *Phys. Rev. Lett.* **124**, 043902 (2020).
16. M. Z. Alam, I. D. Leon, and R. W. Boyd, *Science* **352**, 795 (2016).
17. I. Liberal and N. Engheta, *Nat. Photonics* **11**, 149 (2017).
18. X. Niu, X. Hu, S. Chu, and Q. Gong, *Adv. Opt. Mater.* **6**, 1701292 (2018).
19. S. Campione, J. R. Wendt, G. A. Keeler, and T. S. Luk, *ACS Photonics* **3**, 293 (2016).
20. J. Kim, A. Dutta, G. V. Naik, A. J. Giles, F. J. Bezares, C. T. Ellis, J. G. Tischler, A. M. Mahmoud, H. Caglayan, O. J. Glembocki, A. V. Kildishev, J. D. Caldwell, A. Boltasseva, and N. Engheta, *Optica* **3**, 339 (2016).
21. M. Habib, D. Briukhanova, N. Das, B. C. Yildiz, and H. Caglayan, *Nanophotonics* **9**, 3637 (2020).
22. X. Duan, F. Zhang, Z. Qian, H. Hao, L. Shan, Q. Gong, and Y. Gu, *Opt. Express* **27**, 7426 (2019).
23. C. T. DeVault, V. A. Zenin, A. Pors, K. Chaudhuri, J. Kim, A. Boltasseva, V. M. Shalae, and S. I. Bozhevolnyi, *Optica* **5**, 1557 (2018).
24. O. Dominguez, L. Nordin, J. Lu, K. Feng, D. Wasserman, and A. J. Hoffman, *Adv. Opt. Mater.* **7**, 1800826 (2019).
25. S. A. Schulz, A. A. Tahir, M. Z. Alam, J. Upham, I. De Leon, and R. W. Boyd, *Phys. Rev. A* **93**, 063846 (2016).

